A STUDY OF EDDY - CURRENT COUPLINGS WITH AND WITHOUT ENDRINGS

A Thesis submitted for the degree of

MASTER OF SCIENCE

BALAPRABUDAS JAMES

THE UNIVERSITY OF ASTON IN BIRMINGHAM

October, 1969.

Summary

This thesis presents the results of

(a) an experimental verification of Davies' generalised analysis of eddy-current coupling performance,

and (b) a comparison of the performance of a coupling fitted with a solid iron drum and an iron drum fitted with copper endrings as a practical attempt to approximate the idealised condition of endrings of negligible resistance.

For (a), the coupling was comprehensively tested with the copper endring drum. Full details of the tests, together with their analysis and comparison with Davies' generalised analysis, are given.

An attempt is made to assess the effects of the end-regions of the solid iron drum on the coupling's performance. This assessment is based on a comparison of test results for the endring drum with those for a solid iron drum. Gibbs' analysis of the end-region is compared with test results and a simpler alternative analysis of the end-region is also presented.

Contents

List of symbols

B	=	flux density, Wb/m^2
B_g	=	peak airgap flux density on load, Wb/m^2
C	=	constant, defined in Section 3.9.5 and Section 4.5
D	=	diameter of drum at airgap, m
d	=	depth of penetration, m
E	=	electric field intensity, V/m
F_R	=	peak armature reaction ampere-turns per pole, AT/pole
F_g	=	total airgap ampere-turns per pole, AT/pole
F_ϕ	=	flux component of F_g
f	=	slip frequency, Hz
g	=	radial airgap length, m
H	=	magnetising force, AT/m
H_m	=	peak value of H at drum airgap surface, AT/m
h	=	harmonic order, used as a subscript
I	=	total current per unit circumferential length, A/m
I_T	=	total current in the end region, A
J	=	current density, A/m^2
J_z	=	current density along z-axis, A/m^2
J_m	=	peak current density at drum airgap surface, A/m^2
j	=	$\sqrt{-1}$
K, K'	=	elliptic integrals (Section 4.9)
K	=	constant (equation (1.14, page 16)
k, k_1	=	moduli of elliptic integrals (Figure 4.10 and 4.11)

L	=	drum iron active length, m
L_c	=	length of copper endring per pole pitch, m
m	=	constant, (Equation 1.14, page 16)
N	=	drive motor input speed, r.p.s.
n	=	slip-speed, r.p.m.
P	=	total drum loss, W
p	=	pole pairs
p	=	constant, Section 4.5
R_a	=	effective resistance of the active region per unit depth of drum, Ω
R_e	=	effective resistance of the end region per unit depth of drum, Ω
R_i	=	resistance of the active region for depth of drum, d, the depth of penetration, Ω
s	=	slip, per unit
T	=	torque, Nm
T_h	=	h^{th} harmonic torque
T_m	=	peak torque, Nm
W	=	drum loss per unit area of drum surface, W/m^2
W_1	=	fundamental drum loss per unit area of drum surface, W/m^2
W_h	=	h^{th} harmonic drum loss per unit of drum surface, $W./m^2$
W_m	=	total drum loss at peak torque, W
W_p	=	end region loss per pole pitch, W
x	=	peripheral direction in drum
y	=	radial direction in drum
z	=	axial direction in drum
α	=	$\sqrt{\frac{\mu\mu_o\ \omega\sigma}{2}} = \frac{1}{\text{depth of penetration}}$ (m^{-1})
β	=	auxiliary quantity (defined in Section 3.9.5)

γ = auxiliary quantity (defined in Section 4.4.1, page 100)

δ = auxiliary quantity (defined in Section 3.9.5, page 75)

ε = angle (shown in Figure 4.2, page 81), deg.

θ = angle (shown in Figure 4.2, page 81), deg.

λ = wave length of drum variation, m (pitch of pole pair)

λ = approximately equal to 1/d, (Section 1.4)

μ_o = permeability of free space, H/m

μ_r = relative permeability (numeric)

σ = conductivity, S/m

ρ = resistivity, Ωm

ρ_c = resistivity of copper, Ωm

ρ_i = resisitivity of drum iron, Ωm

ϕ = potential function, Section 4.5

ϕ_m = maximum of potential function, Section 4.5

ϕ = angle (shown in Figure 4.2, page 81), deg.

ϕ_{ac} = fundamental flux per pole, Wb

χ = complex variable

ω = angular velocity, rad/s

The symbol $\bar{}$ (for example, $\bar{J}$) represents a vector quantity.

Note: In general, M.K.S. units have been used but some drawings which are reproductions contain inch units.

CHAPTER 1 The eddy-current coupling

1.1 Principles of operation

In its elementary form, the eddy-current coupling consists of a circular ferromagnetic drum, inside which a field member is mounted concentrically. The drum and field member are supported on individual shafts, and are separated from each other by a small radial airgap. The arrangement is shown diagrammatically in Figure 1.1.

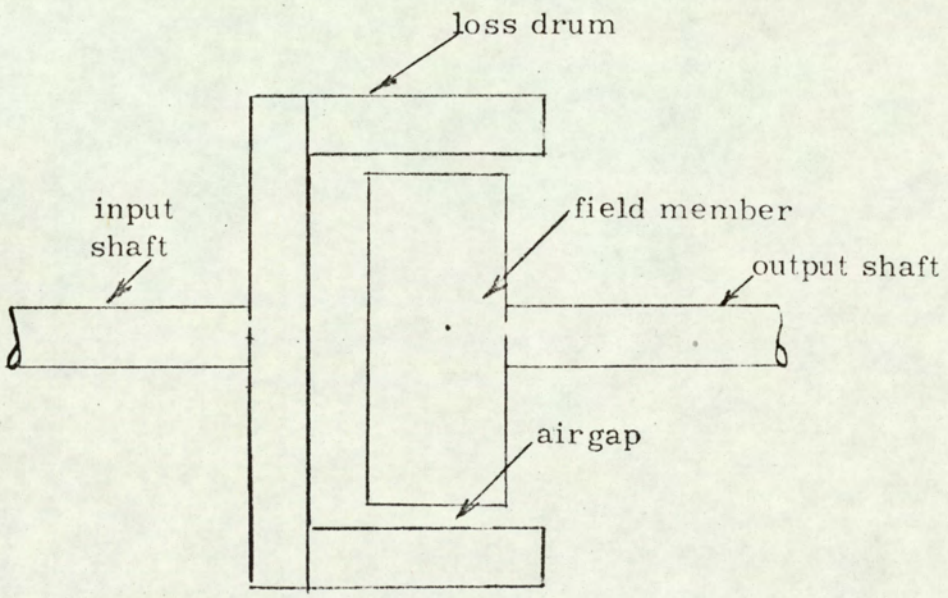

Figure 1.1

The field member is normally an electromagnet. It is common practice to couple the drum to a motor and the field member to a load. When the drum rotates relative to an excited field member, eddy currents are generated in the drum. The losses associated with the eddy currents must be supplied by the input, so the basic power balance of the device is

$$2\pi NT = 2\pi NT(1 - s) + \text{(drum eddy-current loss)}$$

where

N = input speed in r.p.s.,

T = torque in Nm,

and $s = \dfrac{\text{input speed - output speed}}{\text{input speed}}$

Therefore the eddy-current loss in the drum, the slip power, is $2\pi NTs$.

For a given coupling, the drum loss is determined by the drum frequency* and the magnitude of the field current. The direction of rotation of the coupling cannot be reversed by reversing the field current, since the torque is independent of the excitation polarity. The coupling is essentially a torque transmitter.

---

* Drum frequency or slip frequency = pNs, where
p = pole pairs

1.2 Basic design considerations and construction

The drum has two functions; (a) to provide a path for the main magnetic flux, and (b) to generate the slip power. The choice of the drum material must therefore be made on a compromise between the requirements of the magnetic and electric circuits: magnetic efficiency demands high permeability, electrical efficiency low resistivity. There is still speculation about the significance of hysteretic effects in solid iron devices and hence they will not be considered.

The field member may be one of the following types:

a) inductor;
b) Lundell or interdigitated;
c) salient-pole;
d) permanent-magnet.

Figures 1.2(a) & (b) show the essential features of an inductor-type coupling. When the field coil is excited, the field member produces a modulated homopolar flux density distribution in the airgap as shown in Figure 1.2(c) & (d).

Figure 1.3(a) shows the basic features of a Lundell or interdigitated coupling. When the field coil is excited, the field member produces alternate north and south poles as shown in Figure 1.3(b). When the poles are in circumferential alignment, Figure 1.3(c), the field member is fully interdigitated; when they are not it is partially interdigitated, Figure 1.3(b). The fully interdigitated field member produces a heteropolar flux density distribution in the airgap; the partially interdigitated

INDUCTOR COUPLING

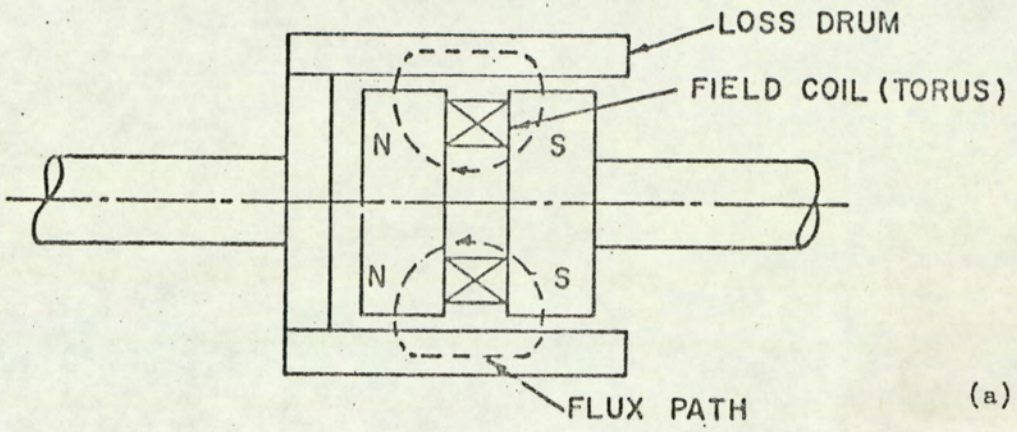

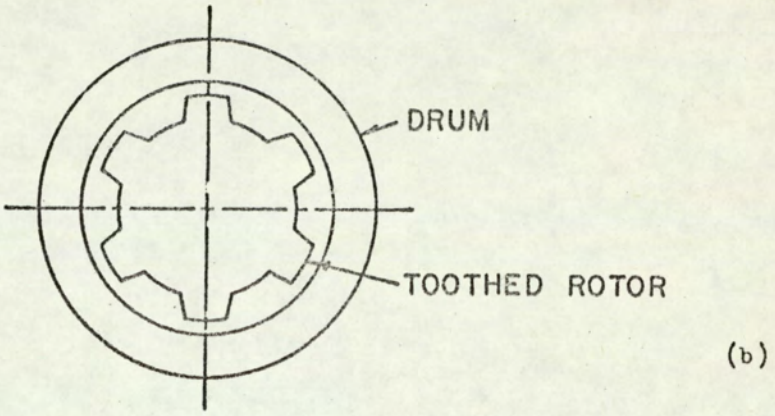

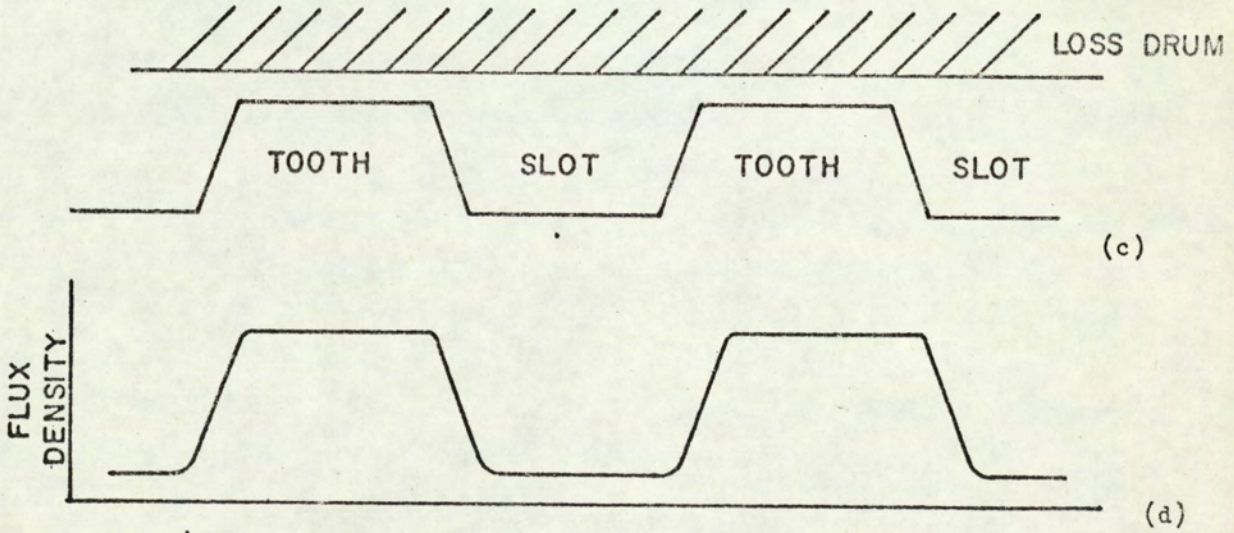

a) Schematic layout showing homopolar nature of machine
b) Cross-section of rotor and drum showing slotting
c) and d) Expanded view of airgap. The slotting pattern in c) produces the flux density pattern in d).

FIGURE 1.2

LUNDELL COUPLING

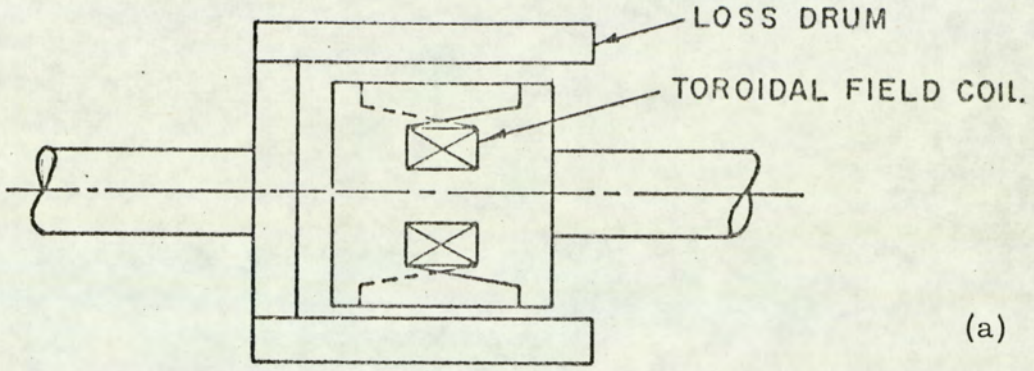

(a)

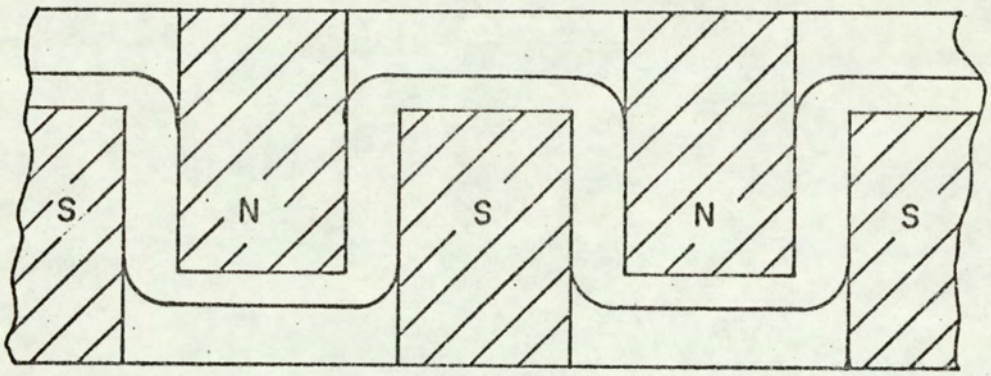

(b)

(Pole faces are shaded for clarity)

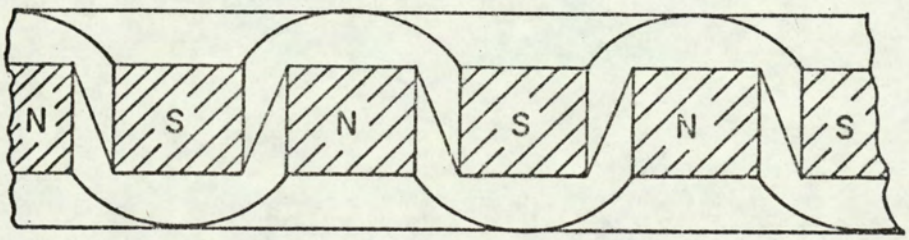

(c)

a) Schematic layout
b) Expanded view of airgap region, showing alternate N-S poles
c) Fully interdigitated form of Lundell coupling

FIGURE 1.3

one produces a combination of hetero- and homopolar distributions. Lundell-type field members are used in couplings rated up to 100 hp.

Salient pole construction is rare but, if a coupling were to be used in a fast response control system, then laminated salient poles could be used.

Permanent-magnet field systems are used for some specialised applications, for example, fan drives in cars where space is limited, and in applications where constructional simplicity is essential.

Sliprings can be used to supply the field current to a rotating field member but, as these are considered to be a source of trouble, the majority of commercial couplings are made with stationary field coils. A typical commercial arrangement is shown schematically in Figure 1.4. It will be seen that there are now two airgaps in the magnetic circuit which increases the excitation required.

A brief discussion of field leakage in Lundell type field members is given in Appendix A3.

Cut-away cross-sectional photograph of a commercial air-cooled Lundell-type eddy-current coupling with driving motor is shown in Plate 1.

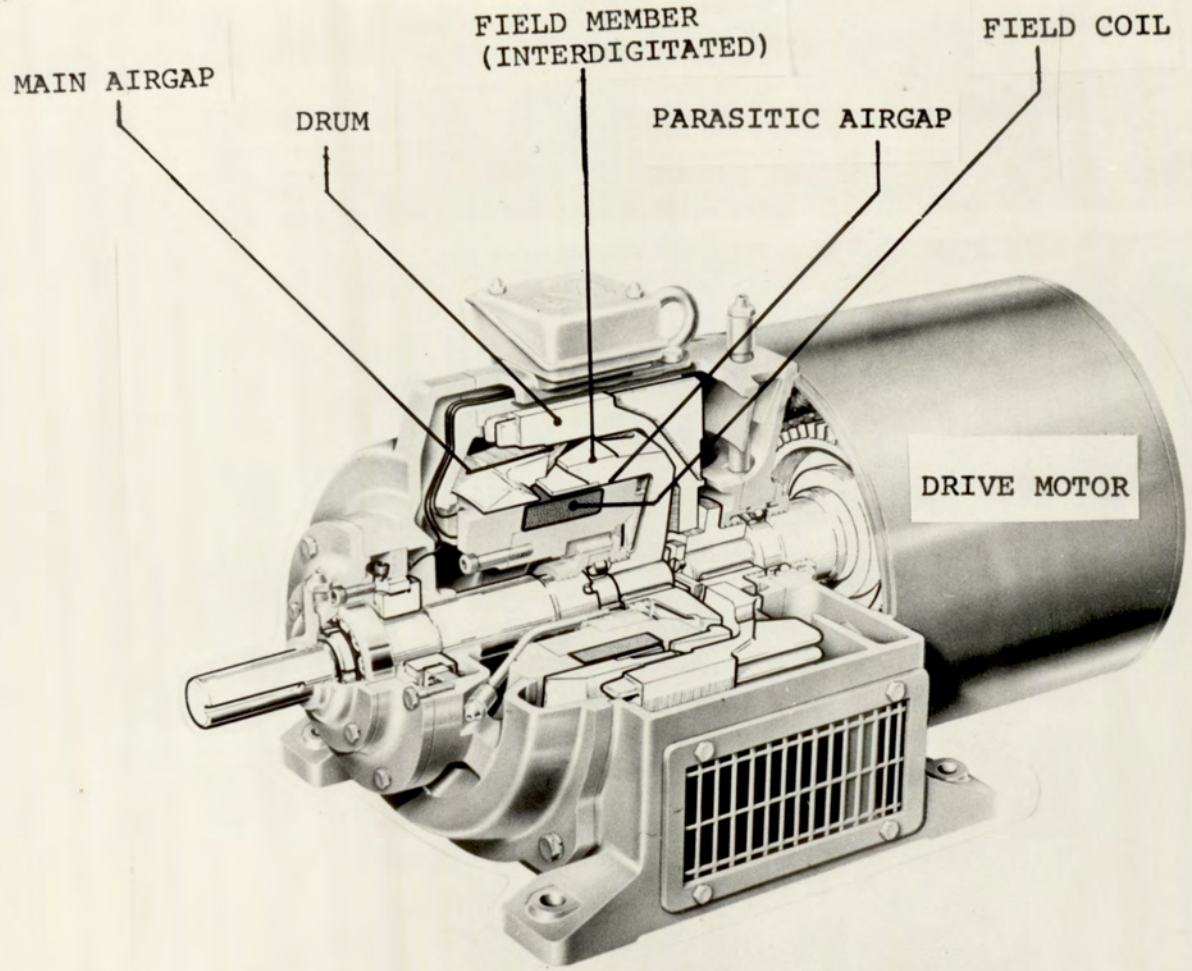

Cut-away Cross Section of a Commercial Air-Cooled Eddy Current Coupling with Driving Motor

Plate 1 (Photo - Mawdsley's Ltd.)

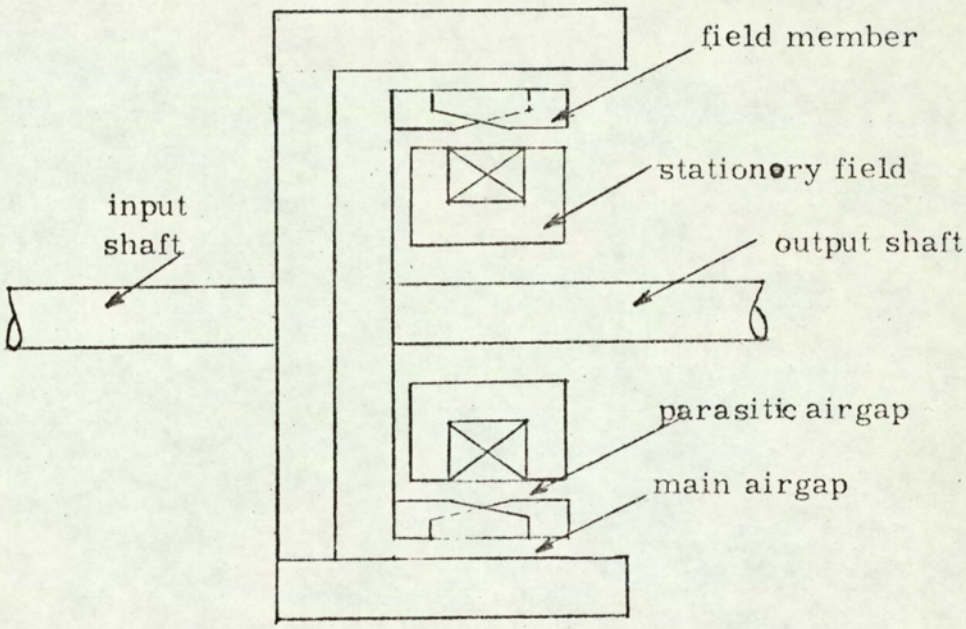
field member
stationary field
input
shaft
output shaft
parasitic airgap
main airgap

Figure 1.4

1.3 Performance and applications

A typical family of torque-speed curves for a coupling is shown in Figure 1.5.

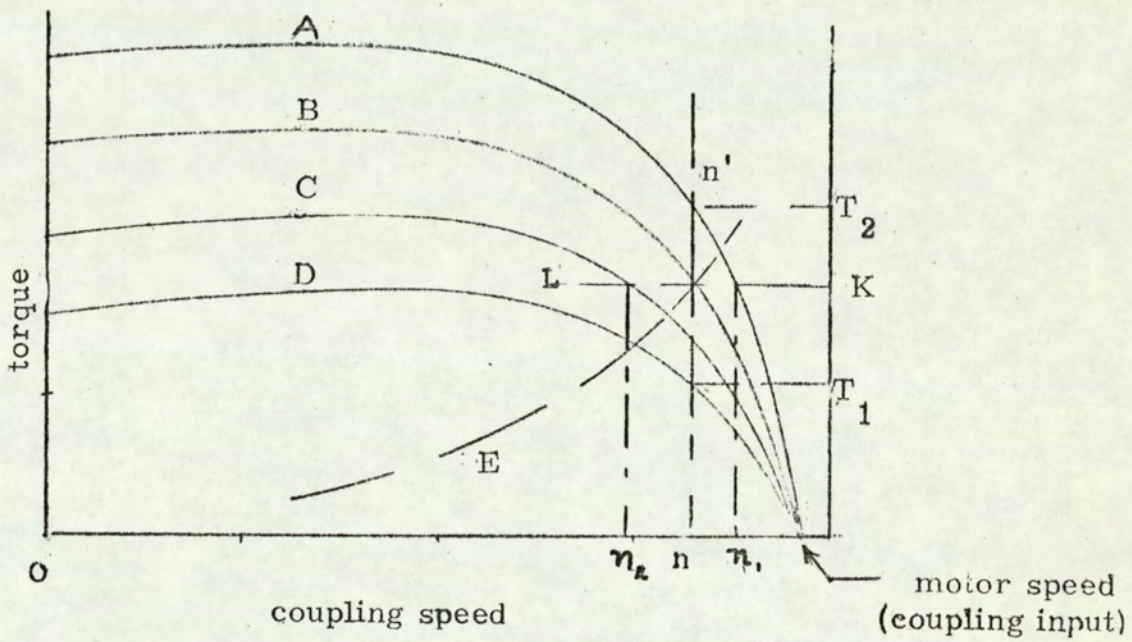

Figure 1·5

A, B, C, D are the coupling torque-speed curves at various field currents. The inherent characteristics of the torque-speed curves of the coupling are non-linear and are load-dependent. For a given load torque, the output speed can be regulated by varying the field current. Conversely, for a given field current, the output speed will depend on the load torque. On the one hand, if a constant-torque characteristic, such as that represented by the line KL, is required over the speed range n_1 to n_2, then the excitation must be varied between the limits represented by curves A and C to give the required

constant torque characteristic. On the other hand, if constant speed is required over the torque range T_1 to T_2, then the excitation must be varied between the limits of curves D and A

If, however, the coupling is to be used for a drive having a load characteristic as represented by the curve E, which is typical of a fan drive, then the excitation must be varied between the limits of curves A and D. The control is inherently smooth, and therefore the coupling is suitable for coilers, conveyors, machine-tools, extruders, fans, and pumps.

1.4 Survey of literature

In the analysis of the performance of the coupling, the field member is relatively unimportant since its sole function is to produce electromagnetic excitation of the drum material. Most of the published analytical work concentrates on determining the electromagnetic conditions in the drum. However, as with all electromagnetic problems in rotating electrical machines, the complex and finite geometry of the coupling, together with the non-linear and hysteretic magnetic behaviour of iron, render the problem intractable by conventional analytical methods. Simplifying assumptions must therefore be made.

The common starting point for the more important analytical work on the coupling (except Ref. 9) is to consider the drum as a plane-faced, semi-infinite conductive slab with

sinusoidal excitation along its plane face. Figure 1.6 shows the idealised problem.

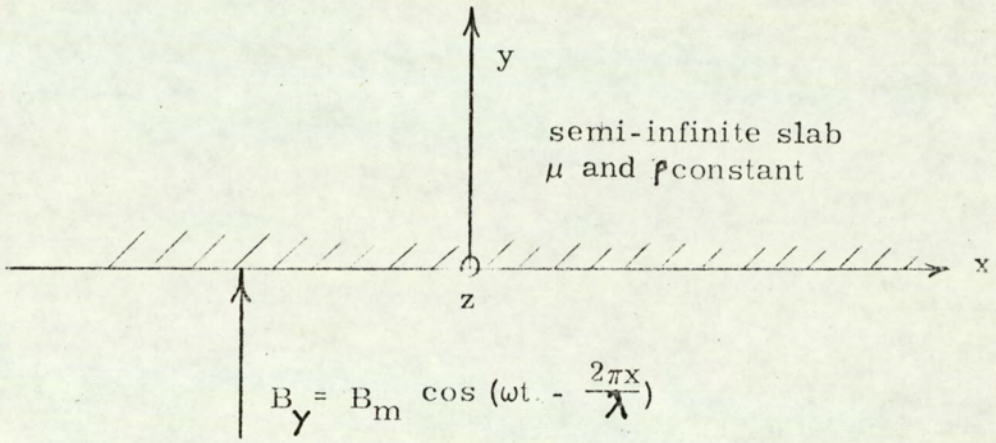

Figure 1.6

In the slab, the electric intensity $\overline{E}$, the eddy-current density $\overline{J}$, and the flux density $\overline{B}$ are related by

$$\nabla \times \overline{E} = - \partial \overline{B} / \partial t, \qquad (1.1)$$

and

$$\overline{J} = \sigma \overline{E}, \qquad (1.2)$$

where σ is the conductivity of the drum material.
The magnetic field intensity $\overline{H}$ is related to $\overline{J}$ by

$$\nabla \times \overline{H} = \overline{J}, \qquad (1.3)$$

since the displacement current density, $\overline{D}$, in the iron is negligible. Assuming that the iron is homogeneous and isotropic, and that

$$\overline{B} = \mu \overline{H}, \qquad (1.4)$$

we have from (1.1) to (1.3)

$$\nabla^2 \bar{J} = -\mu\sigma \, \partial \bar{J} / \partial t \, . \qquad (1.5)$$

$\bar{H}$, $\bar{B}$, and $\bar{E}$ can also be treated to give governing equations similar to (1.5). Since the drum is infinitely long in the z-direction, the problem can be treated as quasi-two-dimensional, and (1.5) becomes

$$\frac{\partial^2 J_z}{\partial x^2} + \frac{\partial^2 J_z}{\partial y^2} = -\mu\sigma \frac{\partial J_z}{\partial t} \, . \qquad (1.6)$$

Since the problem is linear and the magnetic excitation is sinusoidal, the solution of equation (1.6) can be written

$$J_z = J_m e^{-\alpha y} \cos\left(\omega t - \frac{2\pi x}{\lambda} - \alpha y\right), \qquad (1.7)$$

provided that $\sqrt{2}\alpha \gg {}^{2\pi}/\lambda$,

where

J_m = peak value of current density at $y = 0$,

$\alpha = \sqrt{\mu\omega\sigma/2}$,

$\mu = \mu_r \mu_0$,

$\omega = 2\pi f$,

f = slip frequency,

and λ = wave length of the exciting wave (2 pole pitches)

Equation (1.7) shows that the eddy-currents induced in the drum are attenuated and phase-retarded as they penetrate the drum. The total current per unit circumferential length is

$$I = \int_0^\infty J_z \, dy$$

$$= \frac{J_m}{\sqrt{2}} \frac{1}{\alpha} \cos\left(\omega t - \frac{2\pi x}{\lambda} - \frac{\pi}{4}\right) \qquad (1.8)$$

This is equivalent to a uniform current density of $J_m/\sqrt{2}$ in a layer of thickness $y = 1/d = 1/\alpha$, phase retarded by 45^o with respect to the actual current density at the surface (y=0). The thickness d is the depth of penetration. Figure 1.7 shows the variation of the amplitude of the current density with drum depth.

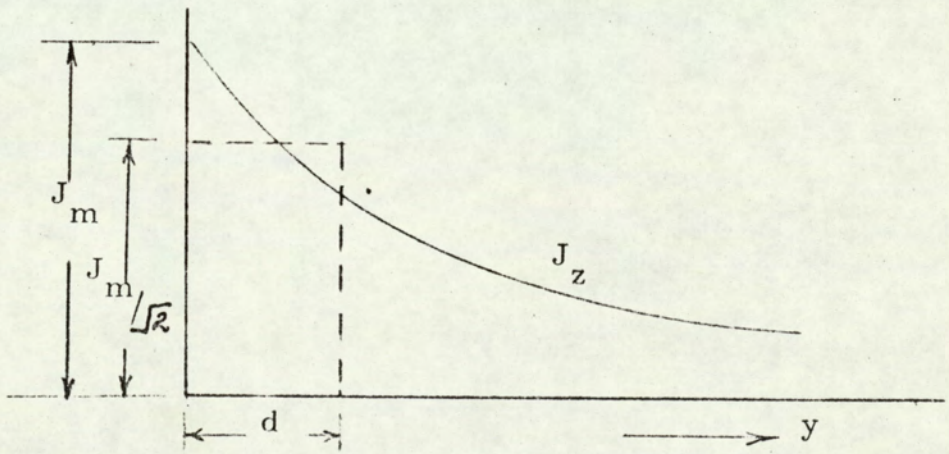

Figure 1.7

The time-average of the drum loss per unit area of surface

$$W = \frac{\omega}{2\pi} \cdot \frac{2}{\lambda} \int_0^{2\pi/\omega} \int_0^{\infty} \int_0^{\lambda/2} J_z^{\,2}\, dx\, dy\, dt$$

$$= \frac{J_m^{\,2}}{4\sigma\alpha} \qquad (1.9)$$

The total drum loss is

$$P = \pi DL\, W, \qquad (1.10)$$

where D is the diameter of the drum airgap surface, and L is the polar axial length (active length).

The torque is given by

$$T = P/\omega \qquad (1.11)$$

The eddy-current armature reaction is [8]

$$\int_0^{\infty} \int_0^{x} J_z\, dx\, dy = \frac{J_m \lambda}{2\sqrt{2}\alpha\pi} \cos(\omega t - 2\pi x/\lambda + \pi/4)$$

The armature reaction has a peak value

$$F_R = \frac{J_m \lambda}{2\sqrt{2}\alpha\pi} \qquad (1.12)$$

and

is $\pi/4$ out of phase with Jm at y = 0.

The discussion so far has dealt with the analysis of an idealised model of the coupling. The efforts of individual authors to extend this analysis to actual couplings will now be considered. Gibbs[3]' work is an excellent example of a judicious blend between theoretical and practical design. His conceptual model of the problem is shown in Figure 1.8.

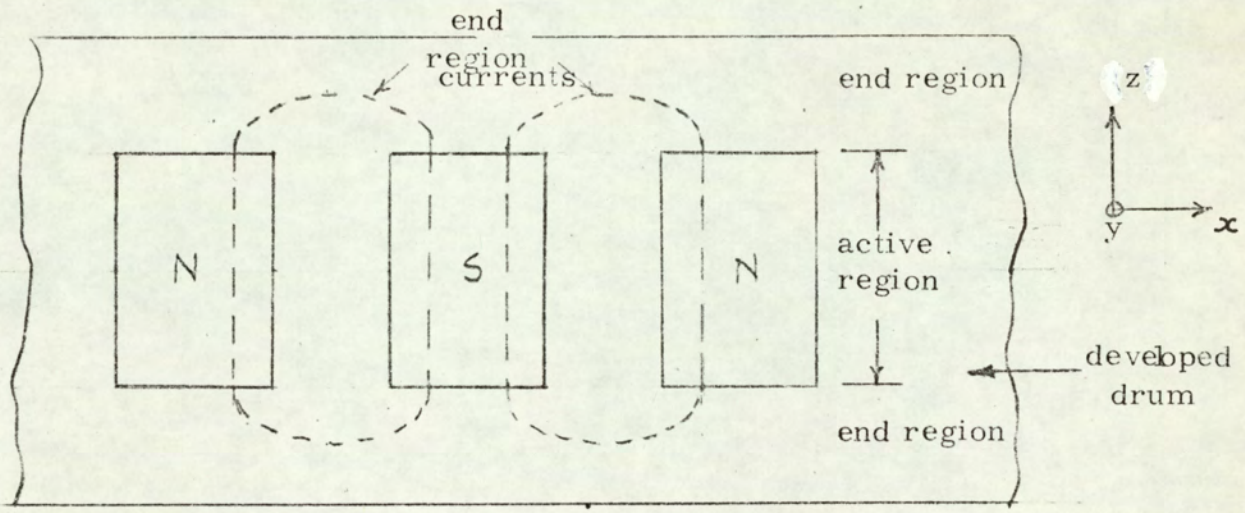

Figure 1.8

To allow for the finite axial length, Gibbs introduces the concept of end effects, that is, the effects of the eddy-currents flowing in the end regions. He assumes that these effects are wholly

outside the influence of the inducing field. This assumption ignores the eddy-current induction by pole-end fringing flux. He attempts to allow for end effects by increasing the resistivity of the drum material by a multiplier which is a function of the pole pitch and the active length. He also considers the harmonics in the flux density wave but his analysis is based on the standstill flux density distribution in the airgap, which he tacitly assumes to apply at all speeds. While this assumption may be virtually true at low speeds in inductor couplings, it is not valid for Lundell couplings (Reference 6, 8, 12). His theoretical calculations for an inductor coupling agree well with test results.

Davies[6, 8, 12] follows Gibbs' analysis up to the loss equation (1.9), and extends the treatment to include the space distribution of the eddy-currents and associated magnetising forces. Starting with the assumption of constant permeability, Davies derives the equation (from Section 3.6, Reference 6).

$$(\mu\mu_o)^{1/4} H_m = \sqrt[4]{\frac{8W^2}{\rho\omega}} \qquad (1.13)$$

where H_m is the peak value of magnetising force at the drum surface, $y = 0$. Davies found that a log-log plot of $(\mu\mu_o)^{1/4} H$ versus H, using values taken from the B-H curve for iron, was linear from H = 250 to 250 000 At/m. This range of H covers the B-H curve above the knee ($B > 1.2$ Wb/m^2), and he suggests that this is the region where couplings operate. Over this section of the B-H curve, therefore,

$$(\mu\mu_o)^{1/4} H = K H^m \qquad (1.14)$$

where K and m are constants, which for wrought iron are 0.97 and 0.77 respectively. By substituting (1.14) for $(\mu\mu_o)^{1/4} H$ in (1.13) and identifying H with the peak value, H_m, at the drum airgap surface he obtained

$$0.97 \; H_m^{0.77} = \sqrt[4]{\frac{8 W^2}{\rho \omega}} \qquad (1.15)$$

This enabled him to derive equations for torque and armature reaction, and expressions for peak torque and the speed at peak torque. Probably, the most important contribution by this author is the derivation of generalised equations for torque, flux per pole, and armature reaction, which, as will be shown later, provide a sound basis for design studies. These equations are given in Appendix A1.

Davies assumed purely axial eddy-currents and negligible end effects, which is equivalent to having zero-resistance endrings as shown in Figure 1.9, which implies that the ends of the active length of the drum are equipotentials. Since the current paths are parallel to the z-axis, it follows that the current density, J_z is constant along any line parallel to this axis and a quasi-two-dimensional treatment is justified.

To allow for end effects in the homogeneous drum which was used in the experimental work, Davies introduced two factors which he defined as follows.

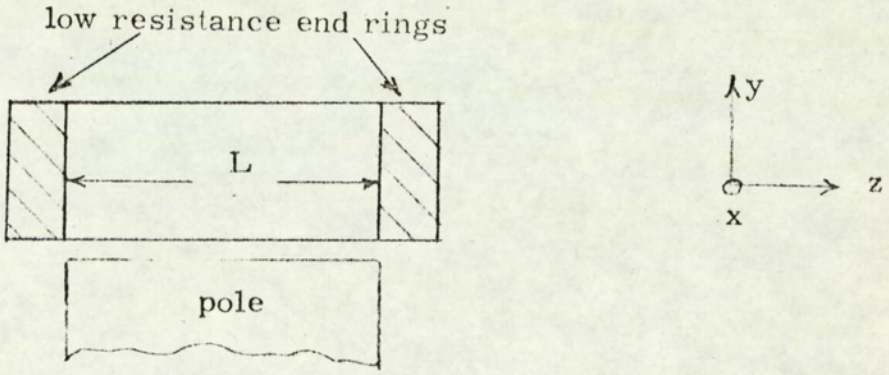

Figure 1.9

"Let r_1 be the multiplier of ϕ_{ac} to allow for the increased voltage which must be generated to circulate J_m through the impedance of the end region."

"Let r_2 be the factor by which the total drum loss must be divided to obtain the loss in the active region."

These factors must be evaluated from test results.

Davies' experimental work was extensive and introduced some new magnetic measurement techniques. By analysing the airgap flux density waves on load, he showed that, while harmonic content varied with slip frequency, the harmonic torque contribution was negligible.

Malti et al.[9] give a three-dimensional analysis of a coupling having a drum of finite length and constant permeability. The treatment of end effects and harmonics is implicit in their analysis which possibly accounts for their good correlation with test results at low excitations.

Gonnen et al.[11] deal with the analysis of a coupling operating at 1 p.u. slip, i.e. a brake. Their contribution to the subject is a method of accounting for the variation of permeability within the drum depth. The flux density decreases rapidly within the depth (Reference 6), and the permeability correspondingly increases. The authors represent the drum permeability by the expression $\mu = \mu_s e^{+\lambda y}$ where μ is the permeability at the airgap surface ($y = 0$), and λ is approximately equal to $1/d$. They include harmonics by superposition and show that the harmonic torque contribution, based on the field waveform on no load, is approximately 40%

Rudenberg's[1] work on eddy-current brakes (1906) was essentially along the lines discussed earlier, and his analysis did not lead to performance equations. Rosenberg[2] (1923) assumed arbitrary flux and current density distributions within the drum, and surprisingly his results compared favourably with tests. Sharov[4] deals with armature reaction in couplings. His expression for the armature reaction is similar to equation (1.8). He uses synchronous machine two-reaction vector diagrams to obtain the total excitation. Glazenko[5]

develops expressions for peak torque and the speed at peak torque. He derives expressions for harmonic torque in terms of harmonics in the induced eddy-current wave, which he assumes to have the same waveform as the inducing m.m.f. wave. His calculations include harmonics effects and agree well with his test results.

While not dealing specifically with couplings, the work of Angst[16] deals with end effects in solid rotor induction motors. Angst defines an end effect factor as the ratio of the impedance of the solid iron rotor with end effects to that without end effects. Constant permeability is assumed in this analysis, and the final expression for the end effect factor is complex. The author presents results for a rotor with and without copper end rings which agree well with his calculated values. The results also demonstrate the effectiveness of the copper end rings in minimising end-effects.

1.5 Purpose of this thesis

This thesis presents the results of

a) an experimental verification of Davies' generalised analysis of eddy-current coupling performance[12],

and b) a comparison of the performance of a coupling fitted with (i) a solid iron drum, and (ii) an iron drum with copper endrings, the copper endrings being a practical attempt to approximate to the idealised condition of endrings of negligible

resistance assumed by Davies[8].

For a), the coupling was comprehensively tested with the copper endring drum. Full details of the tests, together with their analysis and comparison with Davies' generalised analysis is given in Chapter 3.

In Chapter 4, an attempt is made to assess the effects of the end regions of the solid iron drum on the coupling performance. This assessment is based on a comparison of test results for the endring drum with those obtained by Davies[6] for a solid iron drum. As significant differences were found between the performances with the two drums, particularly with respect to the torque-speed characteristic, it would obviously be of considerable practical value if a simple method were available for assessing quantitatively the effects of the end regions. Such a simple method appeared to be offered by Gibbs[3] "resistivity multiplier"*, and the latter part of Chapter 4 is devoted to examining the accuracy of the multiplier. A simple alternative method for estimating the end region to active region loss ratio is also presented.

Some tests designed to study the end region field distribution are also presented in Chapter 4.

---

* The "resistivity" multiplier is a factor by which the resistivity of the drum active region is multiplied to allow for end region effects.

CHAPTER 2 The experimental machine

2.1 Rotating drum; stationary field

The experimental Lundell coupling was designed by Davies;[6] a cross-section of the arrangement is shown in Figure 2.1. The wrought iron drum was mounted on a non-magnetic stainless steel backplate on the drive shaft to minimise magnetic leakage flux. The backplate carries a guide bearing which supports the shaft of the pole member. The drum was driven by a variable speed d.c. motor through a shaft which was supported in two bearings situated in the bearing frame.

The field member which rotated within the drum is separated from it by an airgap of 0.25 mm. The shaft carrying the fieldmember was mounted between the guide bearing whose outer race rotated with the drum, and a plummer block mounted on a steel pillow. The field member was held stationary while the drum rotated. This was done by fixing one end of a torque arm to the outboard end of the shaft and the other to a pan of a precision weighing scale. Resistance strain gauges were fixed to the top and bottom surfaces of the torque arm and connected to form a strain-gauge bridge. This bridge was supplied from a stabilised d.c. source. The torque on the shaft bent the torque arm and an output from the bridge, proportional to the torque, was fed to an x-y plotter. The coupling assembly was mounted on a substantial baseplate. The plate carrying the bearing

LAYOUT OF TEST MACHINE (ROTATING DRUM)

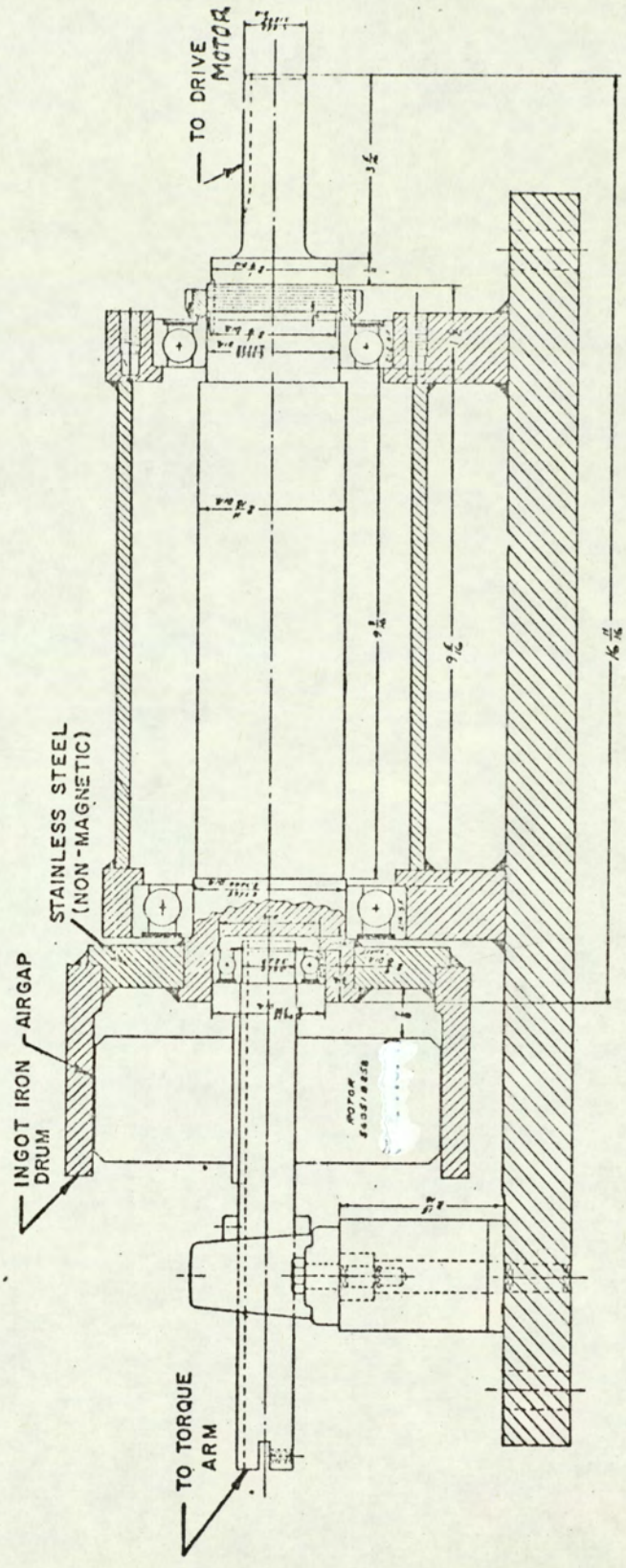

FIGURE 2.1

assembly was welded to the baseplate and the plummer block assembly was fixed to the baseplate by screws. The complete rig was mechanically very robust. A new drum with copper endrings and shaft assembly was made for this project. The coupling had a nominal rating of 1 hp.

The rig was used for the following measurements;

(a) airgap flux-density distributions at various field currents and slip-speeds,

(b) the field core flux,

(c) torque-speed curves.

2.2 Stationary drum; rotating field

Davies[6] also designed a second model with a stationary drum. The field member which was driven by the d.c. motor was common to both rigs. The direct current to the field winding was supplied through slip-rings. A cross-section of this arrangement is shown in Figure 2.2. Davies[6] used this rig to measure J at the drum surface and the flux distribution in the drum depth in the active region.

The same rig, with minor modifications, described in Section 2.7, was used to investigate the end-region field distributions.

2.3 The field member

Details of the field member are shown in Figure 2.3. The magnetic circuit design provided ample flux-carrying cross-

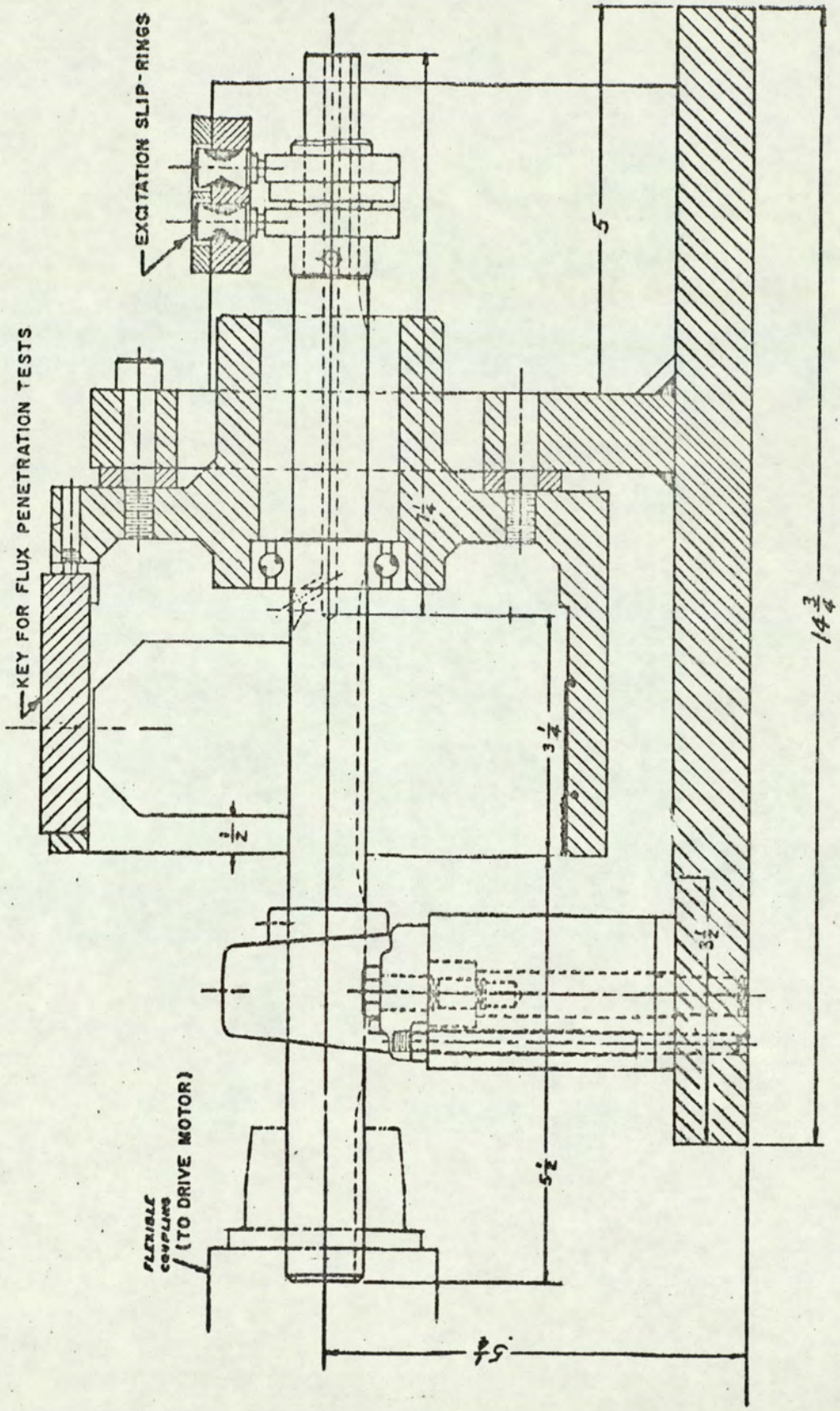

LAYOUT OF TEST MACHINE (STATIONARY DRUM)

FIGURE 2.2

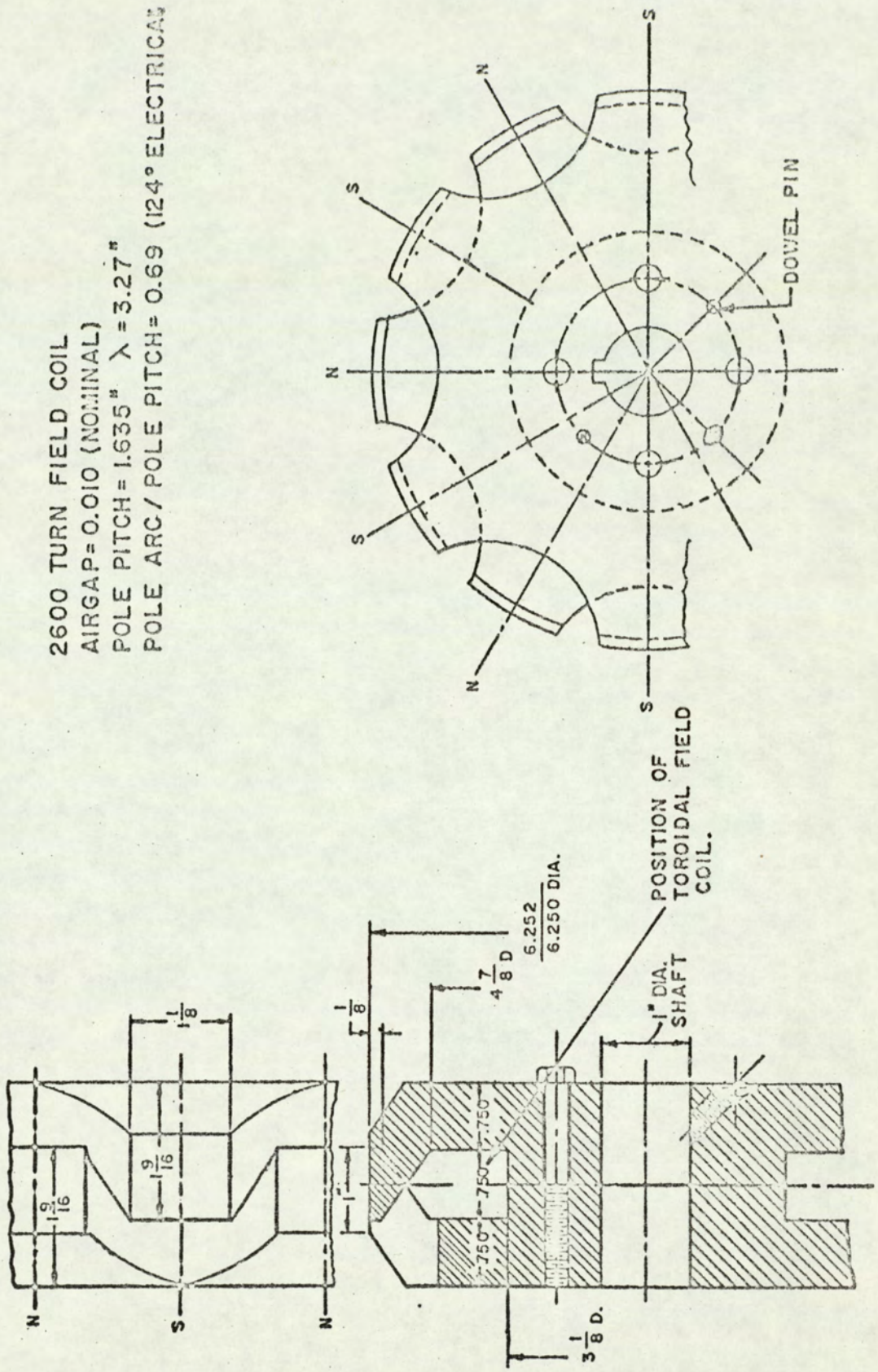
DETAILS OF POLE MEMBER OF EXPERIMENTAL MACHINE
2600 TURN FIELD COIL
AIRGAP = 0.010 (NOMINAL)
POLE PITCH = 1.635" λ = 3.27"
POLE ARC / POLE PITCH = 0.69 (124° ELECTRICAL)
DOWEL PIN
POSITION OF TOROIDAL FIELD COIL.
1" DIA. SHAFT
6.252
6.250 DIA.
4 7/8 D
3 1/8 D.
1 1/8
1 9/16
1"
.750
N
S

FIGURE 2.3

sections to minimise iron saturation. This was essential as we were interested in relating torque to the airgap flux and, if a large proportion of the field m.m.f. were absorbed in the field iron, the airgap relationships would be obscured.

The pole faces were designed to be approximately square as a compromise between short length to minimise pole leakage and long poles to reduce end-effects.

2.4 The coupling drive

The coupling was comprehensively tested over a speed range of 0 - 1500 r.p.m. (0 - 150 Hz). The coupling drive consisted of a substantial d.c. motor with manual Ward-Leonard speed control. The motor field was separately excited from the a.c. mains through a full-wave silicon rectifier. The motor armature was fed from a 3-phase full-wave bridge-connected rectifier supplied from the mains through a motorised variac driven at one revolution per minute, which enabled the motor to be run up smoothly. It was later found necessary to interpose a transformer between the supply and the variac for finer speed control. A precision d.c. tachometer was directly coupled to the d.c. motor shaft and its output signal was fed to an x-y plotter through a potentiometer. To avoid dangerous speed rises due to accidental tripping of the field, the armature and field supplies were interlocked. The circuit diagram is shown in Figure 2.4. The rig performed satisfactorily throughout the test programme.

SCHEMATIC DIAGRAM FOR EDDY CURRENT COUPLING TEST RIG

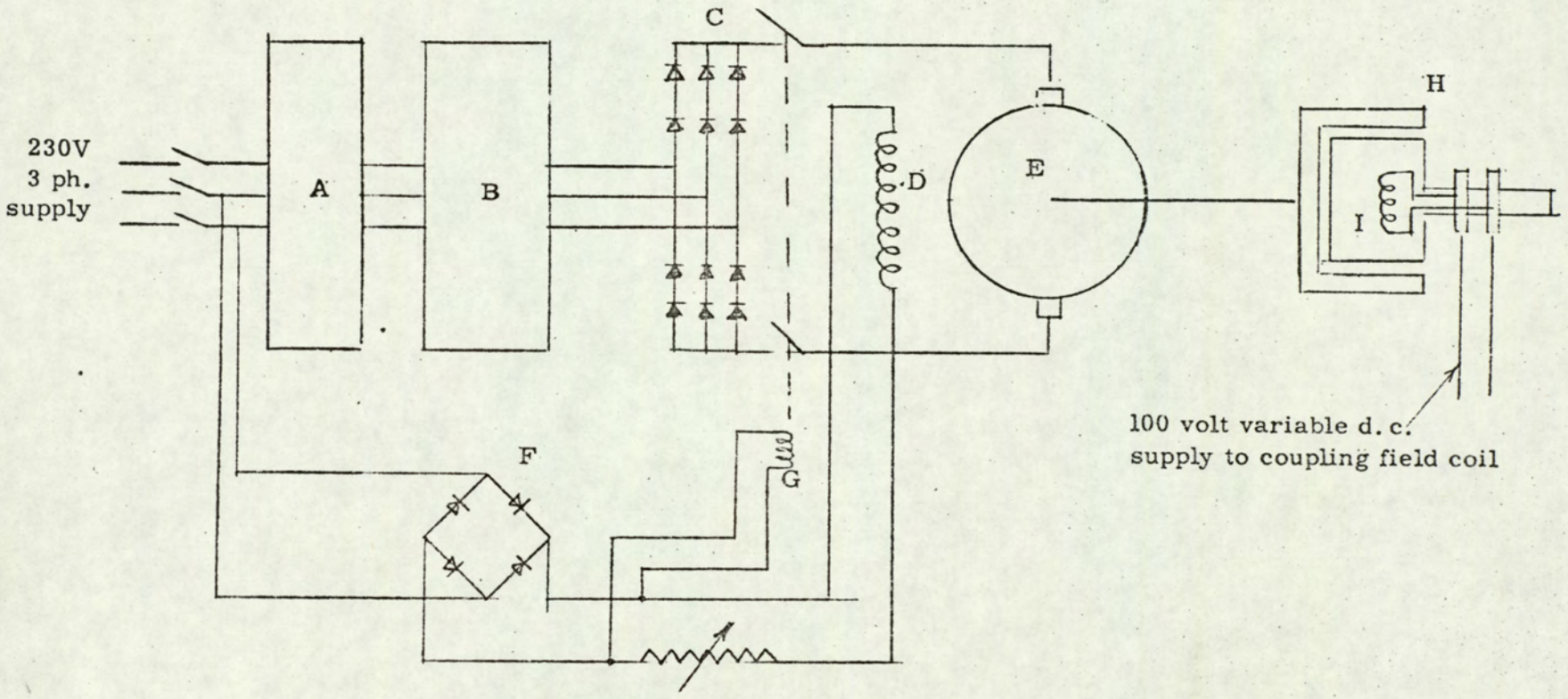

A 3 ph. variac B - 3 ph. transformer C - 3 ph. full wave rectifier D - d.c. motor field
E d.c. motor F - single phase rectifier for d.c. motor field G - motor armature contactor coil
H- coupling drum I - coupling field coil

Figure 2.4

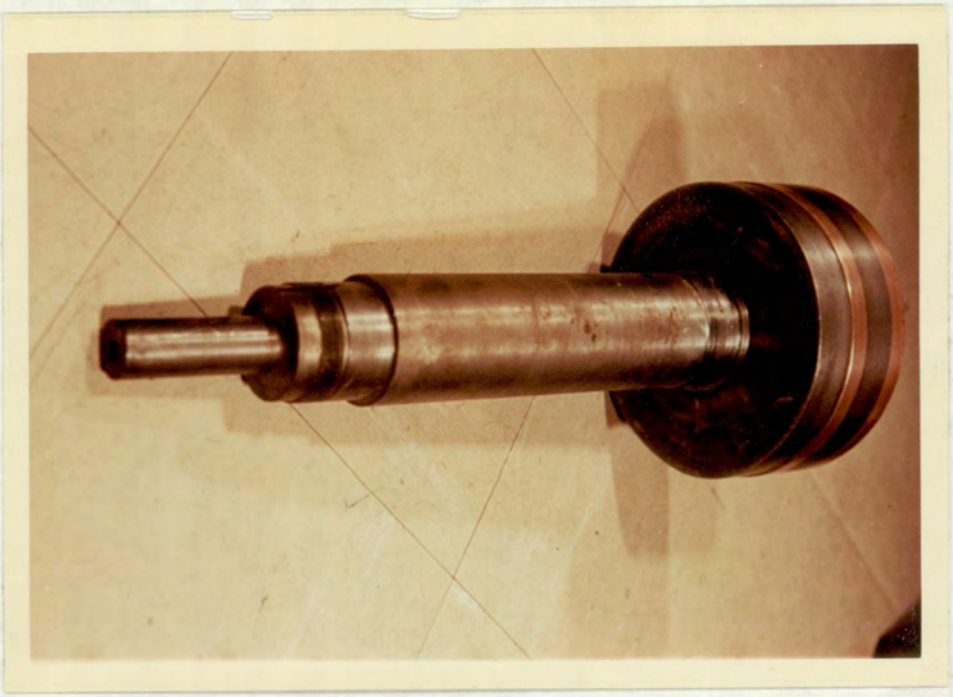

Plate 2

Endring drum

2.5 Endring drum construction

The active section of the experimental drum was made of wrought iron and was machined from the solid to avoid welded joints. Copper endrings were brazed to ends of the wrought iron section. The mating faces of the wrought iron section and the copper rings were machined accurately and brazed by a vacuum process. A colour photograph of the drum is shown in Plate 2.

2.6 Search Coils

2.6.1 Pole face flux distributions

Figure 2.5(a) shows the search coil configuration used to measure the circumferential distribution, and Figure 2.5(b) shows that used for the axial distribution. All the search coils were held in position by epoxy resin. The leads were twisted together to reduce pick-up and connected to a multi-contact rotary switch. This search coil arrangement was first used by Davies.

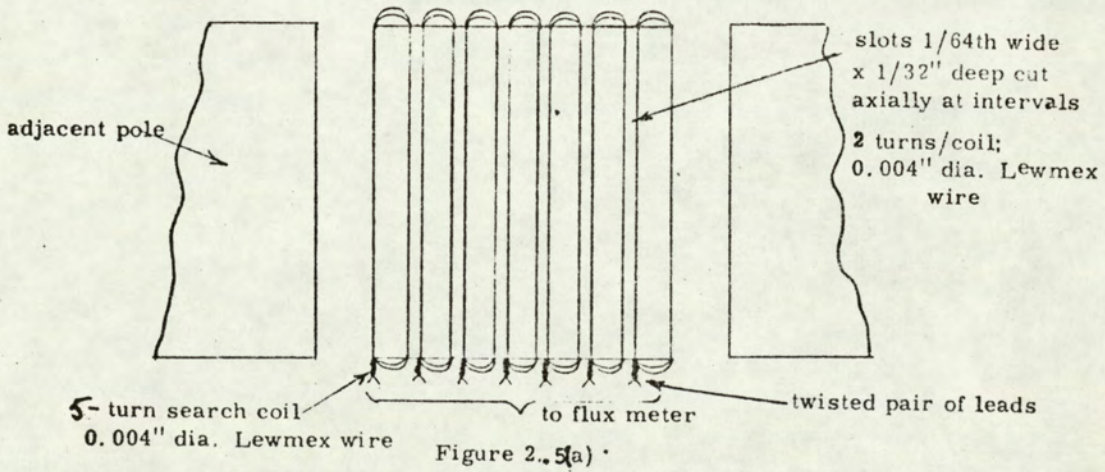

Figure 2.5(a)

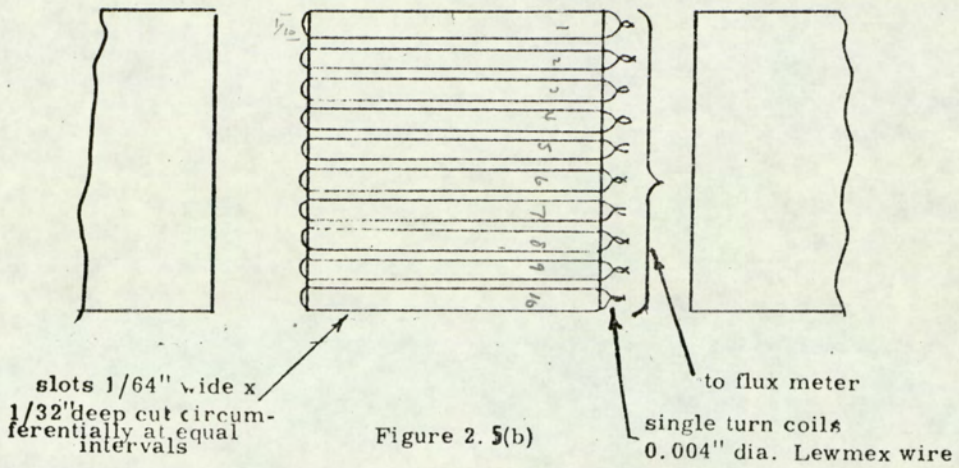

Figure 2.5(b)

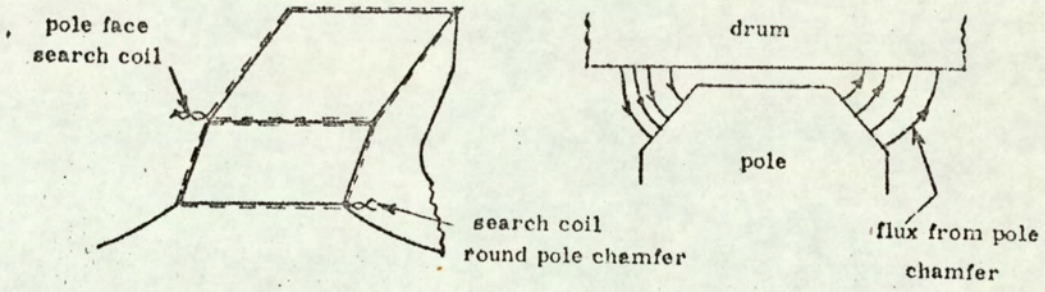

Figure 2.6

2.6.2 Pole-chamfer fringing flux

Figure 2.6 shows the single-turn search coils used for the measurement of the pole-chamfer and the corresponding pole face fluxes.

2.6.3 Total pole and core fluxes

The flux through all the poles (six) of the same polarity and the corresponding core fluxes were measured using the search

coils shown in Figure 2.7(a) and 2.7(b) respectively.

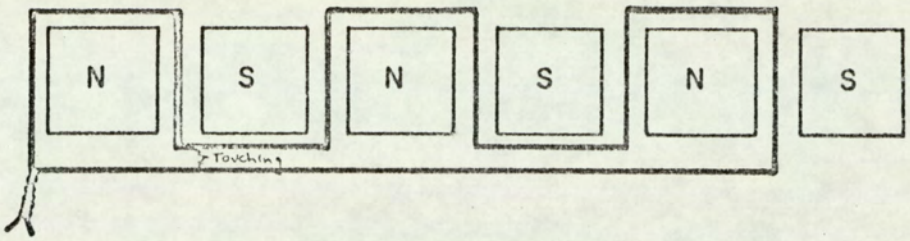

(a) Search Turns to measure Total Flux from all N poles. (Note that end connections are arranged not to link with axial leakage flux). In actual machine, there are 12 poles.

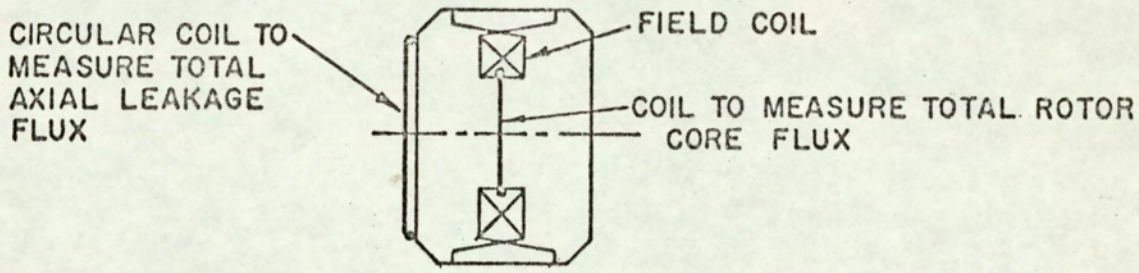

(b) Search coils measuring rotor core flux and axial leakage flux.

FIGURE 2.7

2.7 End region investigations

2.7.1 Axial flux density distributions

Davies'[6] solid stationary drum was used for these tests. Thirteen 0.635 mm (0.025 in.) diameter holes were drilled at 2.54 mm (0.1 in.) centres along an axial line in the

end region. The 'spongy' nature of the wrought iron made the drilling difficult and smaller diameter drill bits were not suitable. The layout of the search coils is shown in Figure 2.8.

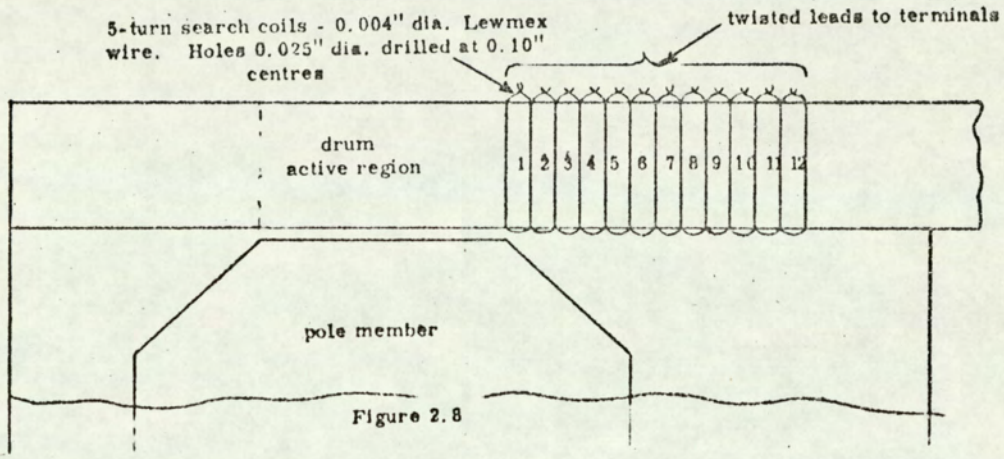

Figure 2.8

2.7.2 Radial flux density distributions

Davies[6] used a precision ground key with axial slots to locate the search coils to measure the radial flux-density distribution in the active region. This key was located in an axial keyway in the drum and extended well into the end region and this part of the key was used to place search coils to measure

the radial flux-density distribution in the end region. Axial slots were cut in the key to receive the search wires as shown in Figure 2.9. At one end, the search wires were twisted and soldered together to form a common electrical connection and, at the other end, the wires were taken through a radial slot in the key to terminals. Any pair of terminals will form a search coil. The search coil layout is shown in Figure 2.10.

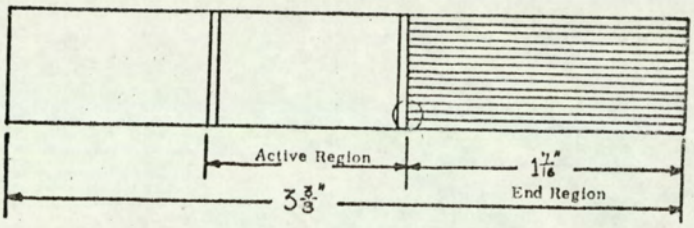

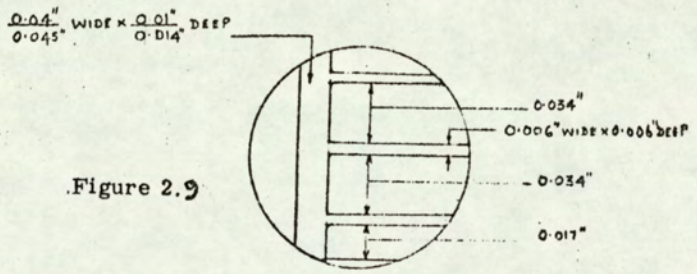

Figure 2.9

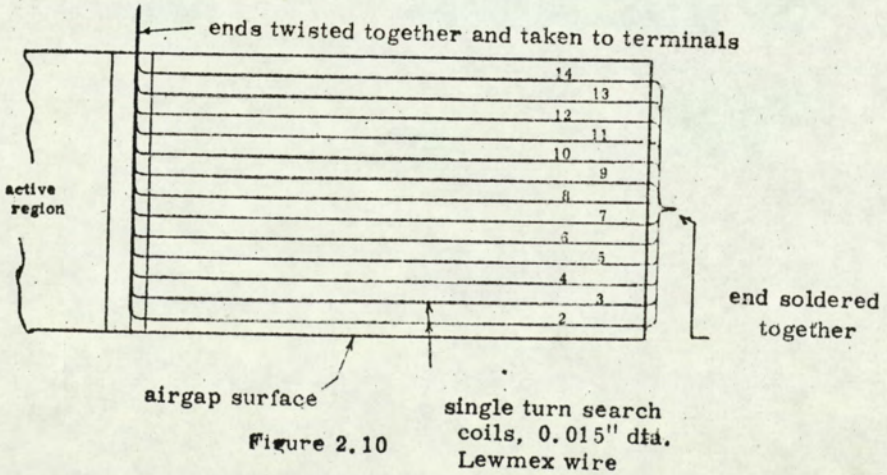

Figure 2.10

2.7.3 General precautions

The fine insulated wires used for the search coils required very careful handling, and it was necessary to smooth all rough edges in slots and holes to avoid damage to the insulation. The search coil leads were carefully twisted together to minimise stray pick-up. Excessive heating of the drum was avoided as this would have damaged the search coils.

2.8 Flux measurements

2.8.1 Field member stationary

The Norma fluxmeter was used to measure the fluxes with the field member stationary. It was possible to use field polarity reversal to produce flux changes through the search coils under both static and dynamic conditions since the coupling torque is independent of field polarity.

2.8.2 Drum stationary

The induced voltages in the end-region search coils alternate at slip frequency and the waveforms of the induced voltages were seen to have a large harmonic content. Flux calculations based on measured voltages would therefore have been inaccurate. A high gain operational amplifier was used as an integrator, the output being fed to an oscilloscope with accurate calibration facilities.

2.9 Torque measurement

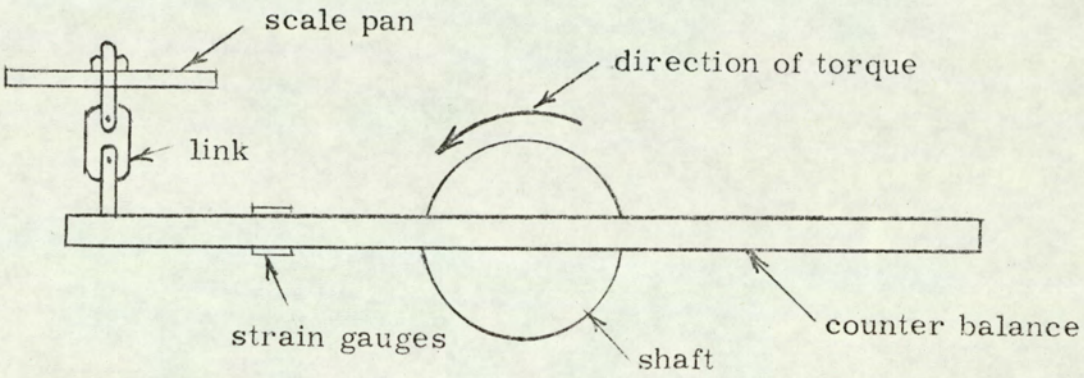

Figure 2.11

The torque arm consisted of an 0.47 cm x 1.27 cm (3/16 in. x 1/2 in.) mild steel bar. The field-member shaft end was slotted to carry the torque arm, which projected an equal distance on each side of the shaft axis to provide its own counter-balance. One end of the arm was fixed to the pan of a precision balance ($\pm$ 5 gm) through a pivoted link as shown in Figure 2.11.

Four resistance strain gauges, two on the top side and two on the underside of the arm, were fixed with epoxy resin. When the torque-arm was bent, the resistance of the top strain gauges decreased (due to compression) and that of the bottom gauges increased (due to tension). The four gauges were connected to form a bridge, Figure 2.12, which was supplied from a stabilised d.c. source.

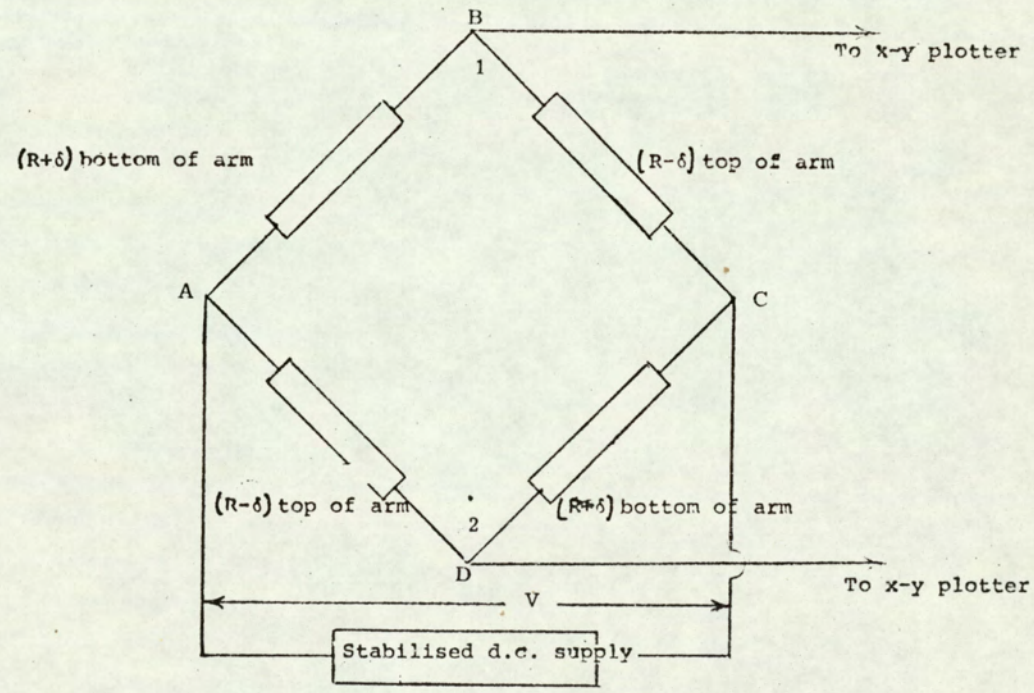

δ. change in resistance
R- normal resistance of strain-gauge.

FIGURE 2.12

The output from the bridge was fed to an x-y plotter. The arrangement is similar to that used in Reference 6, except that all the four gauges were active in this bridge.

2.10 Eddy-current distribution

Eddy-currents on the drum surface obey Ohm's Law for fields, $\overline{E} = \rho \overline{J}$. Davies[6] describes 'E-probes' fixed to the drum inside surface. An E-probe was designed to investigate the eddy-current distribution in the end regions, and over the back surface of the drum. A cross-section of this probe is shown in Figure 2.13.

The probe consisted of a bakelite ring (1) about 2.54 cms diameter x 2.54 cms thick. Two concentric holes (2), 0.5cm centres were drilled to take hypodermic needles (3). Lewmex wires[6], 0.038 mm (.0015"), were carefully soldered to the top of the needles and were threaded through the central holes in the needles. Two springs (4) were placed on top of the needles and held in position by screwing the bakelite handle (5) to the base ring. The two copper wire leads were soldered on to a screened cable.

2.11 Equipment calibrations and specifications

2.11.1 Torque

The strain gauge bridge output was fed to a d.c. millivoltmeter. After first levelling the precision balance, the coupling was run through a range of torques. Corresponding

CROSS SECTION OF 'E' PROBE.

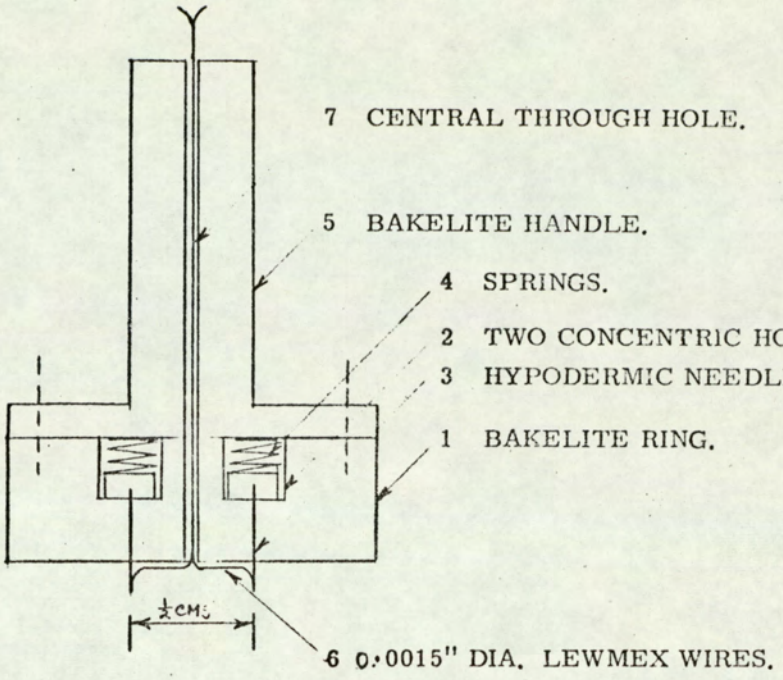

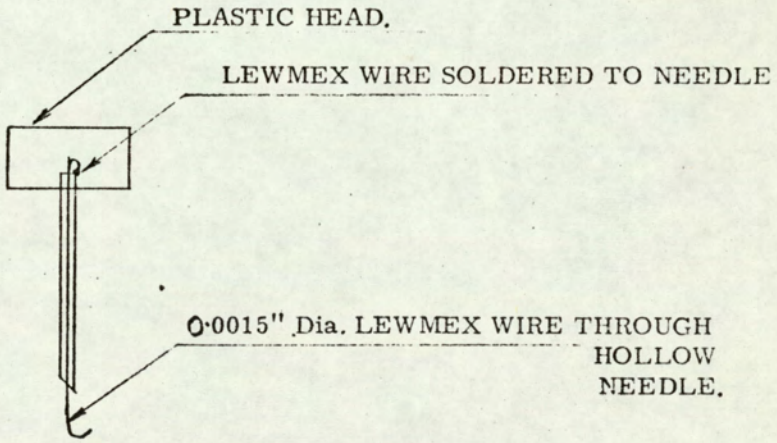

ENLARGED VIEW OF HYPODERMIC NEEDLE WITH SEARCH WIRE.

FIGURE 2.13

readings of the strain gauge output and the balance scale are shown in Figure 2.14. The calibration was checked over a period of time, taking precautions to minimise drum heating.

2.11.2 Flux-meter

A Hibbert magnetic standard was used to check the calibration of the flux-meter, and it was found that the meter calibration was within 1% of the standard over the entire scale range. When the flux-meter was connected to the search coils, it was necessary to add external resistance so that the total input resistance could be set to 30 ohms as specified by the makers.

2.11.3 Integrator

Tektronix type 'O' operational amplifier was used as an integrator. The specification of the amplifier is as follows.

Open loop gain	2500
Input impedance (internal values)	0.01, 0.1, 0.2, 0.5 and 1.0 Meg. Ohm.
	10 p.F., 0.0001, 0.001, 0.01, 0.1 and 1.0 μF at $\pm$ 1%.
Feedback impedance	same values and tolerances as the input impedances internally.

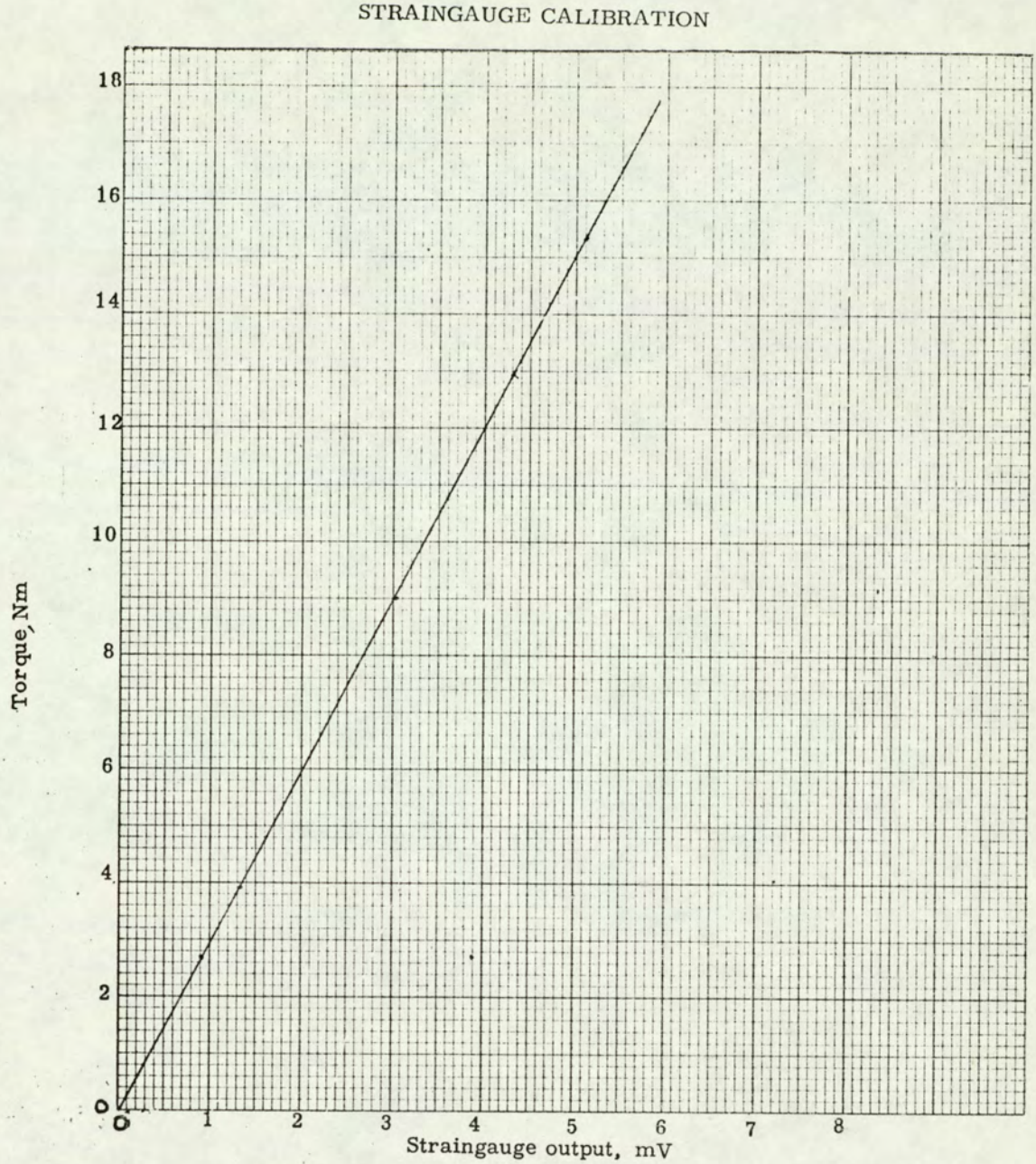
STRAINGAUGE CALIBRATION
Torque, Nm
0
2
4
6
8
10
12
14
16
18
0
1
2
3
4
5
6
7
8
Straingauge output, mV

Figure 2.14

2.11.4 x-y Plotter

Brief technical data of the x-y plotter are as follows:-

Input resistance	10 000 Ohm across variable attenuator
Speed	7.5 inches/sec. (max.)
Accuracy	$\pm$ 0.5% dynamic at constant velocity to 7.0 inches/sec.

2.11.5 Tachogenerator

The slip-speed signal was obtained from a direct-coupled precision tachogenerator with the following specifications:

Open circuit output	0.1 volt/r.p.m.
Maximum speed	4 000 r.p.m.
Maximum current	0.1 A.

As the maximum input to the x-y plotter was in the region of 100 mV, the tachogenerator output was fed to the plotter through a suitable potentiometer.

2.12 Details of experimental couplings

Drums	Solid	End Ring
drum material	wrought iron	wrought iron
drum diameter (I.D.)	15.875 cm (6.25 in.)	15.875 cm (6.25 in.)
drum thickness	1.27 cm 0.5 in.)	1.27 cm (0.5 in.)
active length of drum	2.54 cm (1.0 in.)	2.54 cm (1.0 in.)
copper ring cross section	-	1.27 cm x 1.27 cm

Pole member (common to both drums)

Type	Lundell
Number of poles (2p)	12
Pole pitch ($\lambda/2$)	4.15 cm (1.63 in.)
Pole face	2.54 cm x 2.875 cm (1.0 in. x 1.125 in.)
Pole arc/pole pitch	0.68
Length/pole pitch	1.63
Number of turns on field coil	2600
Slip frequency (Hz)	Slip speed in r.p.m. x 10^{-1}

Chapter 3 Tests with endring drum

3.1 Standstill magnetisation tests

Davies'[6] experimental work was on a solid drum, and to compare his results directly with those presented here it was essential to establish that the initial conditions were the same in the two experimental couplings. Since the field member was common to both couplings, it was sufficient to establish that the standstill magnetic conditions in the airgaps of the two experimental couplings were the same. This was done by measuring the core flux, and the flux through all six poles of the same polarity, at different field currents. The search coils described in Section 2.6.3 were used for these tests. The difference between the core flux and the flux through half the poles represents the leakage flux discussed in Appendix A.3.

The standstill pole and core fluxes for the two couplings are given in Tables 3.1 and 3.2.

Table 3.1

Field current, A	Flux through six poles, m.Wb		Percentage difference *
	Endring drum	Solid drum (from Ref. 6)	
0.1	2.05	2.0	2.44
0.2	3.8	3.7	2.63
0.3	4.73	4.6	2.75
0.4	5.1	4.95	2.94

Table 3.2

Field current, A	Core flux, mWb		Percentage difference *
	Endring drum	Solid drum (from Ref. 6)	
0.1	2.75	2.7	1.82
0.2	5.1	5.0	1.96
0.3	6.61	6.5	1.66
0.4	7.3	7.2	1.37

* The endring drum results are the base values.

These tables show that the discrepancies between the two couplings were sufficiently small to be considered negligible.

The results of similar flux tests under 'load' conditions are given in Figures 3.1 and 3.2, which clearly show the effects of eddy-current reaction on the airgap flux.

3.2 Pole-chamfer fringing flux

The search coils described in Section 2.6.2 were used to measure the fringing flux from the pole chamfer and the corresponding pole-face flux in the airgap. The fringing flux was less than 3% of the pole-face flux, and it was considered reasonable to assume that it would have a negligible effect on both the torque and end region-field.

3.3 Torque-speed curves

Torque-speed curves were obtained by first setting the field current to a desired value, and then increasing the slip-speed of the coupling progressively from zero up to a maximum. The speed and the torque signals were fed to

TOTAL AIRGAP FLUX FROM HALF THE ROTOR POLES AS A FUNCTION OF FIELD CURRENT, AT VARIOUS SPEEDS

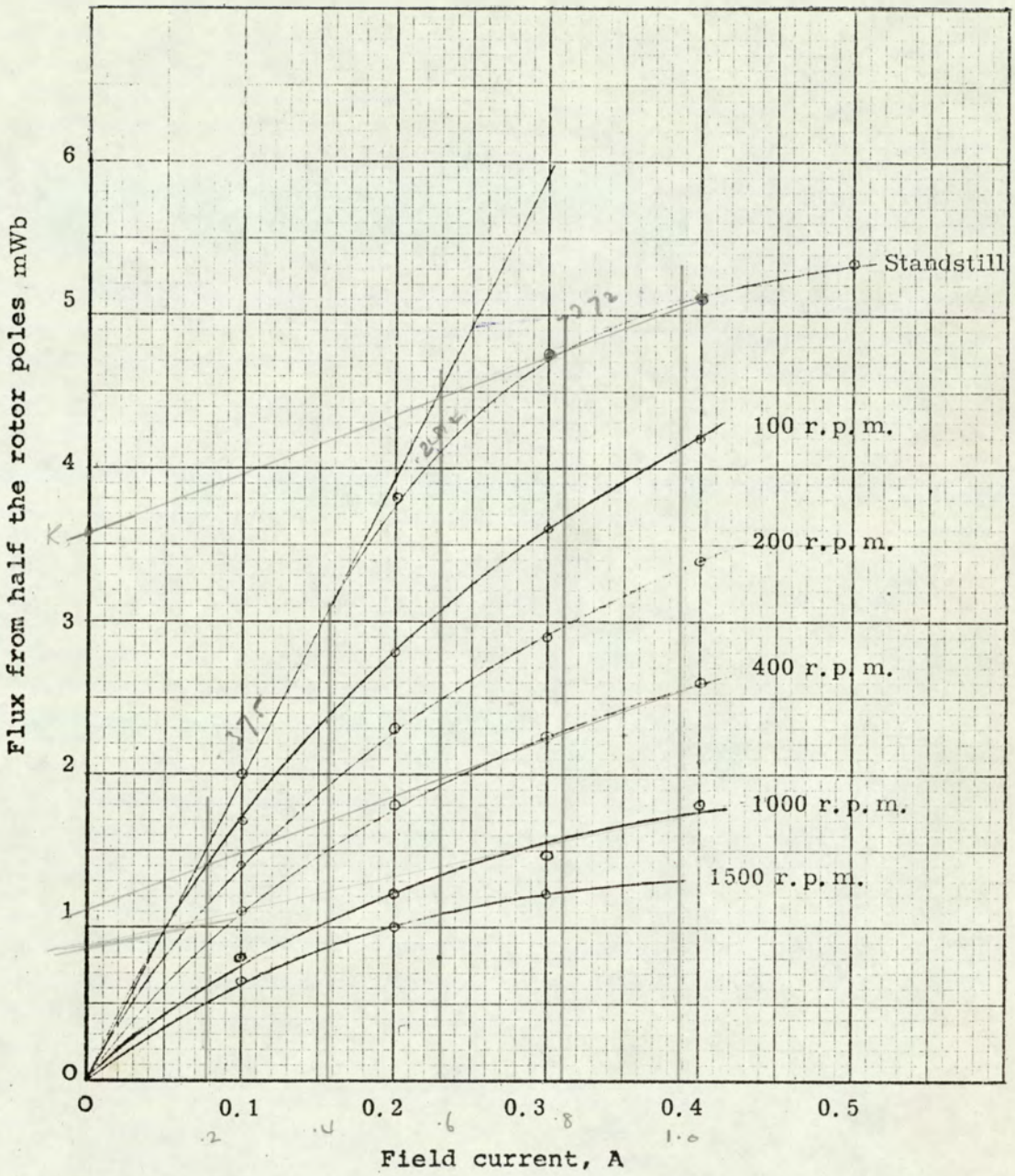

FIGURE 3.1

TOTAL FLUX THROUGH ROTOR CORE AS A FUNCTION OF FIELD CURRENT AT VARIOUS SPEEDS

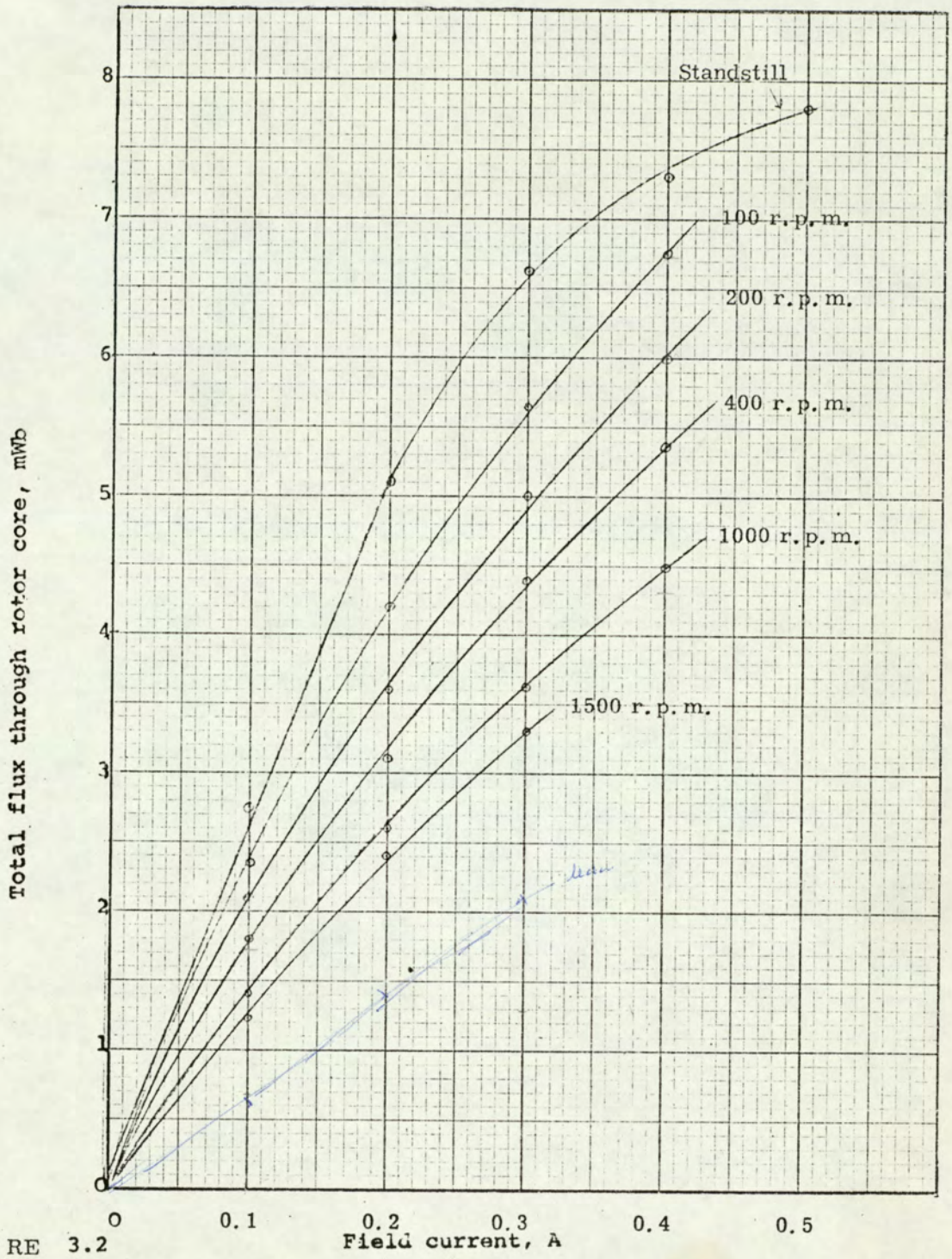

FIGURE 3.2

the x-y plotter.

As the drum was cooled naturally it heated up quickly, particularly at high slip-speeds. The increase in resistivity due to this heating reduced the torque and it was necessary to carry out the tests as quickly as possible. Before each run up the drum was first cooled by running unexcited until the drum outer surface temperature was 30^{o} C.

The torque-speed curves are shown in Figure 3.3. For ease of comparison, two sets of torque-speed curves for the solid and endring drums are shown in Figure 3.4. From these figures, the following initial conclusions can be drawn.

(a) The peak torques (T_m) of the two couplings are the same to within about 5%.

(b) The speeds at which peak torques occur with the solid drum are considerably higher than those with the endring drum.

(c) At lower slip-speeds, the torques with the solid drum are much less than those with the endring drum.

Torque-speed curves are discussed further in Section 3.8 and 3.9.3.

3.4 Circumferential pole-face flux distributions on load

The search coils used for these tests are described in Section 2.6.1. For each value of field current and slip-speed, the flux linking each search coil on the pole face was measured. These fluxes were converted to flux densities

TORQUE-SPEED CURVES FOR VARIOUS EXCITATION FOR END RING DRUM COUPLING.

EACH RUN STARTED WITH DRUM TEMP. AT 30°C. FIGURES INSIDE BRACKETS SHOW FINAL TEMPERATURES.

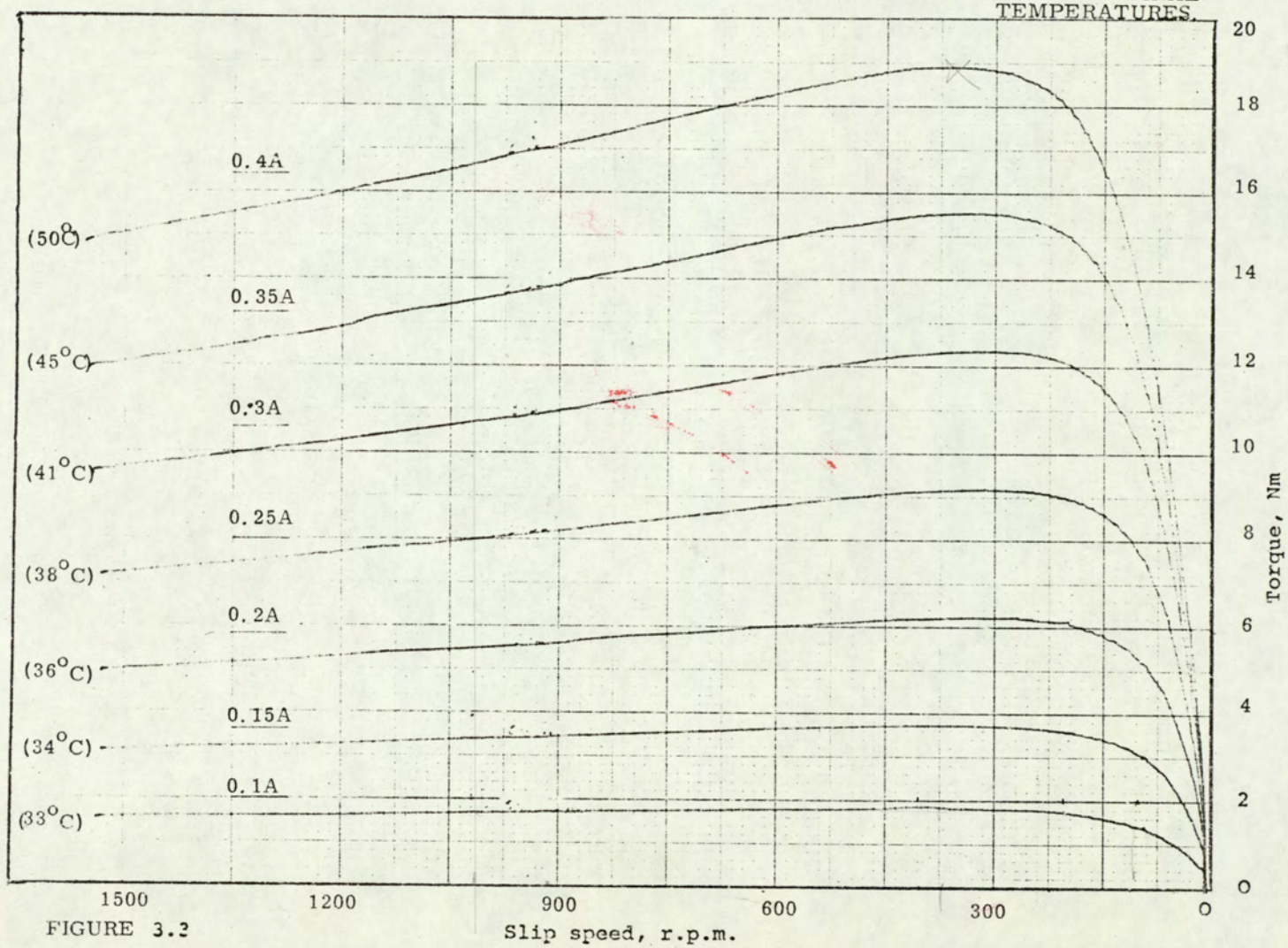

FIGURE 3.2

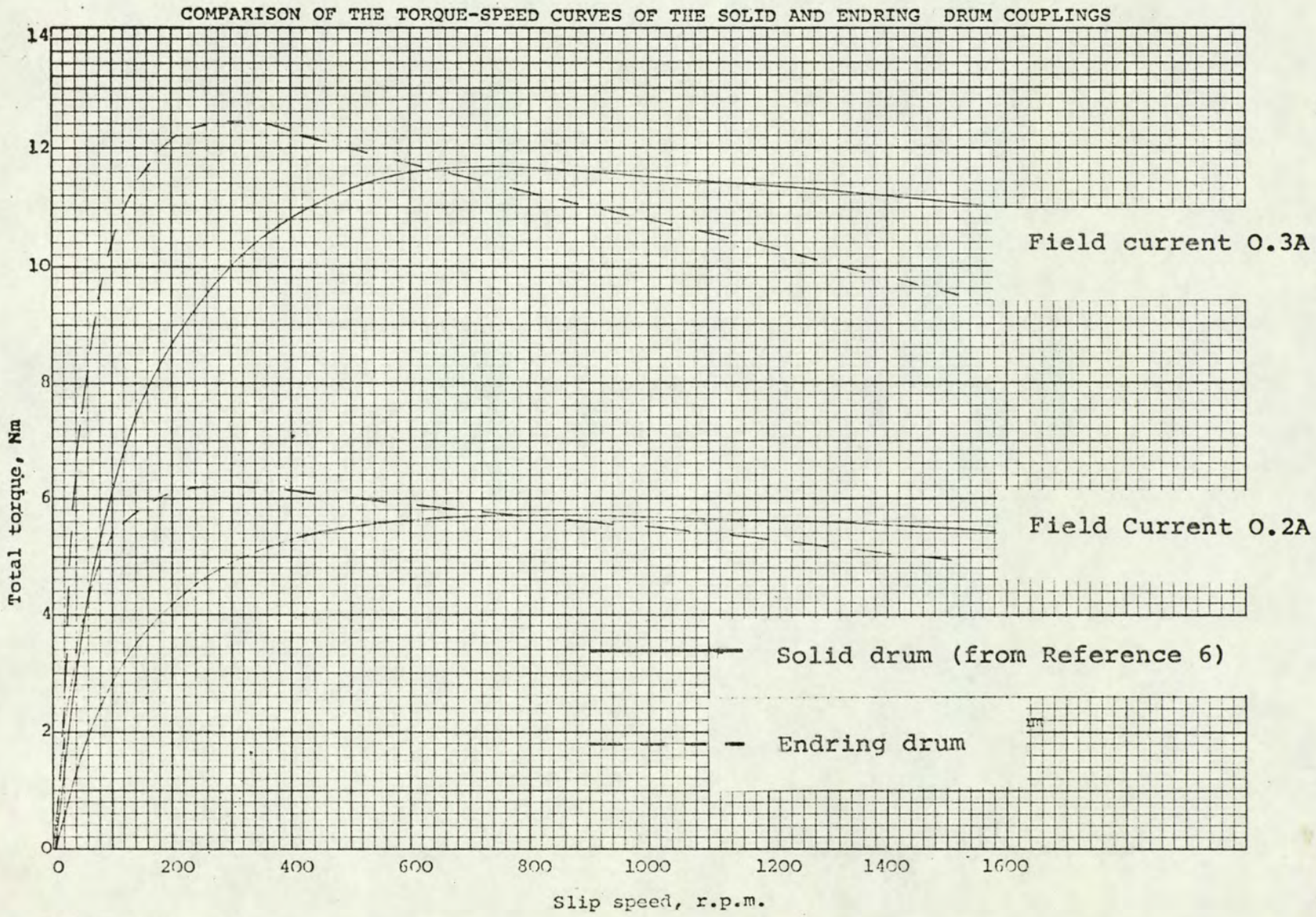
COMPARISON OF THE TORQUE-SPEED CURVES OF THE SOLID AND ENDRING DRUM COUPLINGS
Total torque, Nm
Slip speed, r.p.m.
0
2
4
6
8
10
12
14
0
200
400
600
800
1000
1200
1400
1600
Field current 0.3A
Field Current 0.2A
Solid drum (from Reference 6)
Endring drum

FIGURE 3.4

by dividing each of them by the area of the corresponding search coil.

Since these flux densities represent average values over the search coil areas, their distribution across the pole face should be represented by a histogram as shown in Figure 3.5.

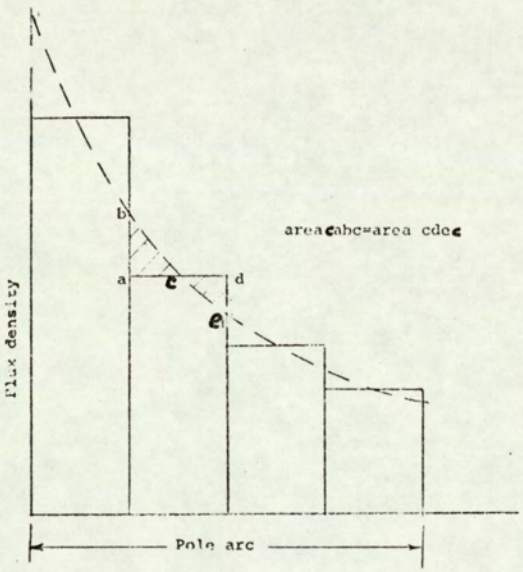

Figure 3.5

The actual distribution is smooth, which raises a problem as to how to construct a curve which is approximate to the true curve. A smooth curve could be constructed by using 'equal-area criteria', that is, determining a point such as C on the curve by making the area cabc equal to the area cdec. Such a curve is shown dotted

in Figure 3.5. Alternatively, the average flux densities could be plotted in the centres of the search coil spans. Harmonic analyses of the load flux-density distributions drawn using both these methods showed negligible differences in the harmonic content. However, since Davies[6] used the second method, it was decided to do the same.

The load flux-density distributions are shown in Figures 3.6(a) to (g). The mean flux densities for each value of field current at standstill are also plotted. Tests showed that the interpolar flux was negligible and therefore it was assumed that the airgap flux was confined to the pole face. The load flux-density distributions show clearly the effects of eddy-current armature reaction.

These curves are similar to Figures 12. to 16 of Reference 6. Those for the endring drum show greater armature reaction, which is consistent with the reduction in end region impedance produced by using copper endrings.

The load flux-density distributions were analysed to obtain the fundamental and harmonic components of the airgap flux density, the peak eddy-current armature reaction, and the displacement of the armature reaction wave with respect to the polar axis. The results of this analysis are considered in the following sections.

The tests covered the slip-frequency range 1 - 150 Hz. As far as is known, this is the first time that coupling performance has been investigated down to 1 Hz. This wide range

LOAD FLUX DENSITY DISTRIBUTION ACROSS POLE FACE
AT VARIOUS SPEEDS AT CONSTANT EXCITATION.
FIELD CURRENT 0.2A (260 AT/POLE).
LOW FREQUENCY OPERATION.
(END RING DRUM).

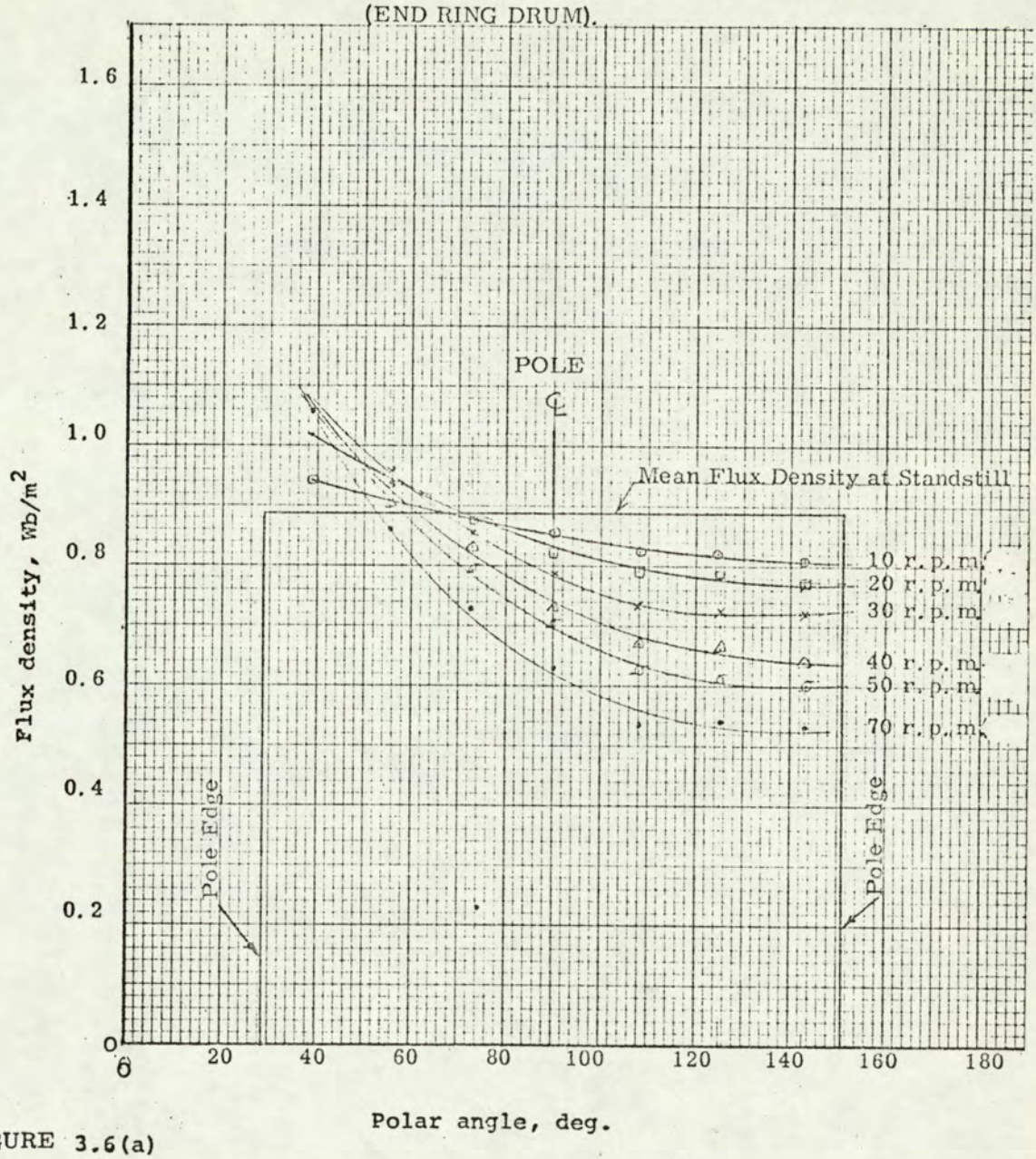

FIGURE 3.6(a)

LOAD FLUX DENSITY DISTRIBUTION ACROSS POLE FACE
AT VARIOUS SPEEDS AT CONSTANT EXCITATION.
FIELD CURRENT 0.3A (390 AT/POLE).
LOW FREQUENCY OPERATION.
(END RING DRUM).

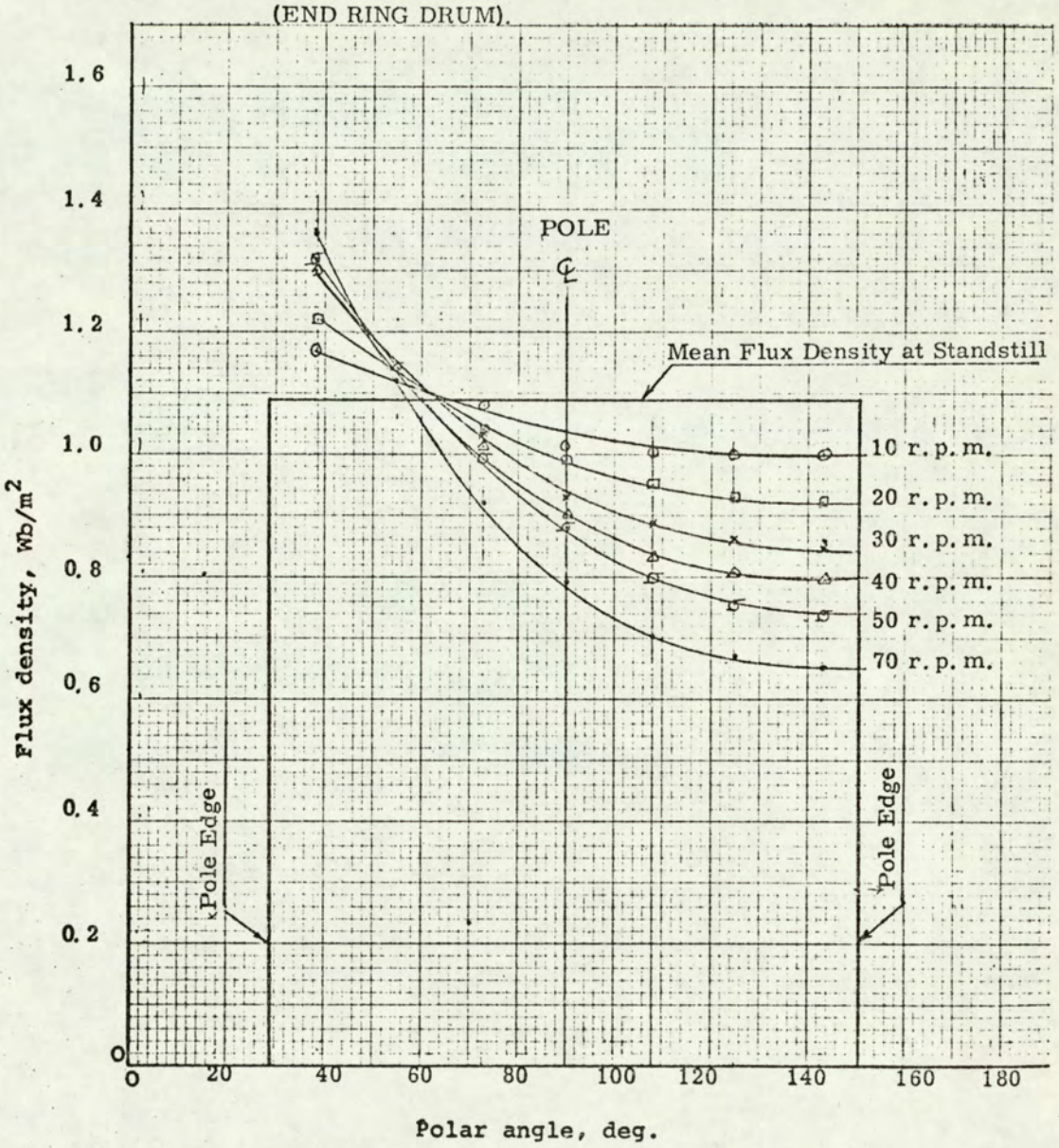

FIGURE 3.6(b)

LOAD FLUX DENSITY DISTRIBUTION ACROSS POLE FACE
AT VARIOUS SPEEDS AT CONSTANT EXCITATION.
FIELD CURRENT 0.4A (520 AT/POLE).
LOW FREQUENCY OPERATION. (END RING DRUM).

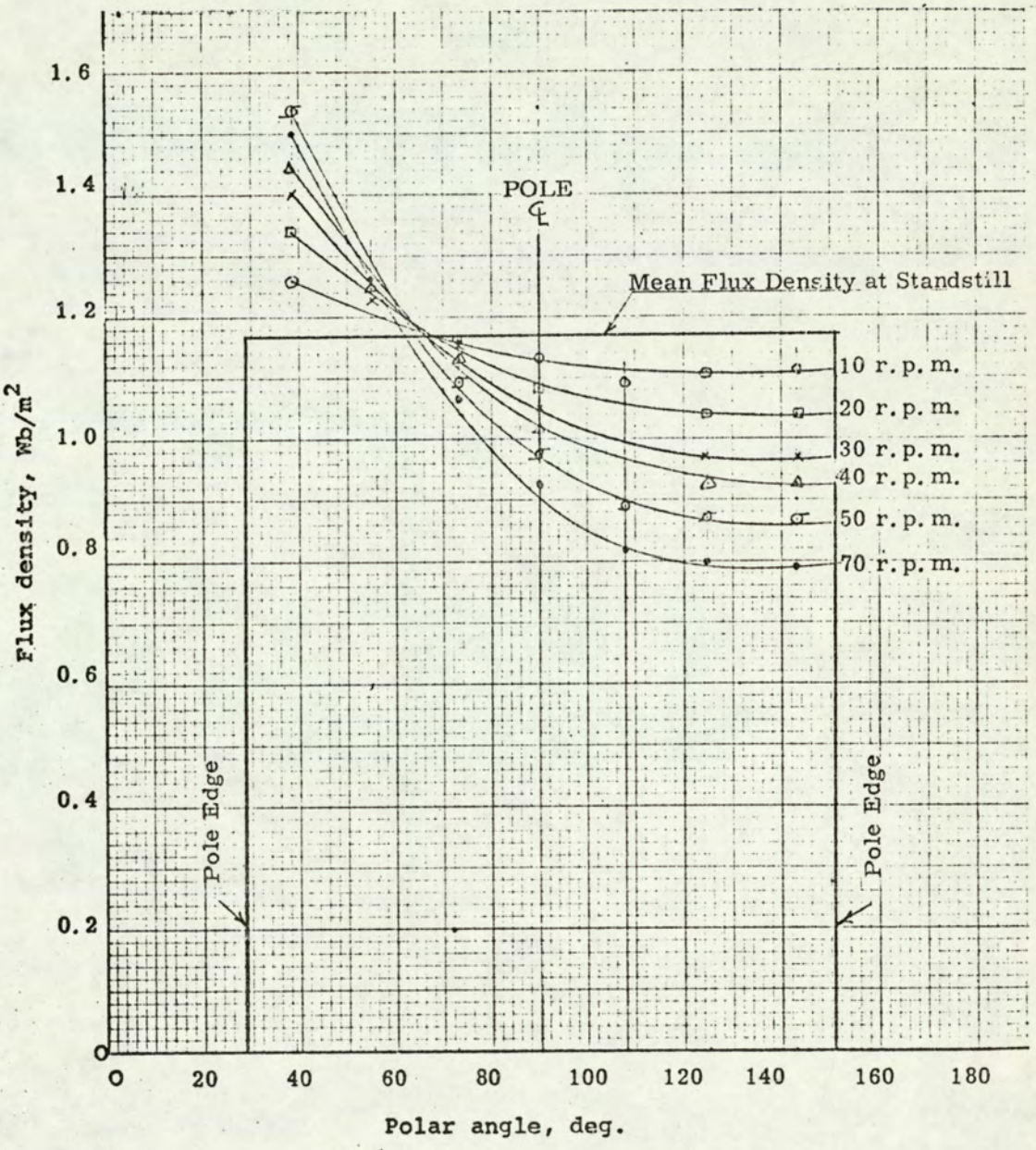

FIGURE 3.6(c)

LOAD FLUX DENSITY DISTRIBUTION ACROSS POLE FACE AT VARIOUS SPEEDS AT CONSTANT EXCITATION.

FIELD CURRENT 0.1A., (130AT/pole)

ENDRING DRUM

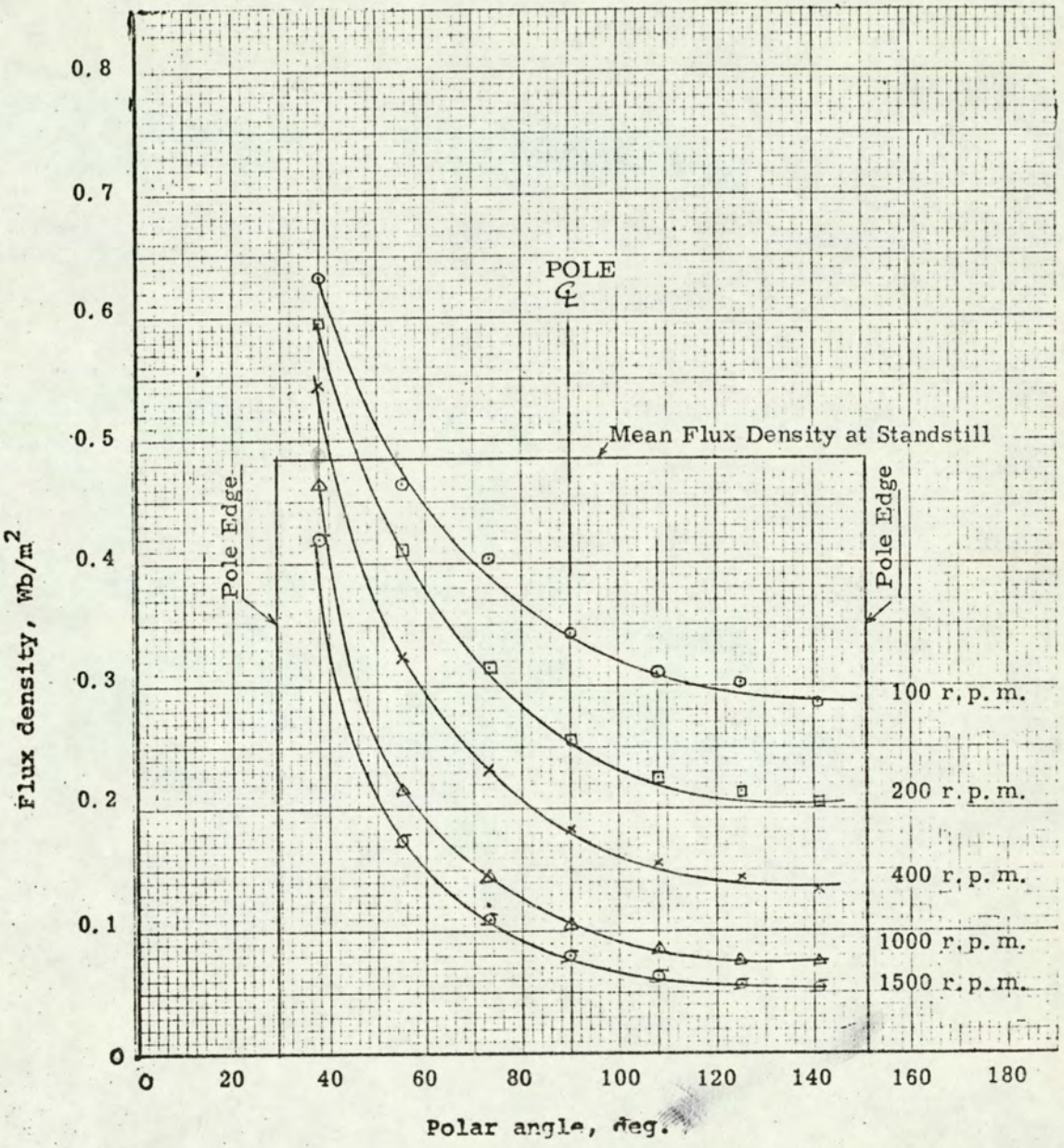

FIGURE 3.6(d)

LOAD FLUX DENSITY DISTRIBUTION ACROSS POLE FACE
AT VARIOUS SPEEDS AT CONSTANT EXCITATION.
FIELD CURRENT 0.2A (260 AT/POLE).
(END RING DRUM).

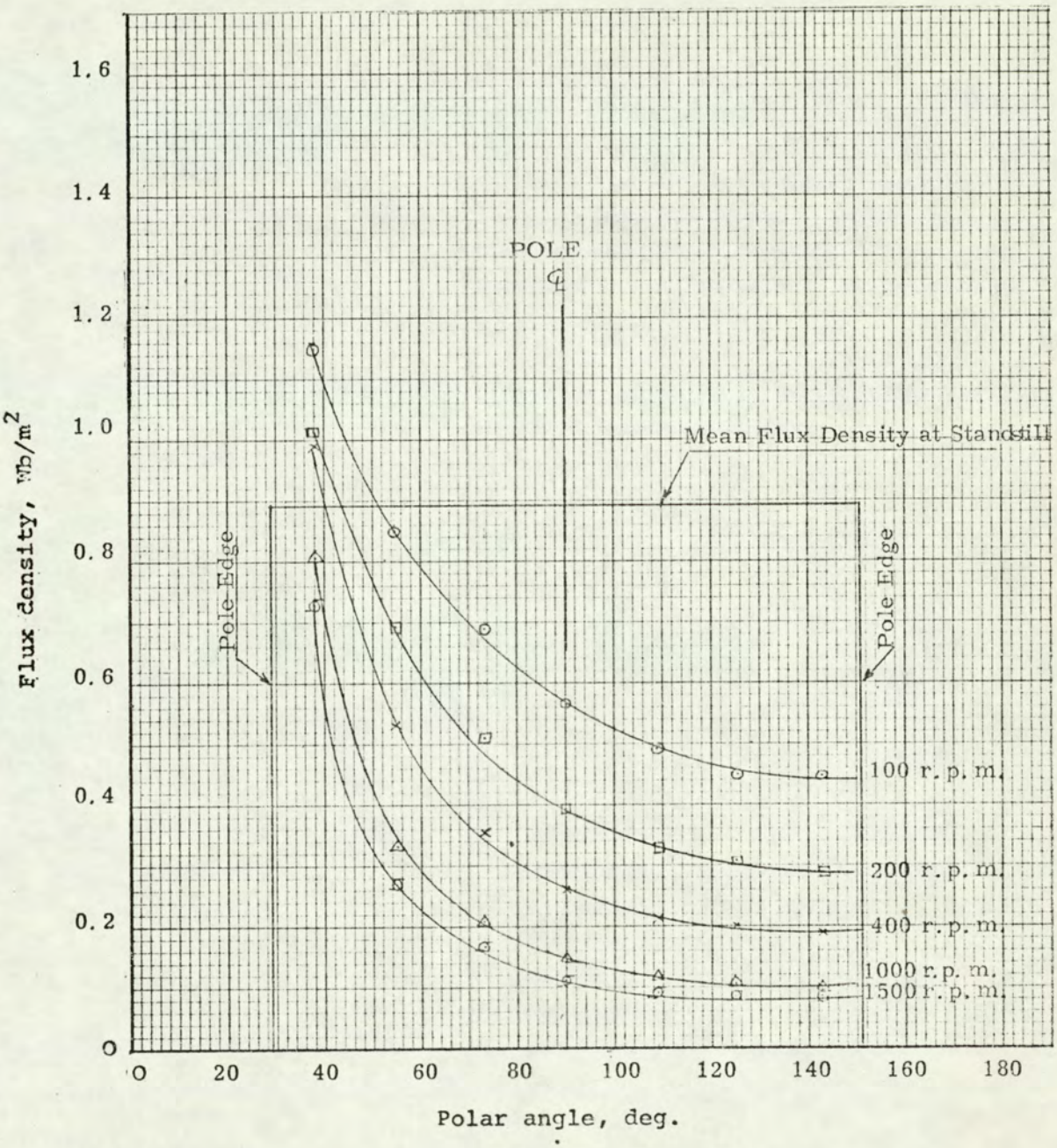

FIGURE 3.6(e)

LOAD FLUX DENSITY DISTRIBUTION ACROSS POLE FACE
AT VARIOUS SPEEDS AT CONSTANT EXCITATION.
FIELD CURRENT 0.3A (390 AT/POLE).
(END RING DRUM).

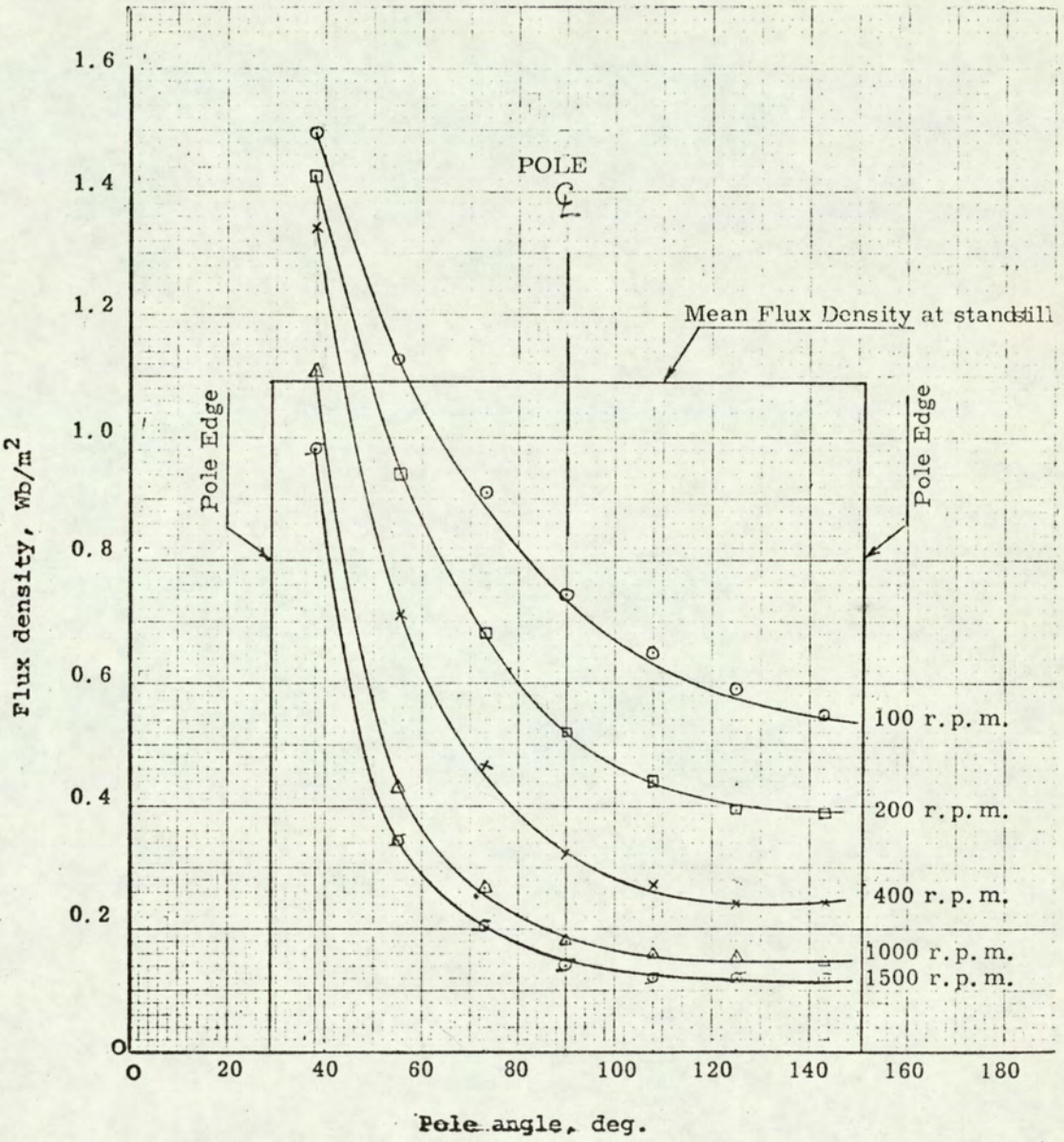

FIGURE 3.6(f)

LOAD FLUX DENSITY DISTRIBUTION ACROSS POLE FACE
AT VARIOUS SPEEDS AT CONSTANT EXCITATION.
FIELD CURRENT 0.4A (520 AT/POLE).
(END RING DRUM).

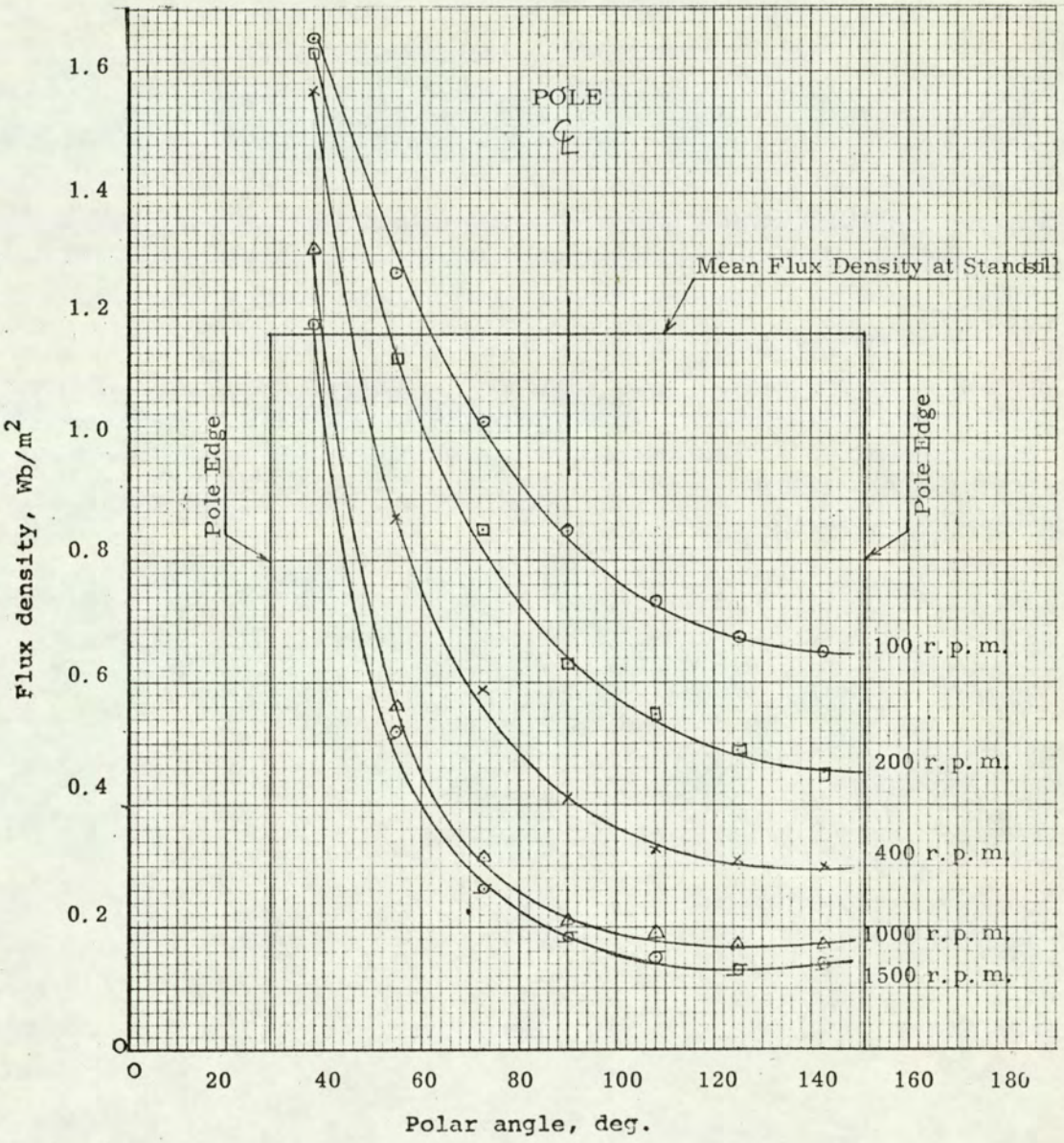

FIGURE 3.6(g)

of slip-frequencies enabled the generalised curves of Reference 12 to be checked not only when the depth of penetration is much less than the radial drum thickness ($\sqrt{2}\alpha \gg 2\pi/\lambda$), but also when it is of comparable magnitude ($\sqrt{2}\alpha \simeq 2\pi/\lambda$).

3.5 Axial pole-face flux distributions on load

Using the search coils described in Section 2.6.1 tests, similar to those described in the previous section, were carried out to establish the axial flux-density distributions. While these tests showed some axial variation in the flux density, it was decided to assume that it was constant as was done in Reference 6. The results of these tests are presented in Appendix A2.

3.6 Analysis of the airgap flux-density distributions

Table 3.3 shows a computer harmonic analysis of the airgap flux-density distributions, together with those presented in Reference 6. It will be seen that:

(a) the endring drum is considerably richer in 3rd harmonics and, to a lesser extent, in 5th harmonics than the solid drum,

(b) the remaining harmonics are not insignificant, which is not surprising since the endring drum produced increased armature reaction,

and (c) the harmonic content increases with slip frequency tending to level off at high slip-frequencies.

Table 3.3

Harmonic analysis of airgap flux-density wave on load

A - Endring drum
B - Solid drum (results from Reference 6)

Field Current, A	Slip Frequency, Hz	Drum	Harmonics, per cent						
			3	5	7	9	11	13	15
0.1	10	A	18	25	20	7	12	11	4
"	"	B	7·5	22					
0.2	"	A	24	26	19	9	12	10	5
"	"	B	15	23					
0.3	"	A	23	26	19	9	12	10	5
"	"	B	16	24					
0.4	"	A	23	25	19	8	12	10	4
"	"	B	14	23					
0.1	20	A	26	27	22	10	14	11	5
"	"	B	16	23					
0.3	"	A	33	30	24	12	15	12	7
"	"	B	19	25					
0.4	"	A	30	28	21	11	14	12	7
"	"	B	19	25					
0.1	40	A	34	31	25	14	16	13	8
"	"	B	18	24					
0.2	"	A	37	34	28	17	18	15	10
"	"	B	26	26					
0.3	"	A	43	34	29	18	19	16	9
"	"	B	26	26					
0.4	"	A	41	33	27	16	17	15	10
"	"	B	23	27					
0.1	100	A	44	37	32	20	20	17	12
"	"	B	30	30					
0.3	"	A	52	43	26	25	24	20	15
"	"	B	35	33					
0.4	"	A	52	43	36	25	23	19	13
"	"	B	33	30					
0.1	150	A	49	40	36	25	25	21	15
"	"	B	33	32					
0.2	"	A	52	40	37	26	25	22	17
"	"	B	38	35					
0.3	"	A	54	45	36	29	28	25	19
"	"	B	36	33					
0.4	"	A	55	45	36	25	23	19	13
"	"	B	35	31					

3.7 Fundamental components

Since the generalised equations of Davies[12] were derived from a theory based on fundamental sinusoidal variations, it is necessary to evaluate the fundamental components of flux per pole, armature reaction, and torque.

3.7.1 Fundamental flux per pole

The variation of the fundamental flux per pole, ϕ_{ac}, with slip-frequency at constant field current is shown in Figure 3.7. From these curves, it is difficult to see the effect of armature reaction at low frequencies and an improved form of presentation is given in Figure 3.8, where ϕ_{ac} on load, at a given field current, is expressed as per unit of the standstill ϕ_{ac} at the same excitation. The increasing effect of armature reaction from 1 Hz to 100 Hz is clearly seen from this figure.

It is of interest to note that the per unit fundamental flux per pole was sensibly constant at a given slip-frequency over the excitations used in the tests.

3.7.2 Fundamental armature reaction

The peak values of armature reaction, F_R, were estimated from Figures 3.6(a) to (g) using the method suggested in Section 6.3 of Reference 6. The results are given in Figure 3.9, and discussed in Section 3.9.2 and Section 4.1.

3.7.3 Harmonic torques

Let the peak surface value of the eddy-current fundamental

(VARIATION OF FUNDAMENTAL AIRGAP FLUX (ϕ_{ac}) WITH FREQUENCY AT CONSTANT FIELD CURRENT (ENDRING DRUM)

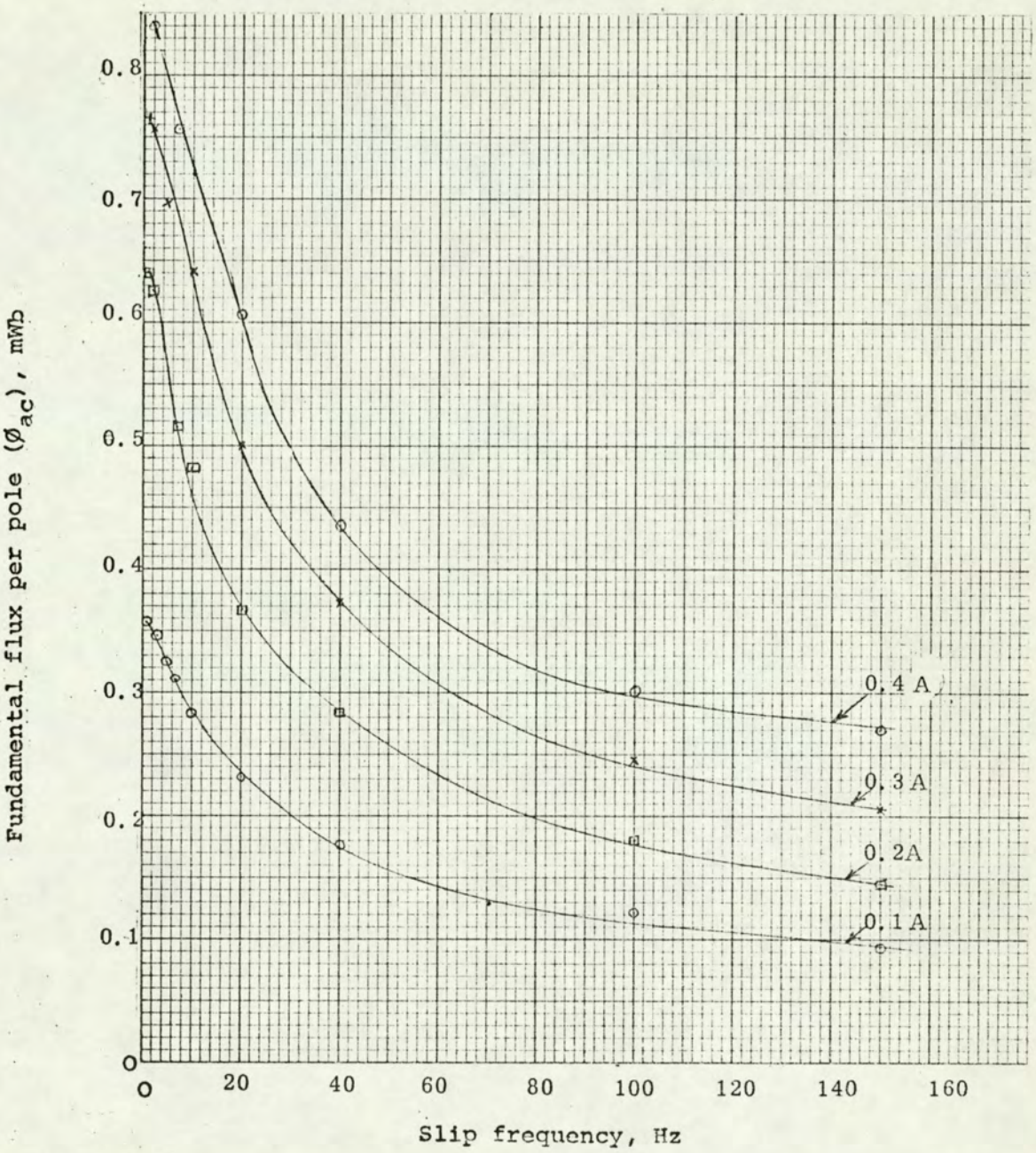

FIGURE 3.7

FUNDAMENTAL LOAD FLUX EXPRESSED AS A PER UNIT OF THE FUNDAMENTAL NO-LOAD FLUX

ENDRING DRUM

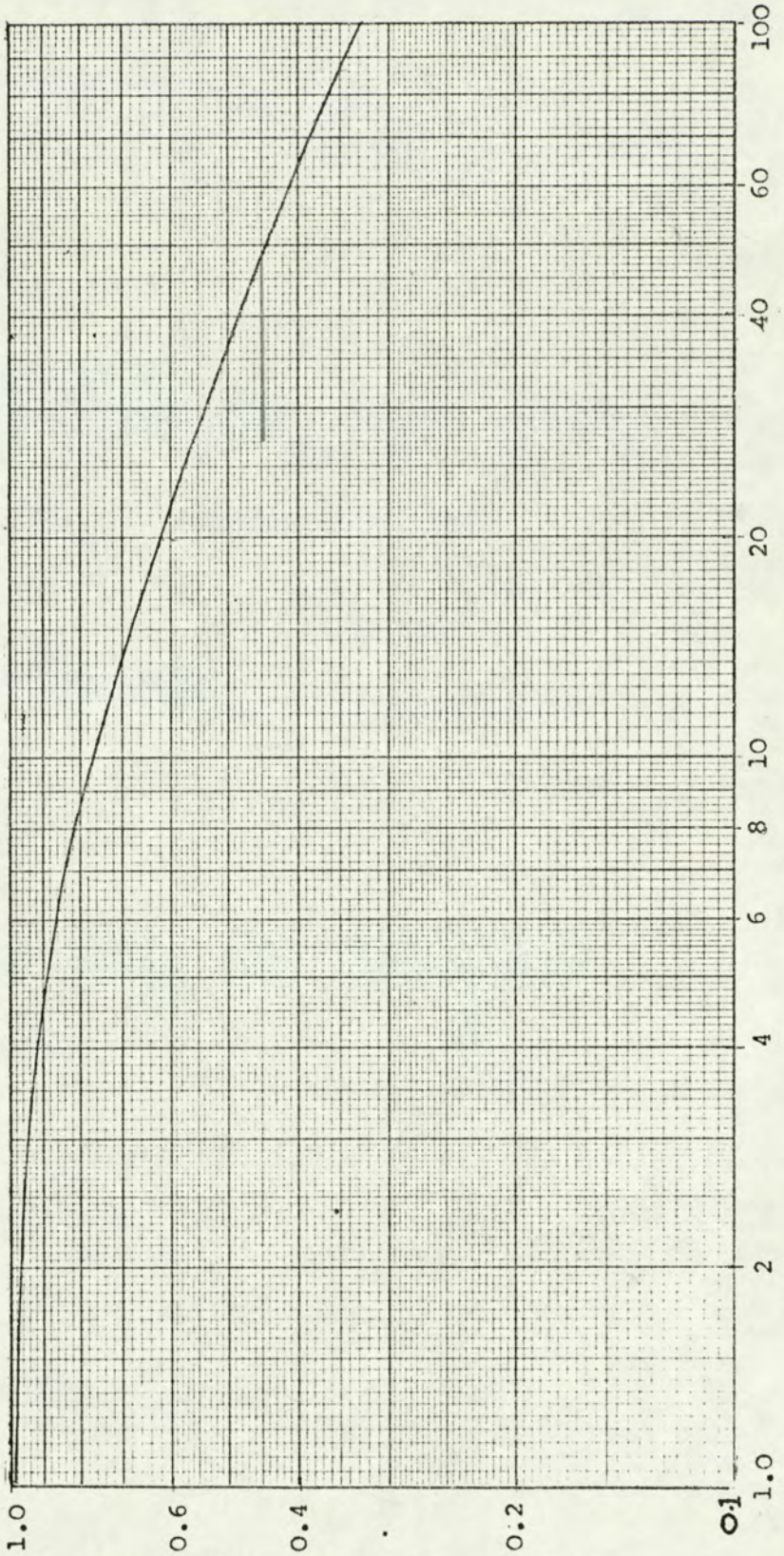

FIGURE 3.8

PEAK ARMATURE REACTION WITH ENDRING DRUM AT VARIOUS SPEEDS AND FIELD CURRENTS

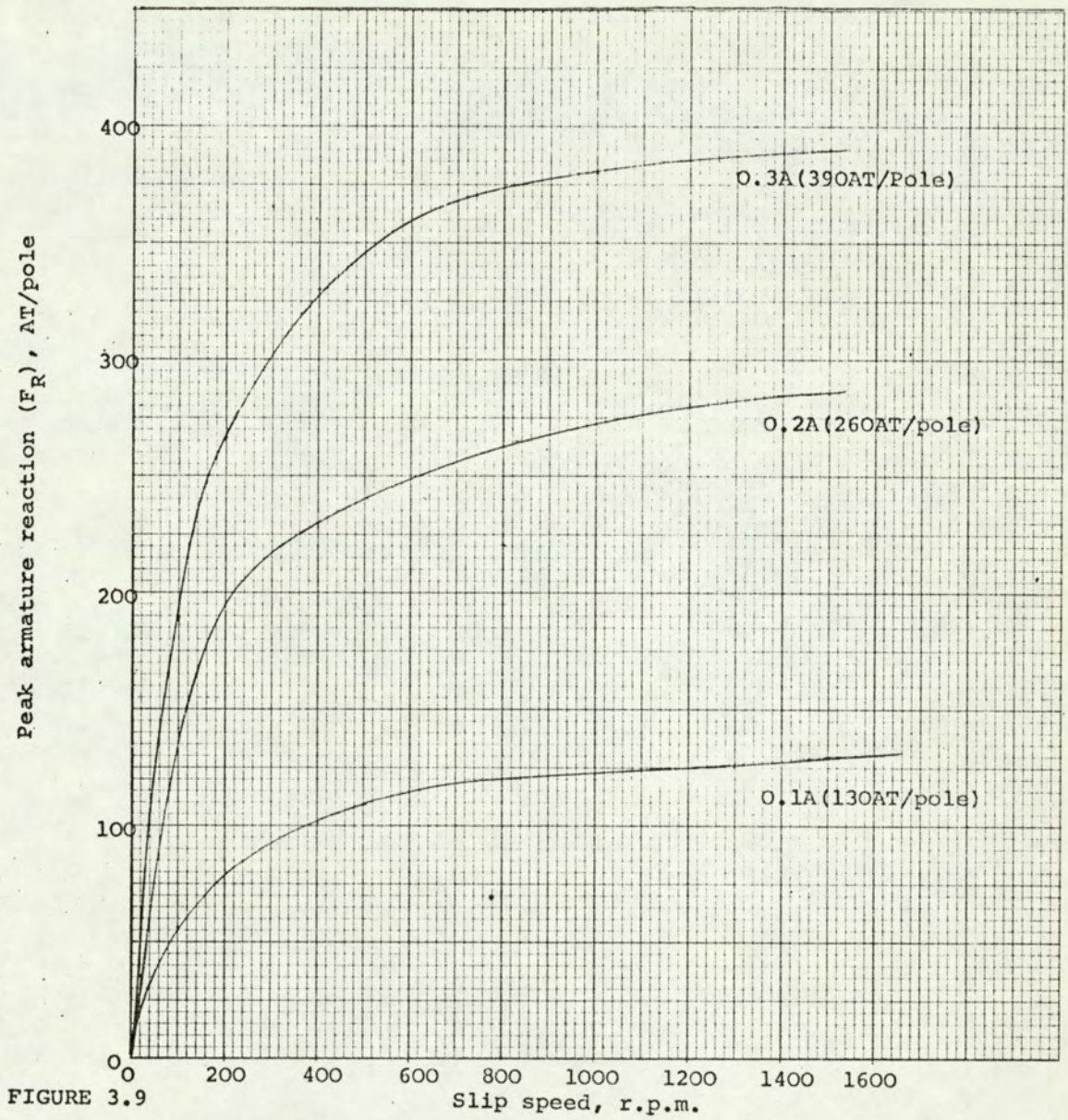

FIGURE 3.9

be J_{m1}. The fundamental drum loss per unit area of the drum surface from equation (1.9) is

$$W_1 = \frac{J_{m1}^2}{4\sigma\alpha_1}$$

where

$$\alpha_1 = \sqrt{\frac{\mu_r \mu_o \sigma \omega_1}{2}} ,$$

$$\omega_1 = 2\pi f_1 ,$$

and f_1 is the fundamental slip frequency.

The fundamental flux per pole from equation (8) of Reference 6 is

$$\phi_{ac_1} = \frac{2 L J_{m1}}{\sigma \omega_1} ,$$

therefore

$$J_{m1} = \frac{\omega_1 \phi_{ac} \sigma}{2 L} , \qquad (3.1)$$

and

$$W_1 = \frac{1}{4\sigma\alpha_1} \left[\frac{\omega_1 \phi_{ac_1} \sigma}{2 L} \right]^2$$

But

$$\phi_{ac_1} = \frac{\pi D L}{2p} \cdot \frac{2}{\pi} \cdot B_1 , \qquad (3.2)$$

where B_1 is the fundamental peak flux density

therefore

$$W_1 \propto \frac{1}{\alpha_1} \omega_1^2 B_1^2 , \qquad (3.3)$$

since σ , D, 2p are constants for a given coupling.

Similarly, for any harmonic h

$$W_h \propto \frac{1}{\alpha_h} (\omega_h \cdot \frac{B_h}{h})^2 , \qquad (3.4)$$

where W_h is the drum loss per unit area of the drum surface due to the h^{th} harmonic,

$$\alpha_h = \sqrt{\frac{\mu_r \mu_o \omega_h \sigma}{2}}$$

$$\omega_h = 2\pi f_h,$$

$$f_h = h f_1,$$

and B_h is the h^{th} harmonic peak flux density.

Therefore

$$\frac{W_h}{W_1} = \frac{(\omega_h \cdot B_h/h)^2}{\alpha_h} \cdot \frac{\alpha_1}{(\omega_1 B_1)^2}$$

$$= \left(\frac{B_h}{B_1}\right)^2 \cdot \frac{\alpha_1}{\alpha_h} \cdot \qquad (3.5)$$

If μ_r is assumed constant then

$$\frac{\alpha_1}{\alpha_h} = \sqrt{\frac{\omega_1}{\omega_h}} = \sqrt{\frac{1}{h}},$$

and

$$\frac{W_h}{W_1} = \left[\frac{B_h}{B_1}\right]^2 \cdot \sqrt{\frac{1}{h}} \cdot \qquad (3.6)$$

Airgap flux density harmonics, being space harmonics, travel at the same speed n as the fundamental. The total torque, T, developed by the coupling is related, therefore, to the harmonic

losses and torques by

$$2\pi nT = \pi DL \lesssim W_h = 2\pi n \lesssim T_h \qquad (3.7)$$

The harmonic torques calculated from equation (3.6) are given in Table 3.4. It will be seen from this table that the total harmonic torque content over the test range varies from around 8% at 10 Hz to around 35% at 150 Hz. Only a limited comparison with the harmonic torque content in the solid drum was possible, and this is shown in Table 3.5. However, it will be noted that the endring drum is considerably richer in 3rd harmonic torque.

3.8 Fundamental torque-speed curves

The fundamental torque at each slip-speed was obtained by subtracting the total harmonic torque, calculated using equation (3.7), from the measured gross torque. Typical fundamental torque-speed curves for the solid and endring drums are shown in Figure 3.10. Apart from the obvious fact that the fundamental torque is less than the gross torque, the curves show that the speed at which the peak fundamental torque occurs is less than the speed at which peak gross torque occurs.

3.9 Generalised curves

Davies[12] derived generalised equations for torque, fundamental flux per pole, armature reaction, and drum loss which are reproduced in Appendix A.1. The correlations of

Table 3.4

Harmonic torques, endring drum

Field current, A	Slip frequency, Hz	Harmonic torque, per cent (T_1 = 100)							
		T_3	T_5	T_7	T_9	T_{11}	T_{13}	T_{15}	Total
0.1	10	1.9	2.8	1.5	0.16	0.43	0.33	0.04	7.06
0.2	"	3.3	3.0	1.37	0.27	0.43	0.28	0.07	8.72
0.3	"	3.1	3.0	1.37	0.27	0.43	0.28	0.07	8.52
0.4	"	3.1	2.8	1.37	0.21	0.43	0.28	0.04	8.23
0.1	20	3.9	3.25	1.83	0.33	0.6	0.33	0.07	10.31
0.3	"	6.3	4.0	2.18	0.48	0.68	0.4	0.12	14.16
0.4	"	5.2	3.5	1.67	0.40	0.6	0.4	0.12	11.89
0.1	40	6.7	4.3	2.3	0.65	0.77	0.47	0.16	15.35
0.2	"	7.9	5.15	3.0	0.97	0.98	0.62	0.26	18.88
0.3	"	10.6	5.15	3.1	1.07	1.1	0.71	0.21	21.94
0.4	"	9.8	4.8	2.75	0.85	0.88	0.47	0.26	19.81
0.1	100	11.0	6.1	3.9	1.33	1.20	0.8	0.37	24.70
0.3	"	15.1	8.3	2.56	2.08	1.75	1.1	0.58	31.47
0.4	"	15.1	8.3	2.56	2.08	1.6	0.93	0.43	31.00
0.1	150	13.8	7.2	4.9	2.08	1.73	1.23	0.58	31.52
0.2	"	15.5	7.2	5.0	2.2	1.73	1.34	0.75	33.72
0.3	"	16.8	9.1	6.0	2.8	2.38	1.73	0.93	39.74
0.4	"	17.4	9.1	4.9	2.08	1.6	1.0	0.43	36.51

Table 3.5

Comparison of harmonic torques, endring and solid drums

A - Endring drum
B - Solid drum (results from Reference 6)

Field Current, A	Slip Frequency, Hz	Harmonic torques, per cent			
		T_3	T_5	$T_3 + T_5$	
0.1	20	3.9	3.25	7.15	A
	"	2.36	4.2	6.56	B
"	40	6.7	4.3	11.0	A
	"	2.66	4.65	7.31	B
"	100	11.0	6.1	17.1	A
	"	7.8	7.8	15.6	B
0.2	10	3.3	3.0	6.3	A
	"	1.8	4.0	5.8	B
"	40	7.9	5.15	13.05	A
	"	5.9	6.0	11.9	B

COMPARISON OF FUNDAMENTAL TORQUE-SPEED CURVES OF SOLID ENDRING DRUM COUPLINGS

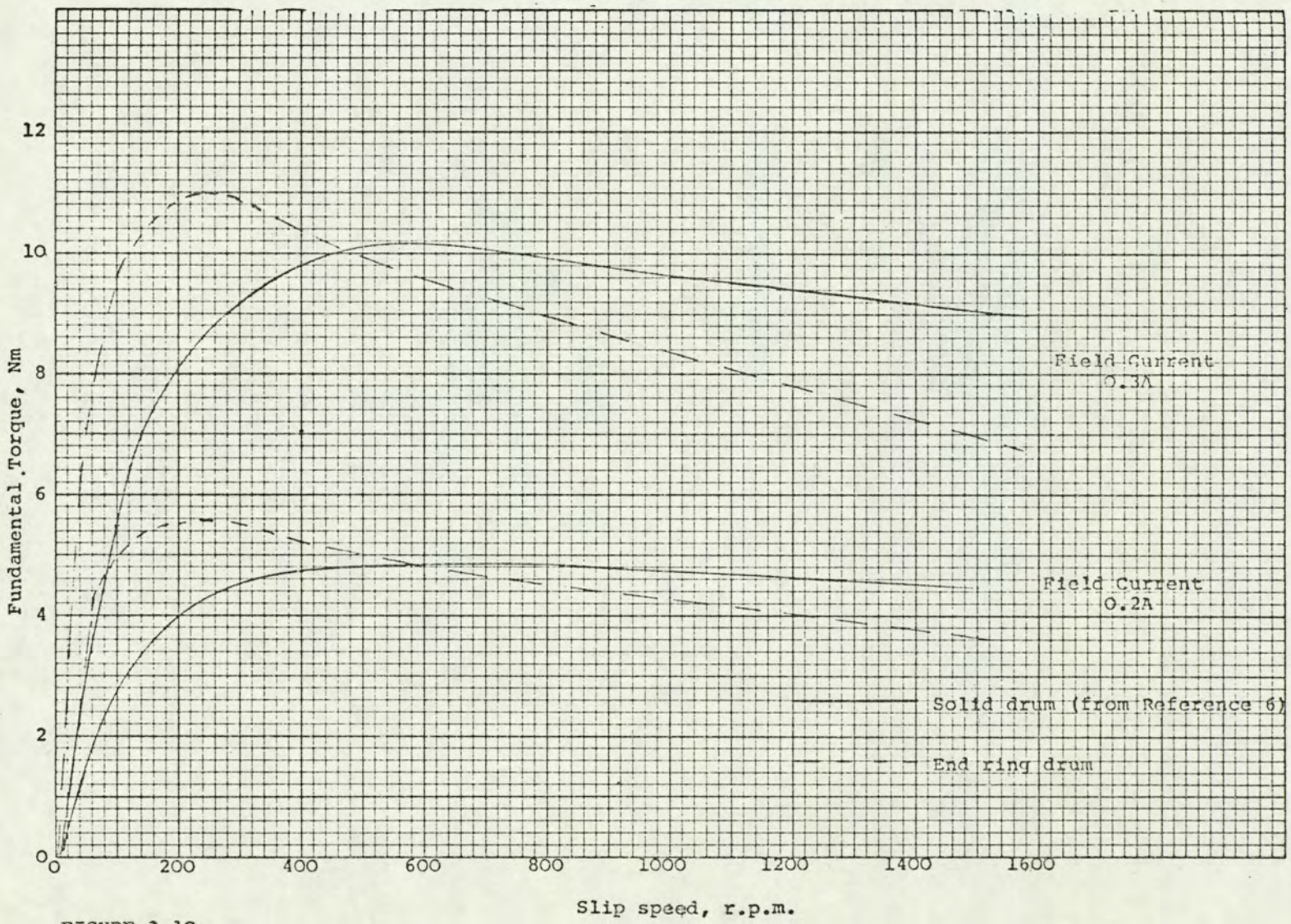

FIGURE 3.10

the results of the preceding sections with the generalised equations, for m = 0.77*, are discussed in the following four sections.

3.9.1 Fundamental flux per pole

The theoretical generalised curve from Figure 5 of Reference 12 is compared with test results from Figures 3.7 and 3.10 in Figure 3.11. Apart from the extreme high-frequency range, nowhere does the deviation from the generalised flux curve exceed 10%. This degree of deviation is adequate for practical design studies.

3.9.2 Armature reaction

The theoretical generalised curve from Figure 5 of Reference 12 is compard with test results from Figure 3.9 and 3.10 in Figure 3.12. For $n/n_m > 0.25$, the maximum deviation from the generalised curve is less than 10%, and in fact at the upper frequency end the correlation is almost exact. Therefore, over this range, the generalised curve would be adequate for design studies.

For $n/n_m < 0.25$, the deviation increases from - 10% to - 45% at $n/n_m = 0.04$. (See Section 3.9.5).

---

* This is the value of 'm' for wrought iron in Davies' relation $(\mu_o \mu)^{1/4} H = K H^m$.

3.9.3 Torque

The theoretical generalised curve from Figure 3 of Reference 12 is compared with test results from Figure 3.10 in Figure 3.13. For $n/n_m > 0.2$, the maximum deviation from the generalised curve is less than 10%. The generalised torque speed curve over this range, which represents an operating range from 5 to 100 Hz, would be suitable for design studies. As with the armature reaction, the deviation increases with decreasing frequency to around - 45% at $n/n_m = 0.07$.

3.9.4 Drum loss

The theoretical drum loss curve from Figure 4 of Reference 12 is compared with test results in Figure 3.14. The deviation is less than 9% for $n/n_m > 0.2$ but increases to - 50% at $n/n_m = 0.08$.

3.9.5 Comments on generalised curves

The largest deviations occur at the low slip-frequency end (below 5 Hz). At low frequencies, the approximation $\sqrt{2}\alpha \gg 2\pi/\lambda$ (Section 3.2, Reference 6), which leads to equation

(1·9)
$$W = \frac{J_m^2}{4\sigma\alpha},$$

is not valid. Without this approximation, equation (9) of Reference 6 is

$$W = \frac{J_m^2}{4\sigma\beta}, \qquad (4.1)$$

GENERALISED FLUX CURVE (m=0.77) - COMPARISON WITH END RING DRUM TEST RESULTS

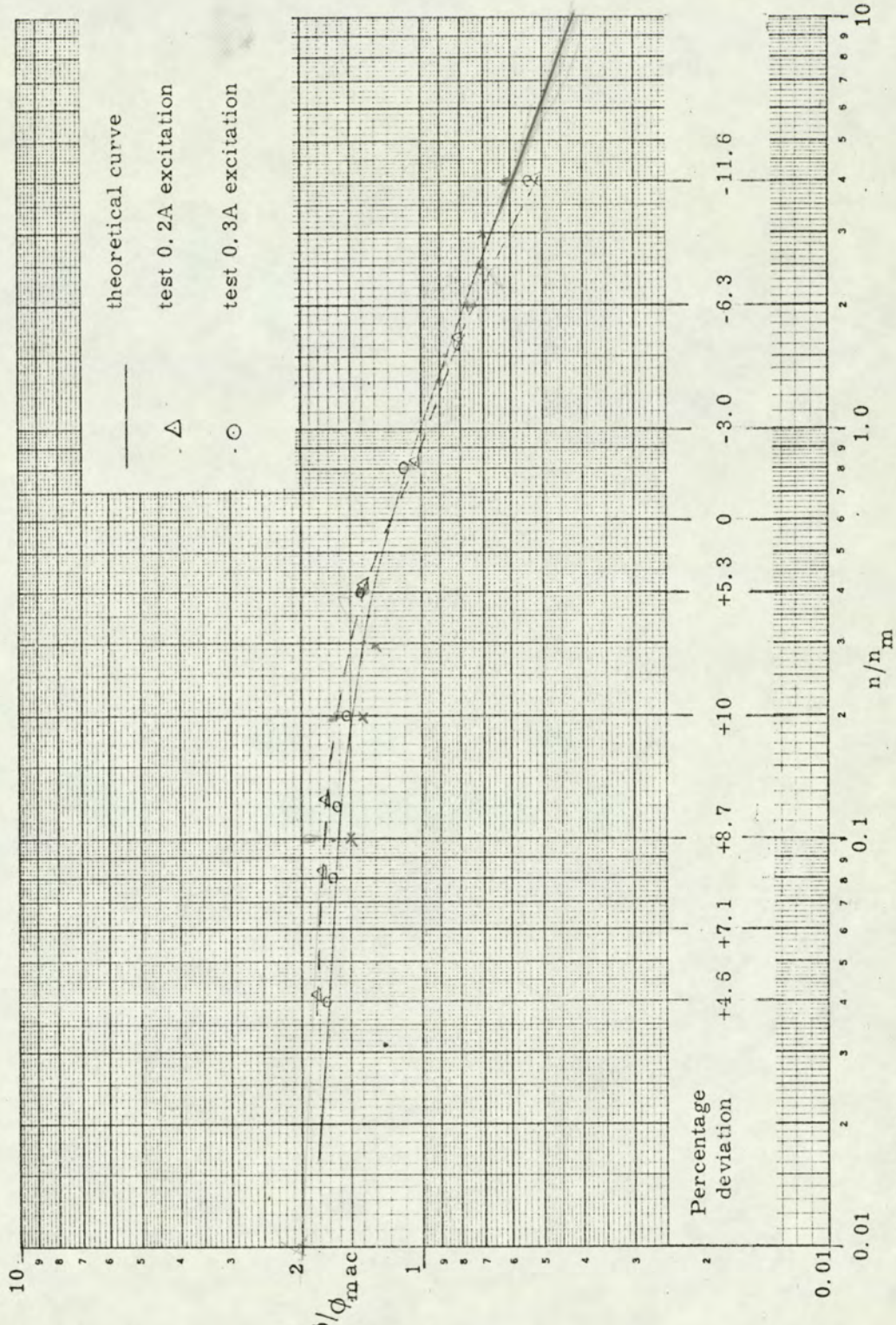

FIGURE 3.11

GENERALISED ARMATURE REACTION CURVE (m=0.77) - COMPARISON WITH ENDRING TEST RESULTS

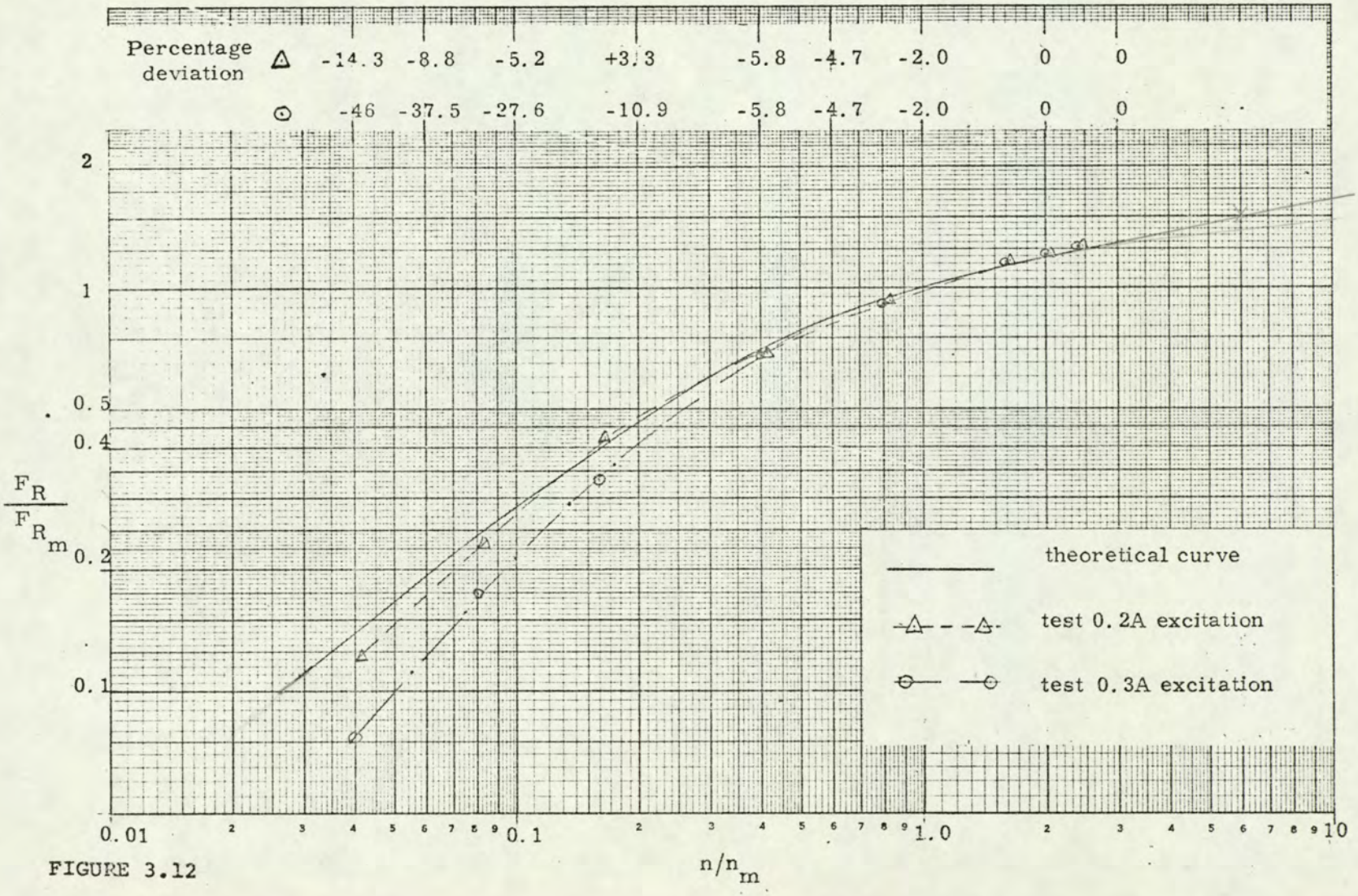

FIGURE 3.12

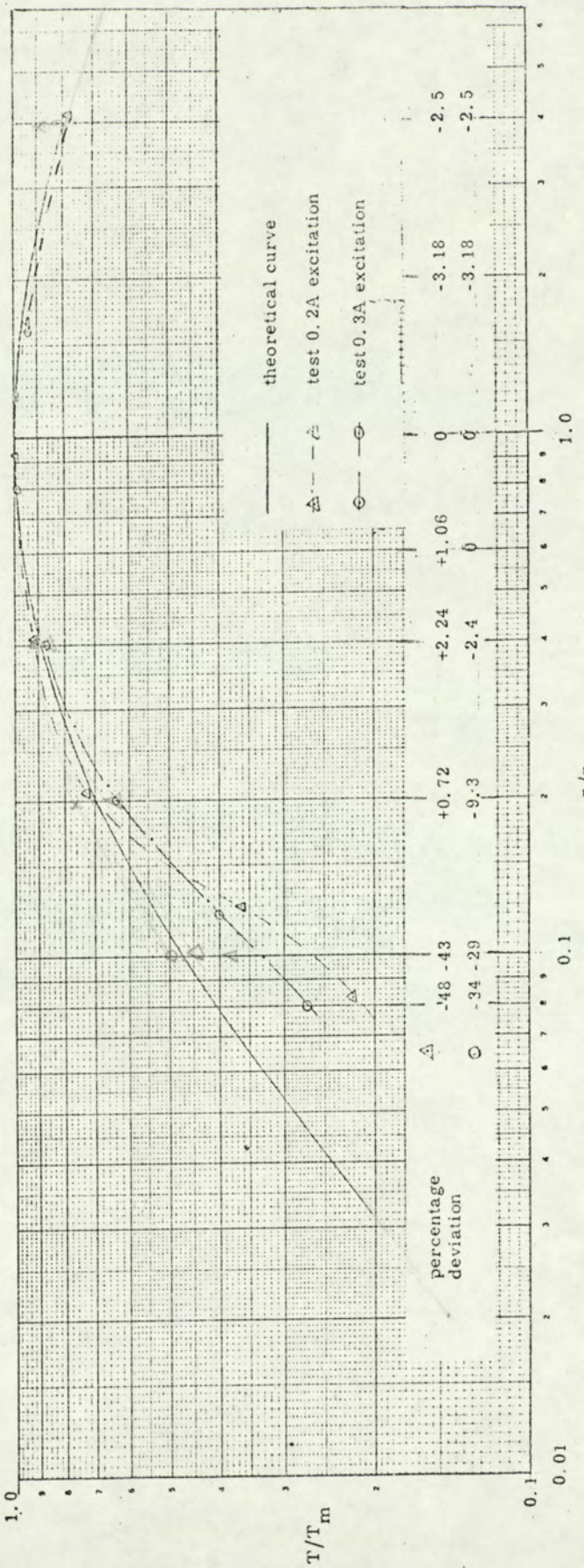
GENERALISED TORQUE-SPEED CURVE (m=0.77) - COMPARISON WITH ENDRING
DRUM TEST RESULTS
theoretical curve
test 0.2A excitation
test 0.3A excitation
percentage deviation
-48 -43 +0.72 +2.24 +1.06 0 -3.18 -2.5
-34 -29 -9.3 -2.4 0 0 -3.18 -2.5
T/T_m
n/n_m
1.0
0.1
0.01
0.1
1.0

FIGURE 3.13

GENERALISED DRUM LOSS CURVE (m=0.77) - COMPARISON WITH ENDRING DRUM TEST RESULTS

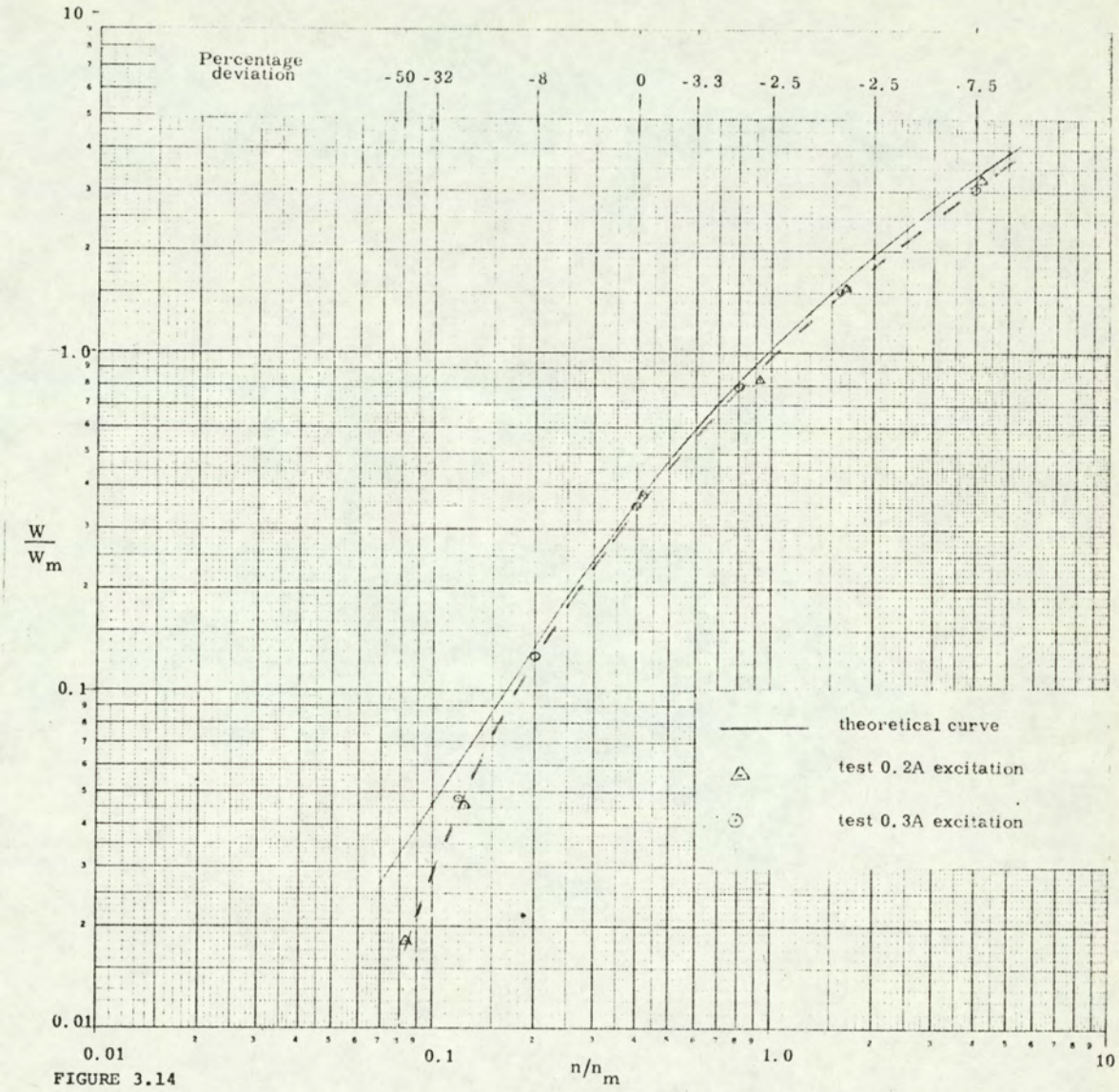

FIGURE 3.14

where $$\beta = \alpha \sqrt{\frac{\delta}{\sqrt{1+\delta^2}-1}} \quad ,$$

and $$\delta = 2\alpha^2 \Big/ (4\pi^2/\lambda^2) \quad .$$

Let $$C = \sqrt{\frac{\delta}{\sqrt{1+\delta^2}-1}} \quad ,$$

then $$\beta = C\alpha$$

Values of δ at low frequencies, in Table 3.6, are obtained from measured values of the depth of penetration ($d = 1/\alpha$) from Table III of Reference 8 assuming that $d \propto 1/\sqrt{\omega}$

Table 3.6

Slip frequency, Hz	10	5	4	3	2	1
depth of penetration, d, mm	5.3	7.49	8.37	9.72	11.83	16.76
δ	12.45	6.21	5.0	3.73	2.5	1.24
C	1.04	1.08	1.1	1.14	1.22	1.45

The low-frequency drum loss can be written

$$W = \frac{J_m^2}{4\sigma C\alpha} \qquad (4.2)$$

The torque is proportional to the drum loss, so to a first approximation low-frequency torque

$$T_\beta = \frac{T_\alpha}{C} \qquad (4.3)$$

where T_α is the torque calculated on the assumption that $\sqrt{2}\alpha \gg 2\pi/\lambda$. The square-dotted curve in Figure 3.15 shows T_β / T_m at the low-frequency end. It will be seen that there is now better correlation with test results.

Adderley's work and subsequent work in the Electrical Machines Centre indicates that the surface flux density in solid iron subjected to normal travelling wave excitations is in the region of $1 Wb/m^2$, which lends support to Davies'[12] suggestion that, over a wide frequency-range, the drum is not working in magnetic saturation. Therefore, it would appear that the substantial deviations at low frequencies, i.e. $n/n_m < 0.1$, cannot be attributed to saturation effects. In fact, it seems possible that better correlation will have to await a theoretical solution which " ..... would include μ as a variable throughout, instead of making the substitution for μ at the end. "[12].

GENERALISED TORQUE-SPEED CURVE MODIFIED AS THE LOW FREQUENCY REGION USING METHOD GIVEN IN SECTION 3.9.5

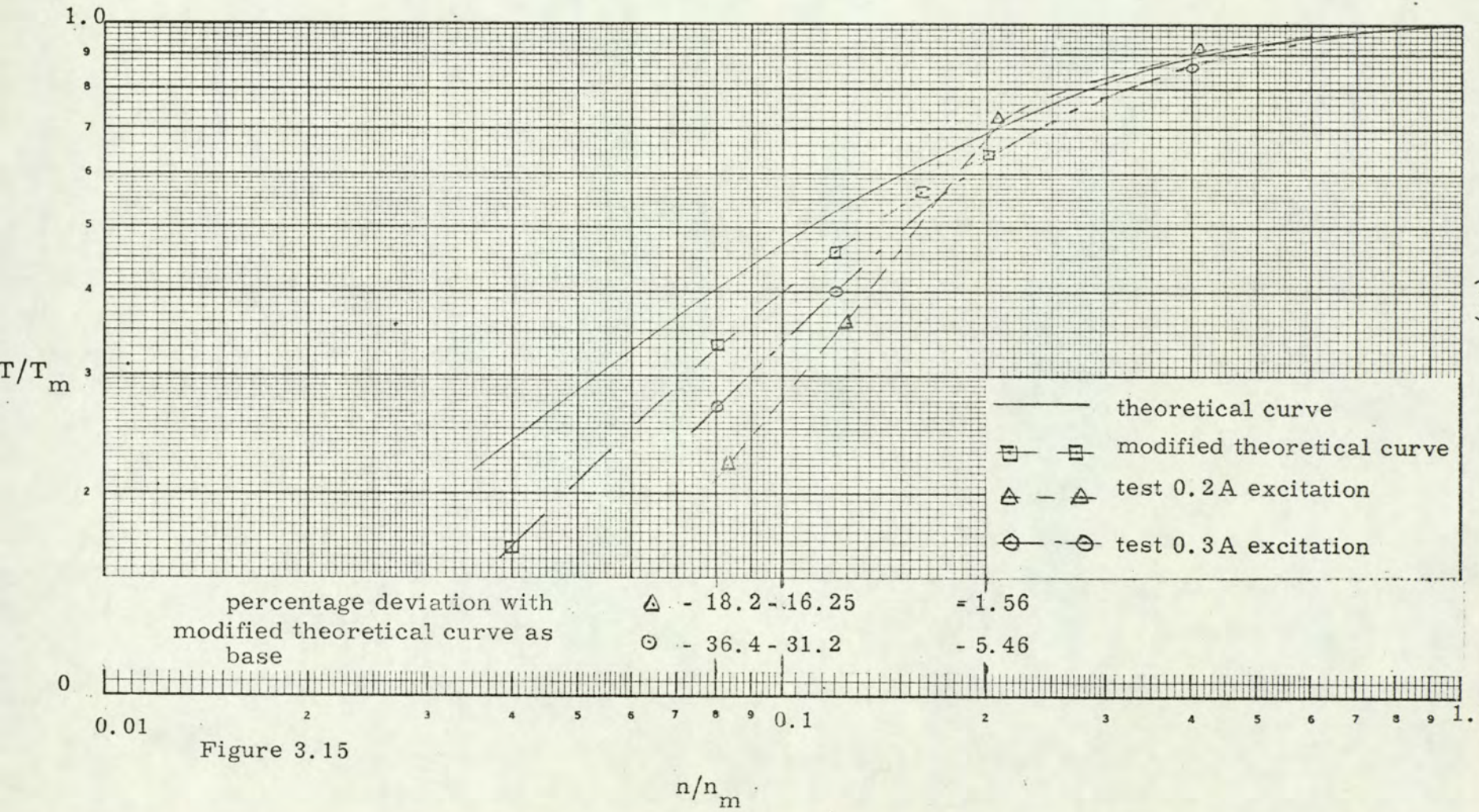

Figure 3.15

The frequency range where the deviation is high (Figures 3.12 to 3.14) is not important from a design point of view. For the normal working range of couplings, $n/n_m > 0.1$, the deviation is less than 10%. The generalised curves therefore provide a sound basis for design studies of couplings, and may find applications in kindred problems with solid iron, for example, negative-sequence losses in rotors of turbo-generators, and pole-face losses in solid-pole synchronous machines[18].

Chapter 4 End effects

4.1 Comparison of endring and solid-drum test results

End effects in solid-drum couplings were discussed briefly in Section 1.5. The end-region currents, which are generated in the active region, distribute themselves " ..... to give minimum resistance loss" (Gibbs[3]). Gibbs also pointed out that the end-region currents flow not only along the inner surface of the drum projecting beyond the pole edges, but also along its radial side faces and outer surface as indicated in Figure 4.1. Tests using

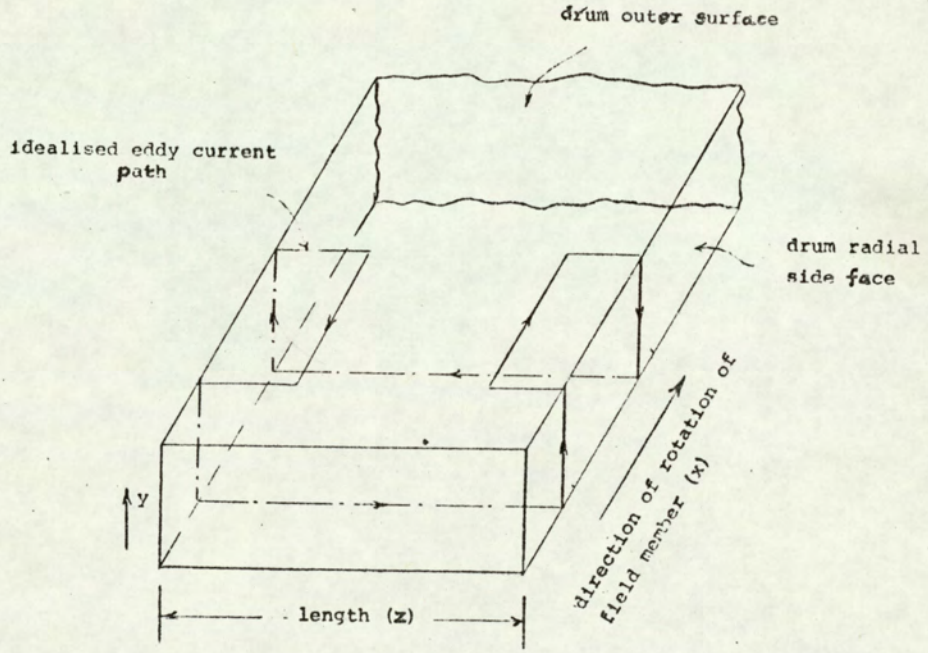

FIGURE 4.1

the E-probe described in Section 2.10 showed the presence of currents in the regions suggested by Gibbs, but a more refined technique would be required to demarcate the active and end region current distribution.

The end-region currents in the solid drum produce two effects not present in a drum without end effects:

a) increased drum loss without increased torque,

and b) increased 'drum impedance'.

The additional drum loss in the end-regions can be considered as equivalent to an increase in the drum resistivity (Reference 3) with a consequent reduction in the torque. The increase in drum impedance due to the end-regions reduces the magnitude of the eddy currents for a given excitation and slip-speed, that is the eddy-current armature reaction is reduced (see below).

Test results of F_R, ϕ_{ac}, and the phase angle ϕ for the solid and endring drums are compared in Tables 4.1(A) and (B), 4.2 and 4.3(A) and (B) respectively. ϕ is the angle between the zero of the armature reaction wave and the maximum of the fundamental resultant flux density in the airgap (see Figure 4.2); it is analogous to the 'power factor angle' in synchronous machines (see vector diagram in Section 10.2 of Reference 6). F_R and ϕ were determined from the test results as explained in Sections 6.3 and 6.4 of Reference 6.

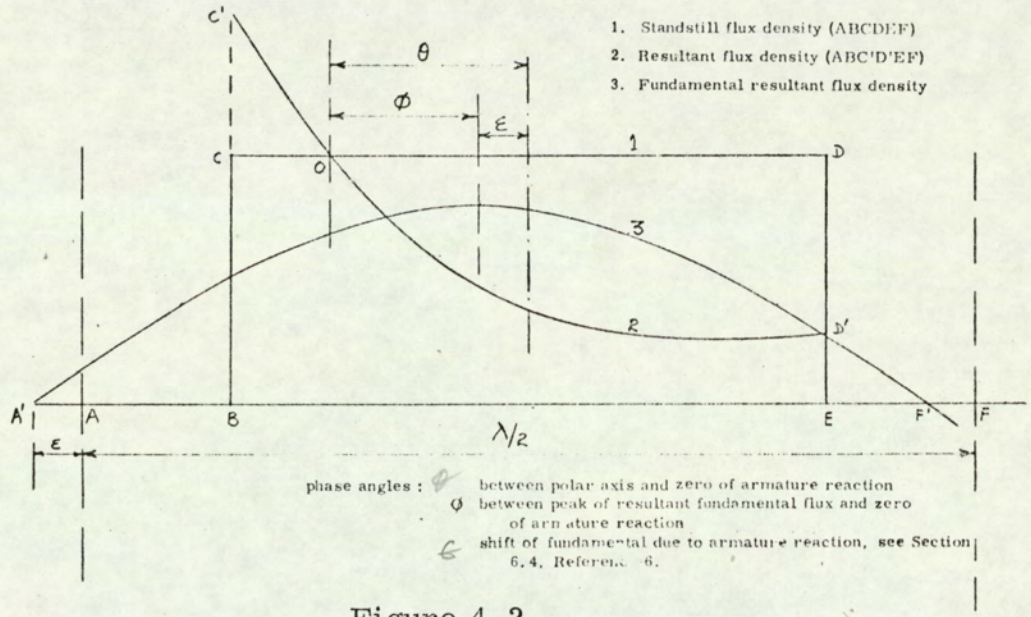

Figure 4.2

Table 4.1 shows clearly the increased armature reaction with the endring drum. This increase was particularly marked up to 40 Hz, but thereafter there appears to be a tendency to level off (see also Figure 3.7). The ratio F_R(endring)/F_R(solid)

is not constant, being over 1.5 up to 20 Hz and much less in the 40 - 50 Hz range.

The variation in the airgap flux with excitation and slip-frequency for the two drums is shown in Table 4.2. It will be seen from this table that, as discussed in Section 3.7.1, for a given excitation ϕ_{ac} decreases with increasing slip-frequency. For the endring drum the ratio $(\phi_{ac})_{150Hz}/(\phi_{ac})_{10Hz}$ is about 0.3; for the solid drum the corresponding ratio is about 0.5. It will also be seen from Table 4.2 that for each excitation the ratio ϕ_{ac}(endring)/ϕ_{ac}(solid) follows practically the same pattern over the slip-frequency range, varying from about 90% at 10 Hz to around 60% at 150 Hz.

The larger 'drum impedance' of the solid drum is clearly demonstrated by the results in Table 4.3(A) where ϕ for the solid drum is appreciably greater than for the endring drum. The measured values of ϕ are considerably less than the theoretical value of 45^{o} obtained when the permeability is assumed constant. Some support as to the correctness of the order of magnitude of the measured values of ϕ is to be found in the work of McConnell[15] and Sharov[4]. McConnell et al. showed that, for a rectangular magnetisation curve, that is, iron always fully saturated, ϕ approached 26^{o}. Sharov's measured values of ϕ for a solid rotor induction motor were approximately 45^{o} for 'weak fields' and 31^{o} for 'strong fields'.

Table 4.1(A) Comparison of F_R between the endring and solid drum couplings

Field current, A	Slip frequency, Hz	F_R, AT/pole		Ratio (A)/(B)
		endring drum (A)	solid drum* (B)	
0.1	10	56	36	1.55
	20	81	54	1.50
	40	101	80	1.27
	100	122	99	1.24
	150	130	103	1.26
0.2	10	140	90	1.56
	20	200	124	1.61
	40	238	161	1.28
	100	275	215	1.27
	150	285	225	1.26
0.3	10	187	124	1.51
	20	266	176	1.51
	40	330	245	1.34
	100	380	307	1.24
	150	390	328	1.19

* from Reference 6

Table 4.1(B)

Field current, A	Slip frequency, Hz	F_R, AT/pole (endring drum)
0.2	1	23
	2	27
	4	81
	7	107
0.3	1	37
	2	70
	4	115
	7	168
0.4	1	36
	2	67
	4	103
	7	190

Table 4.2 Comparison of ϕ_{ac} between the endring and solid drum couplings

Field current A	Slip frequency Hz	ϕæ, mWb endring drum (A)	solid drum* (B)	ratio, (A)/(B)
0.1	10	0.282	0.309	0.915
	20	0.232	0.288	0.805
	40	0.177	0.254	0.70
	100	0.121	0.18	0.671
	150	0.094	0.15	0.625
0.2	10	0.481	0.535	0.90
	20	0.368	0.49	0.75
	40	0.284	0.41	0.692
	100	0.180	0.28	0.642
	150	0.148	0.245	0.605
0.3	10	0.64	0.72	0.89
	20	0.50	0.65	0.77
	40	0.372	0.53	0.70
	100	0.246	0.385	0.64
	150	0.206	0.33	0.625
0.4	10	0.72	0.80	0.90
	20	0.605	0.73	0.83
	40	0.435	0.59	0.736
	100	0.30	0.45	0.667
	150	0.27	0.40	0.675

* from Reference 6.

Table 4.3(A) Phase angle of ϕ for endring and solid drum couplings

Field current, A	Slip frequency, Hz	Phase angle ϕ, deg. †	
		endring drum	solid drum *
0.1	10	29.3	34.9
	20	29.5	38.2
	40	30.1	43.4
	100	30.0	40.3
	150	29.1	38.7
0.2	10	25	35.4
	20	29.9	38.9
	40	29.0	39.2
	100	28.0	38.4
	150	27.3	37.5
0.3	10	14.3	22.9
	20	21.0	30.6
	40	23.3	33.2
	100	23.7	36.4
	150	24.7	37.6
0.4	10	16	22.3
	20	20.3	27.4
	40	24.8	34.5
	100	21.2	37.5
	150	24.8	37.9

Table 4.3(B)

Field current, A	Slip frequency, Hz	Phase angle ϕ, deg. (endring drum)
0.2	1	18
	2	18.4
	3	18.8
	4	21
	7	26.5
0.4	1	16.3
	2	16.6
	3	17.0
	4	18.0
	7	19.4

† The phase angles are corrected for phase shift on load as described in Section 6.4 of Reference 6. See also Figure 4.2

* From Reference 6.

From simple circuit concepts, one might expect that, for a given excitation, ϕ would increase with slip-frequency because of increasing drum reactance. However, the corresponding increase in drum resistance due to the increased skin effect attenuates the increase which would be produced in ϕ by the increase in 'drum reactance' alone.

Table 4.3(B) shows ϕ for slip frequencies less than 10 Hz. It will be noted that, even over this frequency range, ϕ is not insignificant, which means that as far as solid iron is concerned a frequency of even 1 Hz is not a low frequency.

4.2 End-region tests

The search coils described in Sections 2.7.1 and 2.7.2 were used to investigate the axial and radial distributions of the flux density in the end regions of the solid-drum coupling. The excitation and speed ranges were 0.1 to 0.4 A and 100 - 1000 r.p.m.

4.2.1 Axial distributions

Figure 4.3 shows typical oscillograms obtained with the axial distribution search coils shown in Figure 2.8. That there is little distortion in the waveform was confirmed by the oscillogram of the integrated signals which approximated closely to sinusoidal. Figure 4.4 shows a typical log-linear plot of the maximum average flux densities through the twelve search coils at 10 Hz and 100 Hz for a field excitation of 0.3 A.

Waveforms of induced voltage in the axial search coils in the end-region (see Figure 2.8 for search coils)

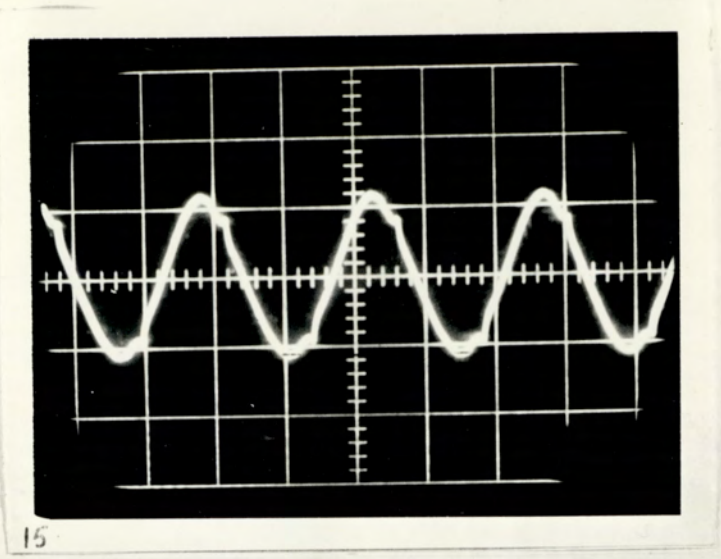

Search coil No. 6, Frequency 100 Hz, excitation 0.1 A
5 mV/cm, 2 ms/cm

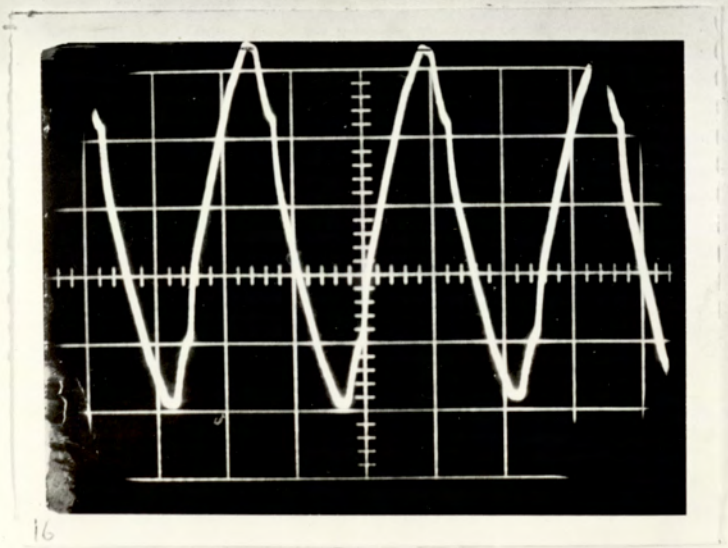

Search coil No. 12, Frequency 100 Hz, excitation 0.1 A
1 mV/cm, 2 ms/cm

Figure 4.3

END-REGION AXIAL FLUX DENSITY DISTRIBUTION (SOLID DRUM)
FIELD CURRENT 0.3A
(See Figure 2.8 for Search Coils)

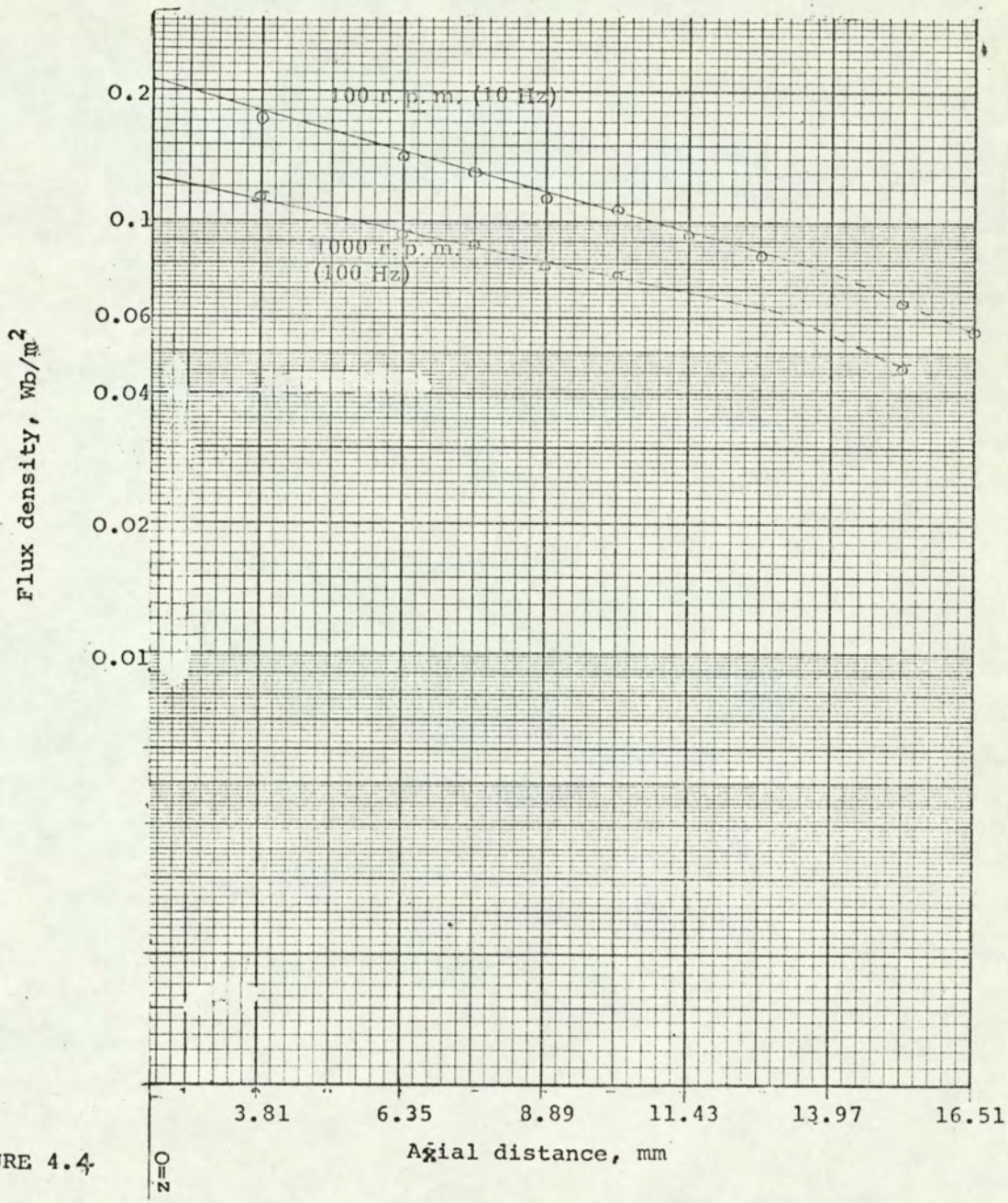

FIGURE 4.4

Similarly-shaped graphs were obtained for the range of excitations 0.1 to 0.4A. The linearity of the graphs shows that the axial decrement is exponential.

The flux in the end-region is due primarily to the end region currents (see Section 3.2). The eddy currents at 100 Hz are greater than at 10 Hz for the same excitation, but the results show that the flux densities are greater at 10 Hz than at 100 Hz. The cause of this reduction in the flux density may be explained as follows:

To fulfil the continuity condition $\nabla . \bar{J} = 0$, the eddy currents generated in the active region must flow in closed circuits, which they do by utilising the end-regions. The whole drum-current configuration moves in synchronism with the field member, and relative to the drum. The end-region currents are therefore self-inductive. The associated skin effect in the end-regions, which becomes more pronounced with increasing slip-frequency, results in a reduction in end-region flux densities at high slip-frequencies compared with those at low frequencies.

4.2.2 Phase angle

The phase angle between the fluxes through pairs of search coils was measured by displaying the integrated induced voltage signals from the search coils on an oscilloscope. These oscillograms showed negligible phase-shift between the fluxes through any pair of search coils. A

End Region Axial Field

Oscillograms showing that there is practically no phase angle between the flux waves linking the axial search coils (Figure 2.8) - Induced voltage waves integrated.

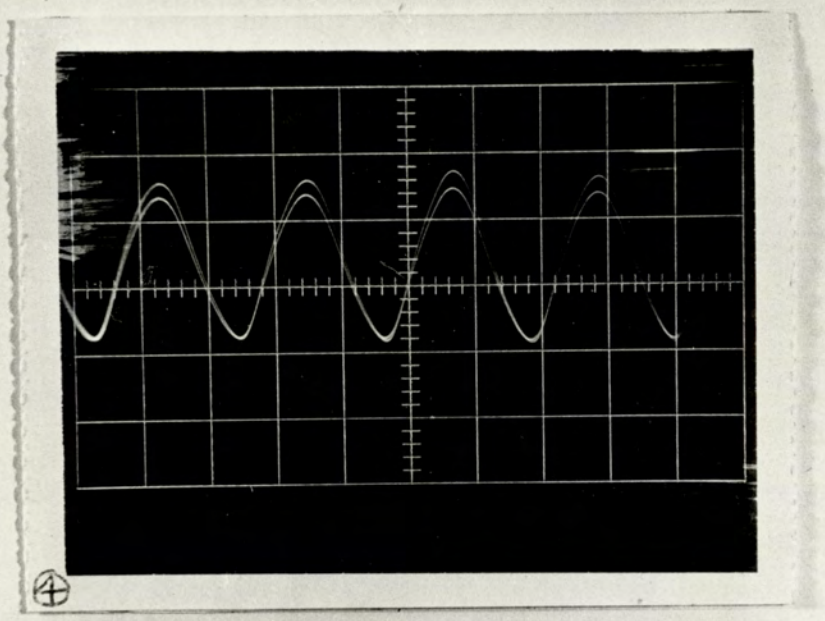

Flux waves in axial coils 2 and 4, Frequency 40 Hz, excitation 0.2A. 10 msec/cm, 0.2 V/cm

Figure 4.5

typical oscillogram is shown in Figure 4.5. Apart from the obvious fact that the end-region field rotates synchronously with the field member the results give general support to Gibbs'[3] model of the end region field distribution.

4.2.3 Radial distributions

Figures 4.6(A) and (B) show oscillograms with the radial distribution search coils shown in Figures 2.9 and 2.10. It will be seen that the e.m.f. waveform for the search coil nearest the drum surface, Figure 4.6(A), has a larger harmonic content than that for the coil in the middle of the drum depth. The reduction in the harmonic content in the latter is due to the rapid attenuation of the harmonics within the drum depth. Typical log-linear plots of the maximum average flux density through the search coils at 10, 40 and 100 Hz are shown in Figure 4.7. The decrements are very similar to those in the active region (see Figures 34 to 37, Reference 6). The flux density at 10 Hz is greater than at higher frequencies for the reasons discussed in 4.2.1.

4.3 Effects of drum overhang

A test was carried out to investigate whether different lengths of drum overhang affected the coupling's performance. Torque-speed curves were taken at a given value of field current with the field member in each of three different axial positions within the drum and the results are shown in Figure 4.8. It will be seen that even when the pole-face edge is in

Waveforms of induced voltage in the radial search coils in the end region (See Figures 2.9 and 2.10 for search coils)

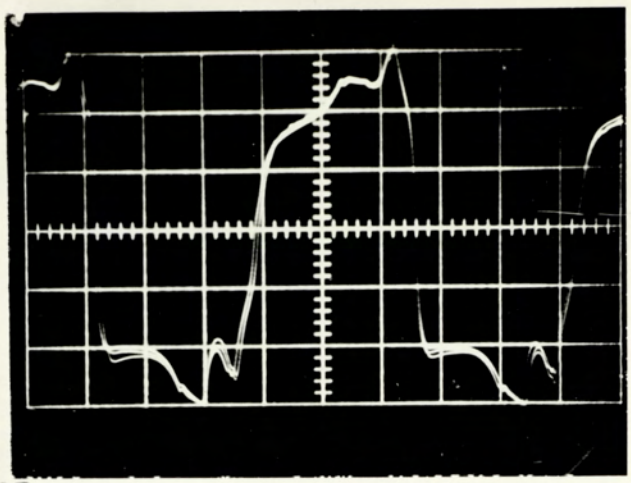

Search coils formed by wires 2 and 3, Figure 2.10. Frequency 40 Hz, excitation 0.3 A.

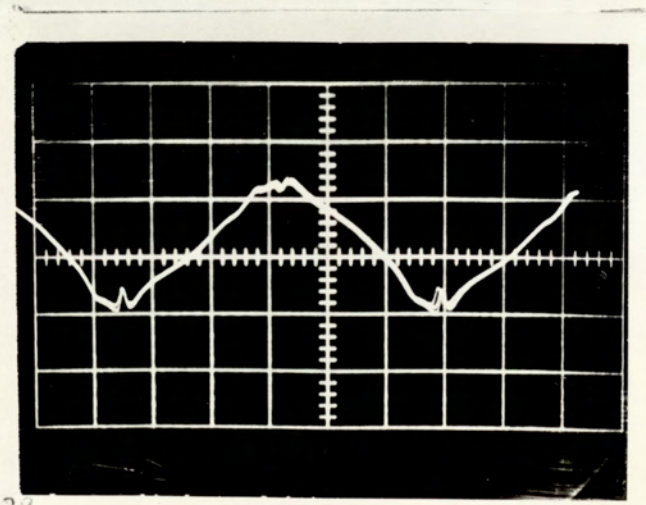

Figure 4.6

Search coils formed by wires 6 and 7, Figure 2.10. Frequency 40 Hz, excitation 0.3 A.

END-REGION FLUX DENSITY DISTRIBUTION (SOLID DRUM)
FIELD CURRENT 0.3A

(See Figures 2.9 and 2.10 for search coils)

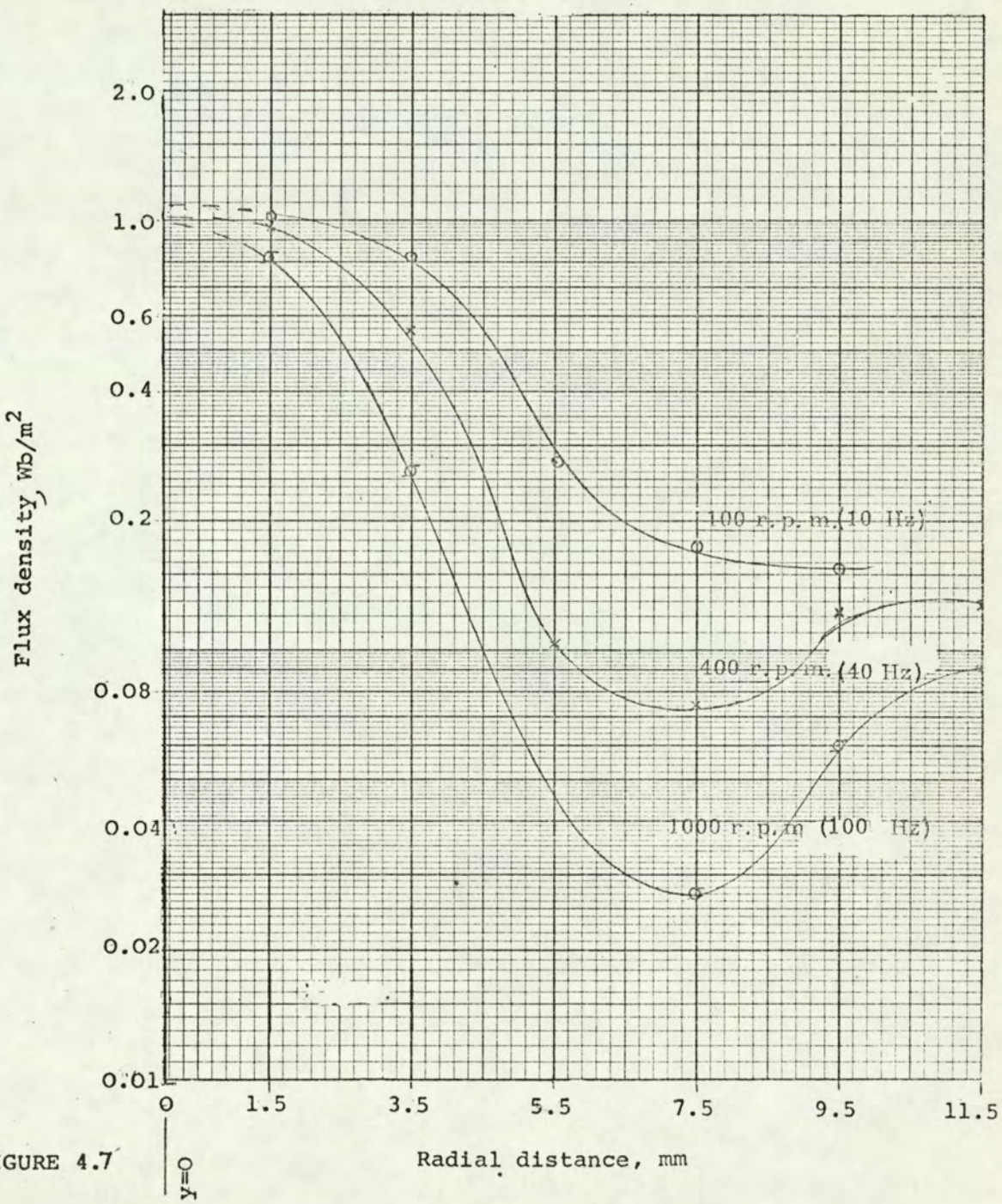

FIGURE 4.7

TORQUE-SPEED CURVES WITH ROTOR POLES IN THREE DIFFERENT AXIAL POSITIONS (SOLID DRUM)

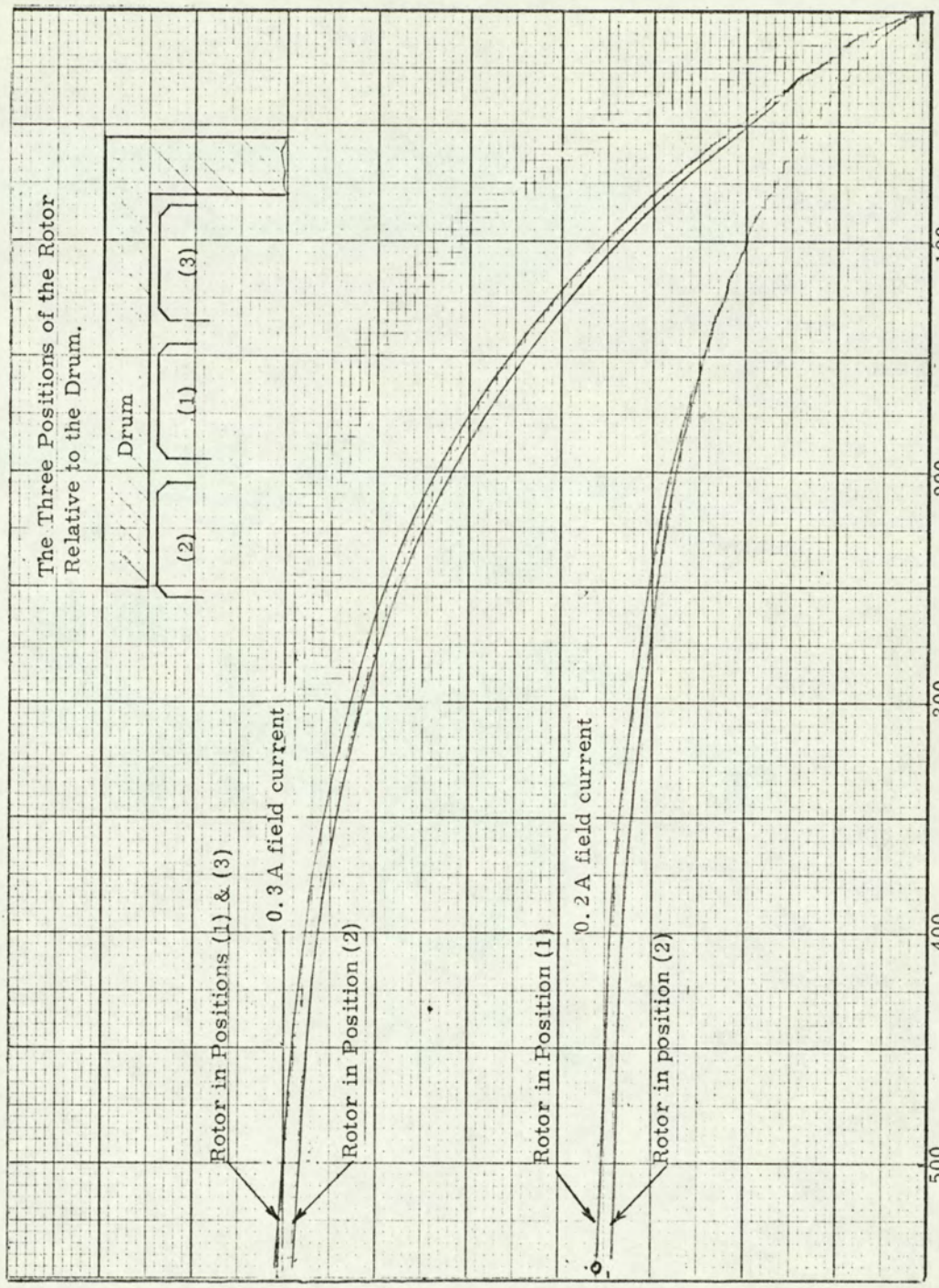

FIGURE 4.8

circumferential alignment with the drum radial face (position 2 in Figure 4.8), the torque-speed curve is almost identical to that with the field member in position 1, which has nearly identical drum overhangs on either side of the field member. It is fairly obvious from the configuration of position 2 that, at the open end of the drum, the return paths of the currents from the active region are forced to flow along the radial side faces of the drum, and possibly, to a limited extent, over the drum outer surface. One might reasonably expect that the greater constraint on the end-region currents at the open end of the drum in position 2 would produce increased end-region losses with a consequent decrease in torque. A small but measurable reduction in torque in position 2 compared with the other two positions can be clearly seen in Figure 4.8 which is consistent with the foregoing argument.

4.4 End region losses

It has been pointed out in Section 4.1 that the losses in the end-region result in 'lost torque'. Therefore, it is important for the designer to be able to estimate this as accurately as possible. Unfortunately, without simplifying assumptions, the end region is analytically intractable for basically the same reasons as the active region. Only Gibbs[3] appears to have published an analytical treatment of the end-region in eddy-current couplings.

4.4.1 Gibbs' analysis

Gibbs[3] assumed the current in the end region to be resistance-limited and to have a two-dimensional distribution as shown in Figure 4.9, (but see Section 4.1).

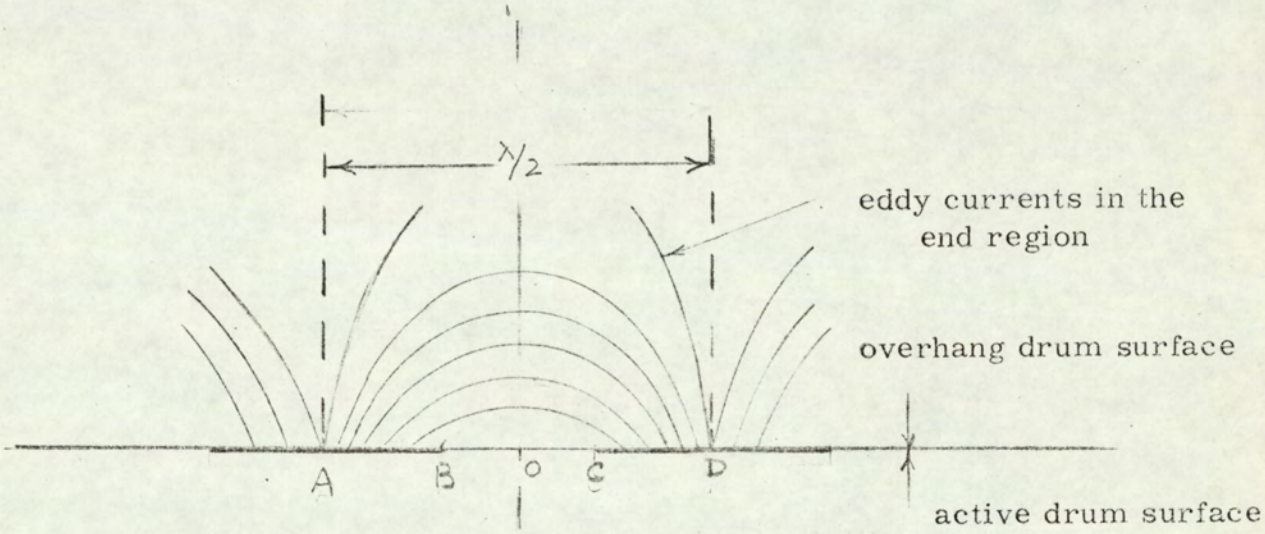

FIGURE 4.9

Since the excitation in the active region was by discrete poles, and the drum overhang was finite, the idealised representation of the problem in the z-plane is shown in Figure 4.10. The figure shows two electrodes AB and CD corresponding to two consecutive poles, applied to a conductor bounded in all directions, that is ADEFA in Figure 4.10, and DE represents the drum overhang. Using Schwarz-Christoffel transformations, Gibbs obtained the final electrode configuration

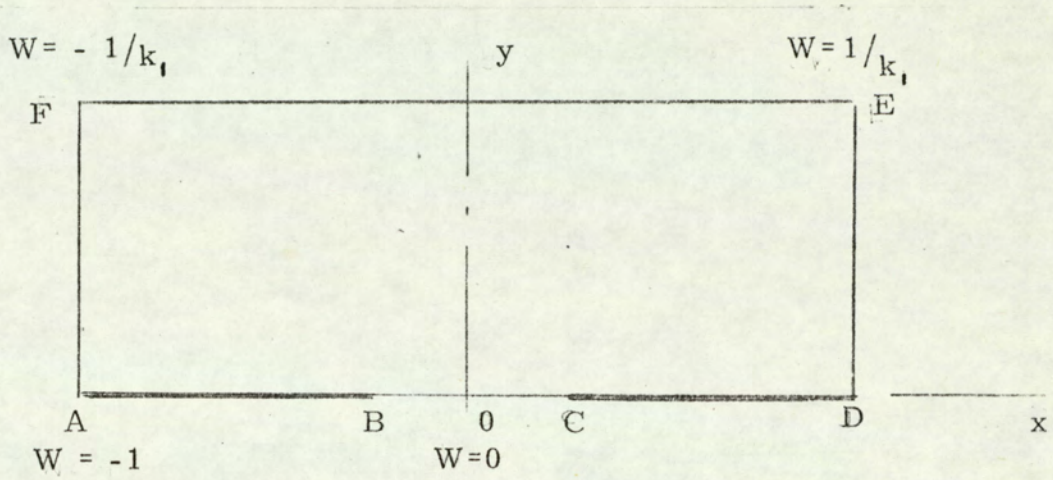

FIGURE 4.10

shown in Figure 4.11† from which he obtained the required effective resistance of the end region per unit depth of the drum as

$$R_e = \rho \frac{2K}{K'}, \qquad (4.1)$$

where K and K' are elliptic integrals*.

---

* These integrals and the detailed mathematical manipulations are given in full in Reference 30.

† overleaf

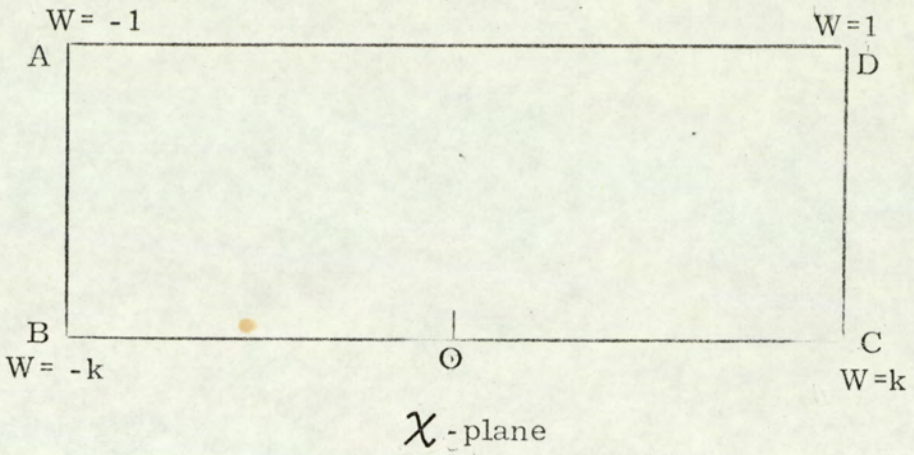

FIGURE 4.11

Figure 4.12 is drawn from data given in Table 14 of Reference 30. This figure shows the relation between R_e/ρ and the ratio $s = \frac{DE}{OD}$, where DE is the drum overhang, and OD is half the pole pitch (see Figure 4.9 & 4.10)

Gibbs shows that, when DE (the drum overhang) tends to an infinite length, $R_e/\rho \rightarrow 2.00$. It will be seen from Figure 4.12 that, for $DE/OD > 1.2$ the overhang may be considered to be infinite.

Consider the idealised current flow in the active and end-regions shown in Figure 4.13. The resistance

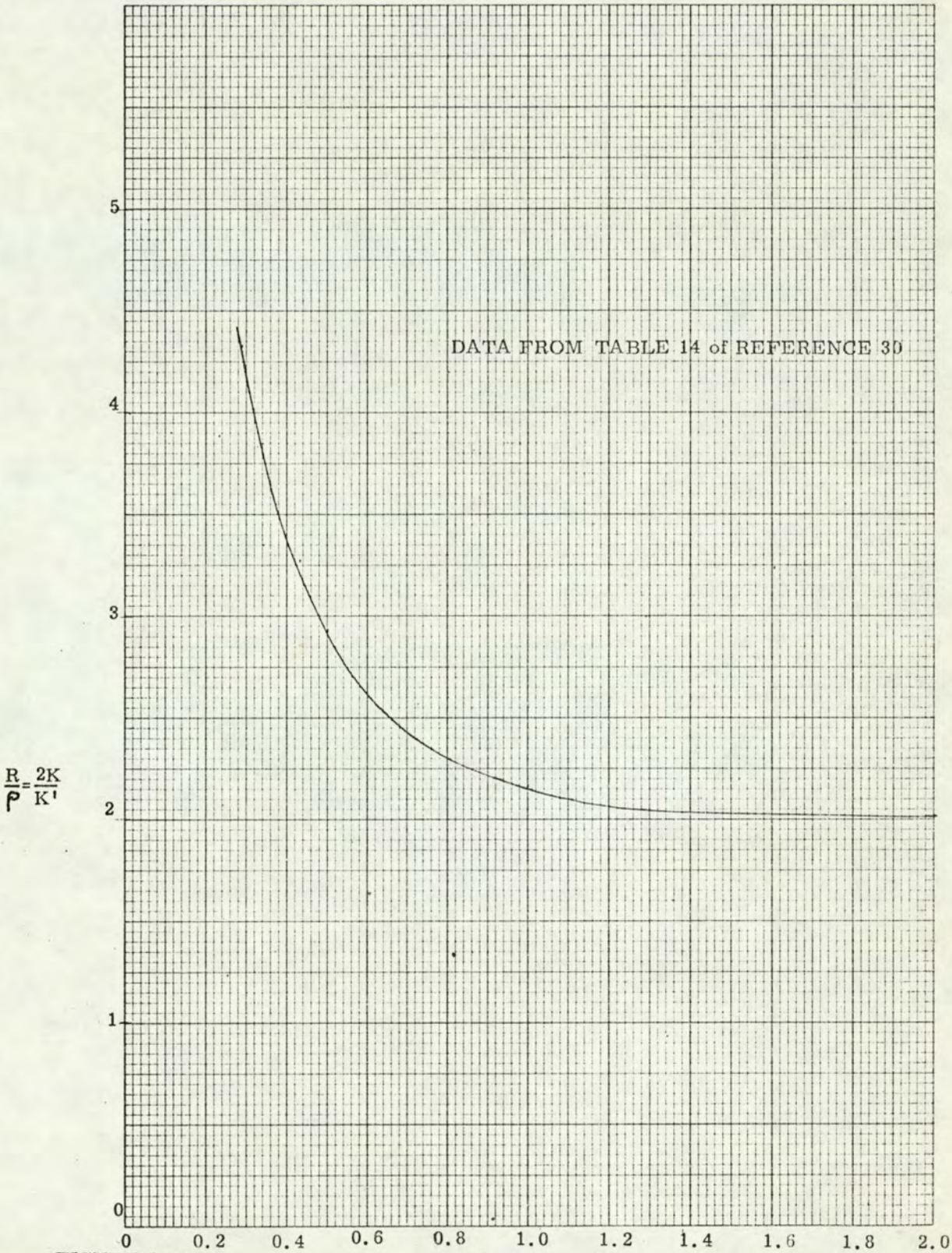
DATA FROM TABLE 14 of REFERENCE 30
$\frac{R}{P}=\frac{2K}{K'}$
0
1
2
3
4
5
0
0.2
0.4
0.6
0.8
1.0
1.2
1.4
1.6
1.8
2.0
$S=\frac{DE}{OD}$, see p. 98.

FIGURE 4.12

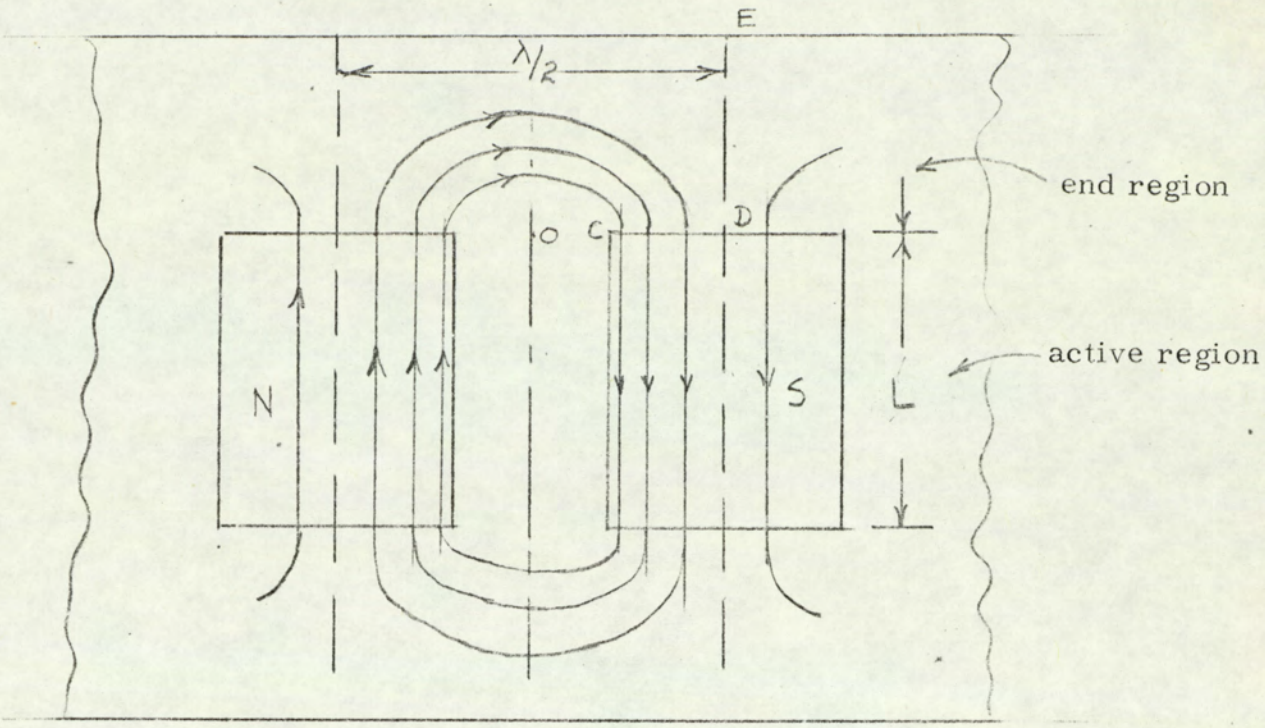

FIGURE 4.13

of the current path in the active region for unit depth of drum is taken to be

$$R_a = \frac{4\rho L}{\lambda(1 - 4\gamma)} \qquad (4.2)$$

where $\gamma = OC/\lambda$ (see Figure 4.9)

Therefore

$$R_{e/R_a} = \frac{\lambda(1 - 4\gamma)}{2L} \cdot \frac{K}{K'} \qquad (4.3)$$

For the experimental coupling

$$s = {}^{DE}/_{OD} = \frac{2.54 \times 10^{-2}}{2.08 \times 10^{-2}} = 1.22$$

$$\gamma = 0.08,$$

$$\lambda = 8.3 \times 10^{-2} \text{ m},$$

$$L = 2.54 \times 10^{-2} \text{ m},$$

and $${}^{2K}/_{K'} = 2.05$$ (from Figure 4.12).

Substitution of these values in equation (4.3) gives:

$$R_e/R_a = 1.14 \qquad (4.5)$$

4.4.2 Experimental ratio of end-region loss to active region loss

Assume initially that the copper endring losses are negligible compared with the corresponding loss in the solid drum (see Section 4.4.3). Then, from Figures 4.14 and 4.15, which show the variation of the fundamental torque with fundamental flux at constant speed for the two drums, we can obtain the torque for the two couplings at given values of ϕ_{ac} and slip-speed.

Let T_e = the torque of the endring drum at slip-speed n and fundamental flux, ϕ_{ac},

T_s = the torque of the solid drum at the same slip-speed and fundamental flux.

Then $2\pi\, nT_e$ and $2\pi\, nT_s$ are the total losses in the endring and solid drums. Therefore

$$2\pi\, nT_e - 2\pi\, nT_s = \text{loss in the endregion of the solid drum.}$$

The reduction in torque in the solid drum can be due only to the additional end-region losses.

Therefore

$$\frac{\text{end region loss}}{\text{active-region loss}} = \frac{2\pi\, nT_e - 2\pi\, nT_s}{2\pi\, nT_s} = \frac{T_e - T_s}{T_s} \qquad (4.6)$$

The loss ratios obtained from Figures 4.14 and 4.15 are given in Table 4.4. The average loss ratio is 1.48 with maximum deviations from this value of +12.9% and -9.5%.

From Gibbs' analysis, we have

$$\frac{\text{end region loss}}{\text{active region loss}} = \frac{I^2 R_e}{I^2 R_a} = 1.14 \text{ (see equation (4.5))}$$

where I is the effective current.

VARIATION OF FUNDAMENTAL TORQUE WITH FUNDAMENTAL FLUX AT CONSTANT SPEED - ENDRING DRUM

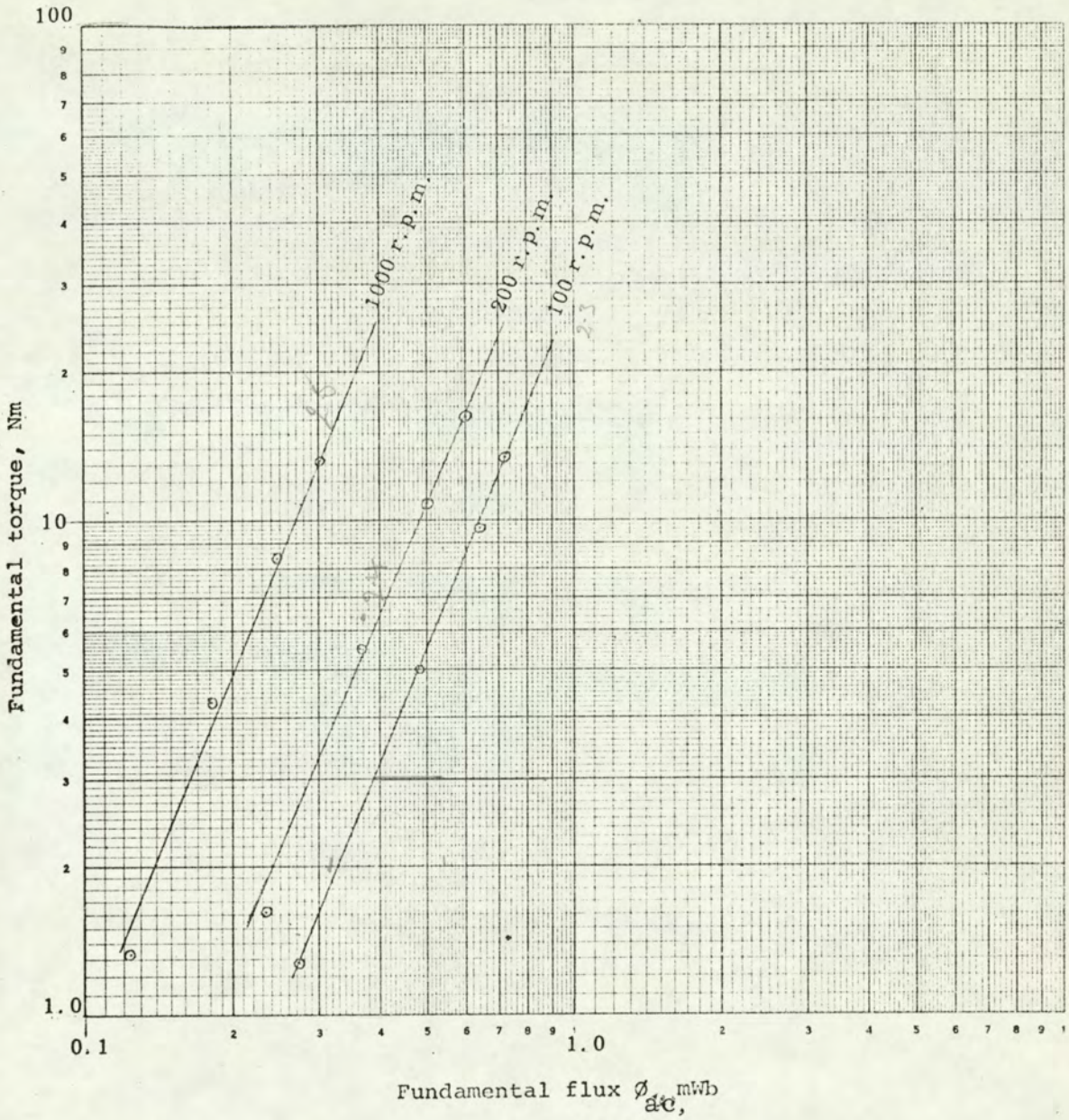

FIGURE 4.14

VARIATION OF FUNDEMENTAL TORQUE WITH FUNDAMENTAL FLUX AT CONSTANT SPEED - SOLID DRUM - TEST RESULTS FROM REFERENCE 6.

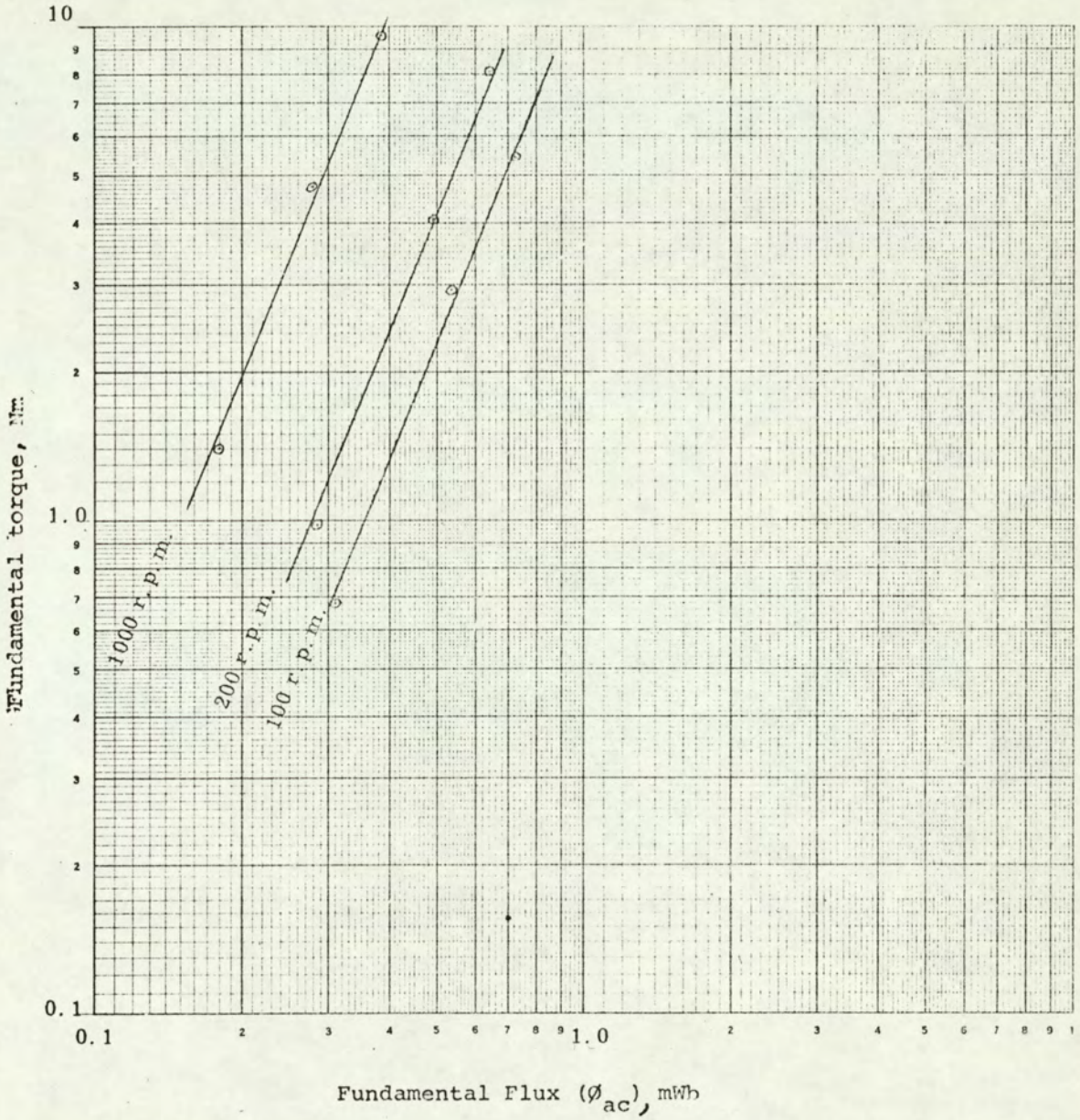

FIGURE 4.15

Table 4.4 End region loss to active region loss ratio

Slip-speed, r.p.m.	ϕ_{ac}, mWb	T_e, Nm	T_s, Nm	$(T_e - T_s)/T_s$	Exp.* / Gibbs
100	0.3	1.6	0.66	1.42	1.246
	0.4	3.2	1.3	1.46	1.282
	0.5	5.5	2.25	1.44	1.264
	0.6	8.2	3.5	1.34	1.175
200	0.4	6.4	2.4	1.67	1. 465
	0.5	10.9	4.1	1.65	1.45
	0.6	16.2	6.4	1.53	1.344
1000	0.2	4.9	1.9	1.58	1.388
	0.3	13	5.25	1.47	1.29
	0.4	25.5	11.0	1.26	1.106

* $\frac{\text{Experimental}}{\text{Gibbs}} = \frac{(T_e - T_s) R_a}{T_s R_e}$

The ratio of the experimental loss ratio to Gibbs' ratio is given in the last column of Table 4.4. It will be seen that the experimental ratio exceeds Gibbs' ratio of 1.14 by between 10% and 46% which is surprisingly good correlation when one considers the initial assumptions in Gibbs' analysis. A further contributory factor to the deviations from Gibbs' ratio may possibly be the tacit assumption that the two drum overhangs were identical, when in fact the experimental drum was open-ended at one end and fixed to a mild steel ring at the other (see Figure A2-2 and Plate 2).

It would appear that equation (4.1) in conjunction with Figure 4.12 would be of considerable value in practical design work.

4.4.3 Copper endrings loss to active region loss ratio

The following analysis shows that the end-region loss is negligible with copper endrings. Assume that

a) the currents in the active region are axial;
b) the currents in the active region are confined to the depth of penetration;
c) the end region currents are confined to the copper rings.

The idealised problem is shown in Figure 4.16. The current distribution in half a pole-pitch ($\lambda/4$) is considered.

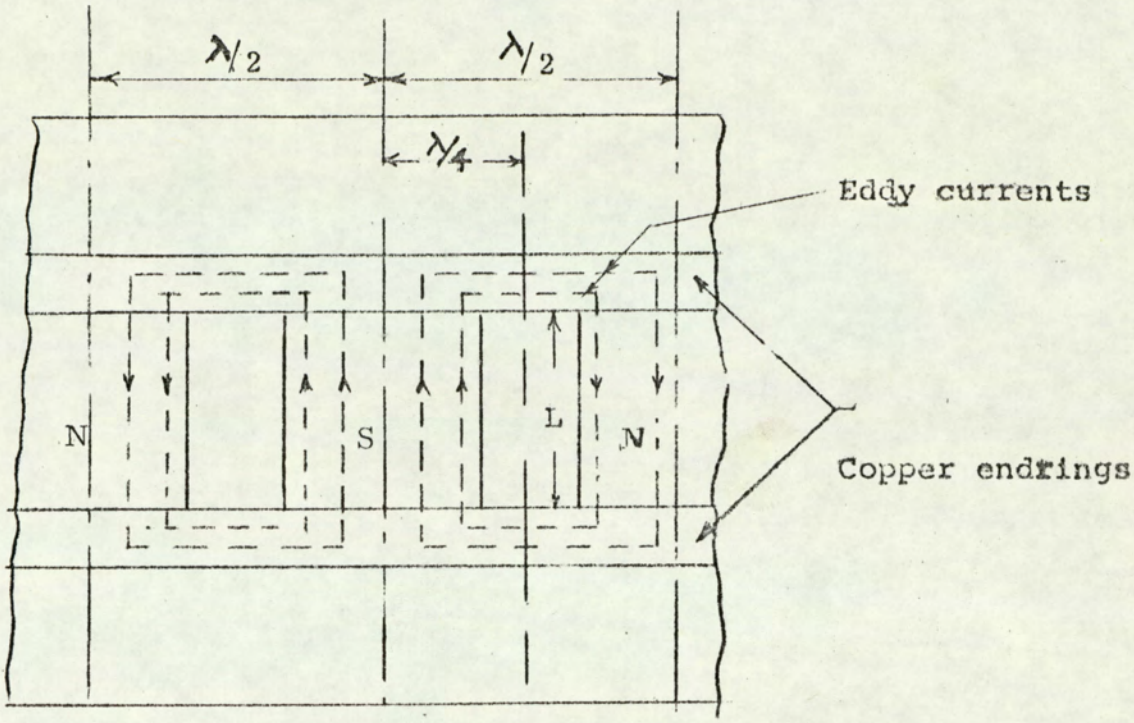

FIGURE 4.16

Iron drum active region loss = $I^2 R_i$ (4.7)

where I is the equivalent current (equation 1·8),

$$R_i = \rho_i \frac{L}{A_i},$$

ρ_i is the resistivity of iron,

L is the active length,

and $A_i = d\lambda/4$ area of cross-section of the current path in iron.

Therefore

Iron drum active region loss = $4\rho_i L I^2/d\lambda$ (4.8)

The loss in the copper endrings

$$= \rho_c \frac{L_c}{A_c} \cdot (I/_2)^2 , \qquad (4.9)$$

where ρ_c is the resistivity of of copper,

$L_c = \lambda/_2$,

A_i is the area of cross-section of the copper endring

and $(I/_2)$ is the average current in the copper endring.

Hence

$$\frac{\text{loss in copper endrings}}{\text{loss in drum active iron}} = \rho_c \frac{L_c}{A_c} \cdot \frac{1}{16} \cdot \frac{\lambda . d}{\rho_i L} \qquad (4.10)$$

Substitution of

$\rho_i = 11.2 \times 10^{-8}$ Ωm at 20° C

$\rho_c = 1.72 \times 10^{-8}$ Ωm at 20° C

$L_c = 4.15 \times 10^{-2}$ m

$L = 2.54 \times 10^{-2}$ m

$A_i = 2.07 \times 0.3 \times 10^{-4}$ m^2 (for d = 3 mm)

$A_c = 1.27 \times 1.27 \times 10^{-4}$ m^2

in equation (4.10) shows that

$$\frac{\text{loss in copper endrings}}{\text{loss in drum active iron}} = 0.022 \text{ (at } 20^\circ \text{ C)}.$$

The temperature coefficient of resistance of copper is

only 0.7 that of wrought iron at 20° C. Taking this into account at a maximum drum working temperature of 200° C, the loss ratio reduces to 0.008. Therefore, the assumption of negligible copper endring losses is valid.

4.5 An alternative analysis of the end region

The following treatment of the end region, which is simpler than Gibbs'[3], has been found to give good correlation with experimental results.

Figure 4.17 shows the alternative model of the end region. It represents the end region as a thin conductive sheet of finite width, along one edge of which there is a sinusoidal potential distribution. For analytical simplicity, it will be assumed as did Gibbs[3], that the current flow is resistance-limited.

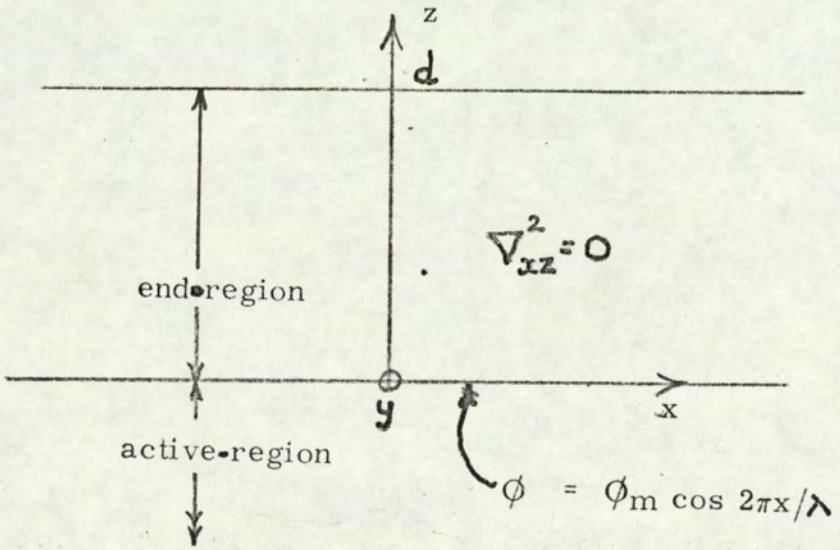

Figure 4.17

Since the conductive sheet is thin, we may assume a quasi-two-dimensional distribution

$$\nabla^2 \phi_{xz} = 0 \qquad (4.11)$$

The suitable general form for ϕ is

$$\phi = C \cosh pz \cos px, \qquad (4.12)$$

where C and p are constants to be determined from the boundary conditions. The required solution of (4.11) is

$$\phi = \left(\phi_m / \cosh 2\pi d/\lambda\right) \cosh \frac{2\pi}{\lambda}(z - d) \cos \frac{2\pi x}{\lambda} \qquad (4.13)$$

The loss per pole pitch is

$$W_p = \int_0^d \int_0^{\lambda/2} \rho \, |J|^2 \, dx \, dz$$

$$= \int_0^d \cdot \int_0^{\lambda/2} (J_x^2 + J_z^2) \, dx \, dz, \qquad (4.14)$$

where $J_x = -\frac{1}{\rho} \frac{\partial \phi}{\partial x}$,

and $$J_z = -\frac{1}{\rho}\frac{\partial \phi}{\partial z} .$$

After substituting for J_x and J_z from (4.13), integrating and simplifying we obtain

$$W_p = (\pi \phi_m / 2\rho) \tanh 2\pi d/\lambda \qquad (4.15)$$

The 'total' current in the strip is

$$I_T = \left(\int_o^d J_x \, dz \right)_{x = \lambda/4,}$$

$$= (\phi_m / \rho) \tanh 2\pi d/\lambda . \qquad (4.16)$$

The strip equivalent resistance per pole-pitch is

$$R_e = W_p / I_T^2$$

$$= (\pi \rho/2) \coth 2\pi d/\lambda \qquad (4.17)$$

The corresponding resistance of the active-region is (in conformity with Gibbs[3])

$$R_a = 4\rho L/\lambda , \qquad (4.18)$$

and the end region to active region loss ratio is

$$I_T^2 R_e / I_T^2 R_a = (\pi \lambda/8L) \coth 2\pi d/\lambda \qquad (4.19)$$

Substituting $\lambda = 8.3 \times 10^{-2}$ m,

$L = 2.54 \times 10^{-2}$ m,

and $d = 2.54 \times 10^{-2}$ m,

in (4.19) we obtain for the experimental solid-drum coupling

$$\frac{\text{end region loss}}{\text{active region loss}} = 1.336$$

The experimental loss ratios are compared with this alternative factor and that of Gibbs in Table 4.5

It will be seen from this table that the deviation of the alternative method varies from -5% to 25%.

TABLE 4.5

Slip-speed r.p.m.	ϕ_{ac} m.Wb	Experimental / Alternative	Experimental / Gibbs
100	0.3	1.07	1.246
	0.4	1.09	1.282
	0.5	1.08	1.264
	0.6	1.01	1.175
200	0.4	1.25	1.465
	0.5	1.25	1.45
	0.6	1.15	1.344
1000	0.2	1.18	1.388
	0.3	1.10	1.29
	0.4	0.95	1.106

In the practical coupling, the end region is indeterminate (Section 4.1). The graph coth $2\pi d/\lambda$ against d/λ shown in Figure 4.18 clearly indicates that for values of $d/\lambda > 0.2$ the end region may be assumed to extend to infinity which corresponds to a similar condition in Gibbs' analysis.

4.6 Conclusions and suggestions for further work

The generalised curves derived by Davies[12] have been shown to be within the limits of accuracy required for design studies of couplings over the range of $0.2 \leq n/n_m \leq 4$. This demonstrates that, even when faced with the analytical intractability of solid iron, a judicious blend of theory and practice, as used by Gibbs and Davies, can yield results of practical usefulness.

Below $n/n_m = 0.2$, that is in the low-frequency operating range, the performance of the coupling requires further investigation since the assumption $\sqrt{2}\alpha \gg 2\pi/\lambda$ * is not valid in this frequency range.

That the end-effects in a solid iron drum have a pronounced effect on the torque-speed characteristic has been demonstrated. It has been shown that there is little difference in the magnitude of the peak torque developed by the same coupling fitted with either a solid-iron drum or an endring drum. However, the

---

* See Section 1.4

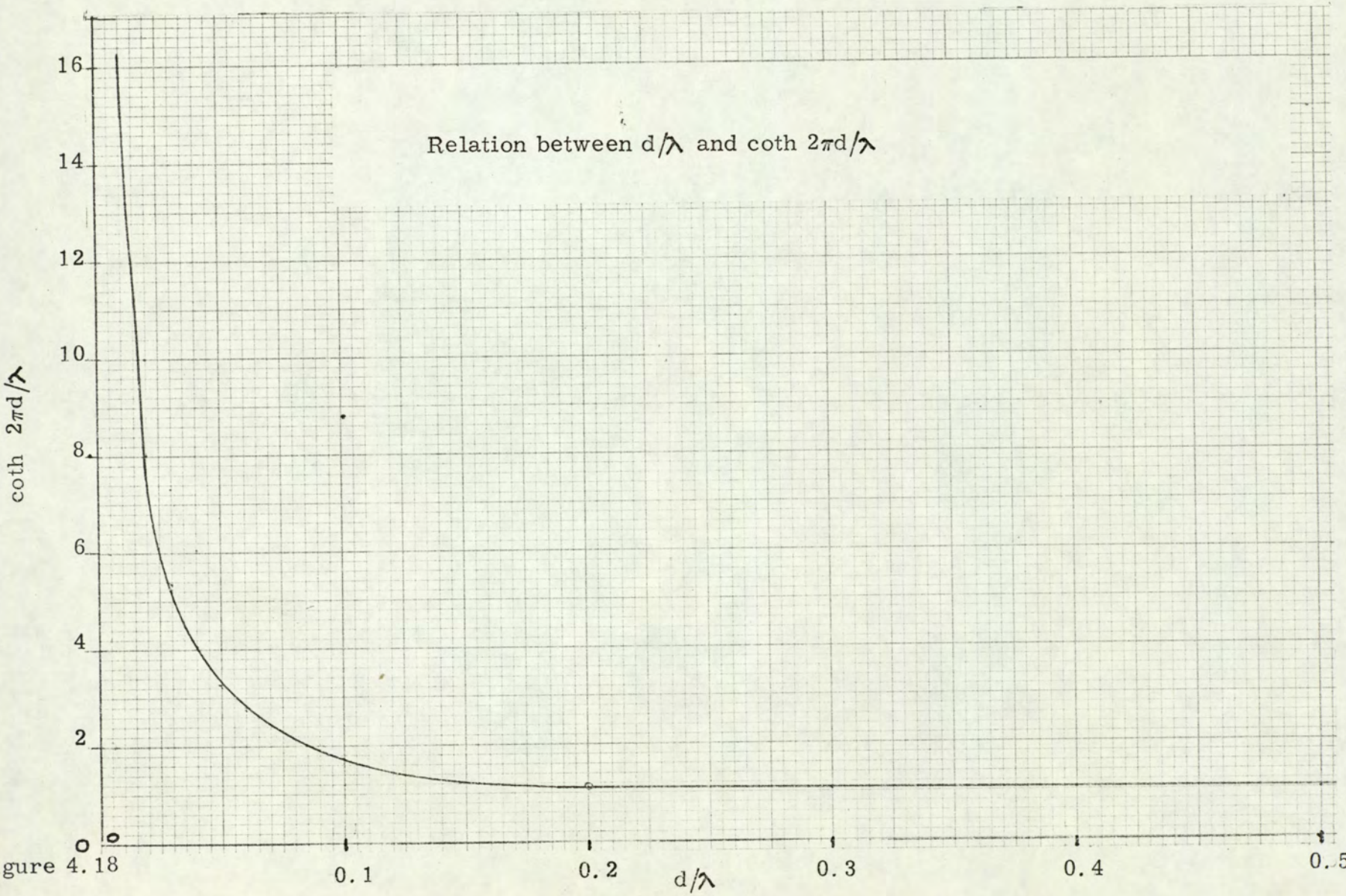
Relation between d/λ and coth 2πd/λ
coth 2πd/λ
16
14
12
10
8
6
4
2
0
0
0.1
0.2
0.3
0.4
0.5
d/λ

Figure 4.18

speed at which the peak torque is developed with the solid-iron drum is appreciably greater than with the endring drum (of the order of 100% greater). Since the only constructional difference between the two coupling configurations was in the end regions, one may reasonably attribute the difference in the torque-speed characteristics to end-effects.

The pronounced effect on the torque-speed characteristic of the end regions makes it essential to be able to assess their effects as accurately as possible. Both equations for the resistance ratios (equation (4.3) and equation 4.19) are simple to apply and either would be adequate for preliminary design studies. At this stage, it would seem that accurate prediction of the coupling performance must await more detailed investigations of the end region.

References (I) Eddy-current couplings and brakes

1. Rudenberg, R.: The energy of eddy currents (in German) Sammlung Elektrotechnischer Vortrage (a year book), 1906, F. Enke, Stuttgart, Germany.

2. Rosenberg, E.: Eddy-currents in solid iron Elektrotechnik und Maschinenbau, 1923, Vol. 41, No. 49, pp 1055 and 1074

3. Gibbs, W. J.: The theory and design of eddy-current slip couplings BEAMA Journal, 1946, pp 123, 172, 219

4. Sharov, V.: Armature reaction of massive iron in electromagnetic slip couplings Elektrichestvo, 1956, no. 10, pp42

5. Glazenko, T. A.: Some design problems for an asynchronous clutch with a solid mass rotor Arotomatika i Telemekhanika, 1958, no. 8, Vol. XIX, pp 800

6. Davies, E. J.: Two experimental studies in dynamo electric machinery Ph.D. Thesis, University of Bristol, 1961

7. Erdelyi, E. A. and Kolatorowicz, E. E.: Model laws of eddy-current couplings for aircraft alternator drives I.E.E.E. Trans, Power Apparatus and Systems, Vol, 79, 1961, pp 438

8. Davies, E. J.: An experimental and theoretical study of eddy-current couplings and brakes
I.E.E.E. Trans., Power Apparatus and Systems, 1963, vol. 82, pp 401

9. Malti, M. G., and Ramakumar, R.: Three dimensional theory of eddy-current coupling
I.E.E.E. Trans., Power Apparatus and Systems, 1963, vol. 82, pp 793

10. Hansen, A., and Timmler, W. R.: Theory of eddy-current couplings - unidirectional flux type
I.E.E.E. Trans., Power Apparatus and Systems, 1963, vol. 82, pp 436

11. Gonnen, D., and Stricker, S.: Analysis of an eddy-current brake
I.E.E.E. Trans., Power Apparatus and Systems, 1965, pp 357

12. Davies, E. J.: General theory of eddy current couplings and brakes
Proc. I.E.E., 1966, vol. 133, pp 825

13. Bahler, W., and van der Hock, W.: An eddy-current coupling used as a variable speed drive
Phillips Technical Review, 1966, vol. 27, pp 15

II Solid iron rotor induction and synchronous machines

14. Gibbs, W. J.: Induction and synchronous motor with unlaminated rotor
Proc. I.E.E., 1948, vol. 95, Pt. II, pp 411

15. McConnell, H. M., and Sverdrup, E. F.: Induction machine with solid iron rotor
I.E.E.E. Trans., Power Apparatus and Systems, 1955, vol. 74, pp 343

16. Angst, G.: Polyphase induction motor with solid rotor: effects of saturation and finite length
I.E.E.E. Trans., 1961, vol. 80, pp 902

17. Bratoljic, T.: Recent studies of stray losses in solid pole-piece of synchronous machines
Brown Boveri Review, 1966, vol. 53, pp 521

18. Adderley, K. J.: Load losses in synchronous machines
M.Sc. Thesis, The University of Aston in Birmingham, 1968

III Eddy-current theories

19. Rosenberg, E.: Eddy currents in iron masses
Electrician, August 1923, pp 182

20. Pohl, R.: Electromagnetic and mechanical effects in solid iron due to alternating or rotating magnetic fields
Proc. I.E.E., 1944, vol. 91, pp 239

21. Aspden, H.: Eddy currents in solid cylindrical cores having non-uniform permeability
Journal Applied Physics, 1952, vol. 23, pp 523

22. McLean, W.: Theory of strong magnetic waves in massive iron
Journal of Applied Physics, 1954, vol. 25, pp 1267

23. Agarwal, P. D.: Eddy current losses in solid and laminated iron
I.E.E.E. Trans, Communication and Electronics, 1959, vol. 78, pp 169

24. Stoll, R. L., and Hammond, P.: Calculation of the magnetic field of rotating machines - Part 4. Approximate determination of the field and the losses associated with eddy currents in conducting surfaces
Proc. I.E.E., 1965, vol. 112, pp 2083

25. Lawrenson, P. J.: Tooth ripple losses in solid poles
Proc. I.E.E., 1966, vol. 113, pp 657

V Books

26. Moon, P., and Spencer, D. B.: Field theory for engineers
D. Van Nostrand Co., Inc.

27. Fitzgerald, A. E., and Kingsley, C.: Electric machinery
McGraw-Hill Book Company

28. Lammeraeni, J., and Stafl, M.: Eddy currents
Iliffe Books Ltd.

29. Vitkovich, D.: Field analysis
D. Van Nostrand Co., Inc.

30. Gibbs, W. J.: Conformal Transformations in Electrical Engineering - Chapman and Hall.

Acknowledgements

The writer wishes to acknowledge with gratitude the continuous advice and encouragement given by Professor E. J. Davies, Professor in Electrical Engineering, in the University of Aston in Birmingham, who has supervised the work from which this thesis is drawn and his permission to reproduce a number of diagrams.

The writer wishes to thank the following:

Messrs. K. J. Adderley, A. L. Bowden, N. Kerruish and Dr. H. McKibbin for many useful discussions and advice;

Messrs. A. Stevenson and M. Ellett for their unstinted assistance with the equipment;

Miss C. Glass and Mrs. B. Gore for preparing the typescript of this thesis;

Messrs. J. T. Whittle and H. Smith for reproducing the typescript and for various photocopying work.

Appendices

Appendix A.1 Generalised Equations

The generalised equations for the coupling derived by Davies[6, 8, 12] are given below.

A1-1 Fundamental flux per pole

$$\phi_{ac} = k_2 \, M \, \frac{T^{(2m-1)/2m}}{n^{1/4m}} \qquad \text{(A1-1)}$$

where $K = (\mu\mu_o)^{1/4} \, H/H^m$,

$$k_2 = 1.8\pi^{1/4m}(K/2)^{1/m},$$

$$M = \frac{\rho^{1/4m} \, L^{1/2m}}{p^{\frac{4m-1}{4m}} \, D^{\frac{2m-1}{2m}}}$$

and for m = 0.77

$$\phi_{ac} = 3\left(\frac{T^{0.35}}{n^{0.325}}\right) \qquad \text{(A1-2)}$$

A1-2 Peak armature reaction

$$F_R = \frac{1}{k_3 \, p^2 \, K_2 \, M} \cdot T^{1/2m} \, n^{1/4m}$$

(A1-3)

and for m = 0.77

$$F_R = \frac{0.855 \times 10^4}{2.86\ p^2}\ T^{0.65}\ n^{0.325} \qquad \text{(A1-4)}$$

A1-3 Peak torque (T_m) and speed at peak torque (n_m)

$$T_m = \frac{F_g^2}{C_1 C_2 (2 + C_3)} \qquad \text{(A1-5)}$$

where F_g = the total airgap m.m.f., At,

$C_1 = k_2 M S$

S = reluctance, At/Wb,

$C_2 = \frac{k_4 f}{p^2 M}$

$k_4 = \frac{1}{k_3 k_2}$

$C_3 = -2 \cos \delta$

and δ is the angle between armature reaction and main flux

$$n_m = \left(\frac{C_1}{C_2}\right)^{2m} T_m^{(2m-2)} \qquad \text{(A1-6)}$$

and for m = 0.77

$$n_m = k_6 \frac{\rho_g^2\ p^{2.08}}{F_g^{0.925}\ D^{3.08}}$$

where k_6 is a constant.

A1-4 Generalised torque-speed

$$\frac{T/T_m}{2 + C_3} = \frac{Q}{1 + C_3 Q + Q^2} \qquad \text{(A1-7)}$$

where $$Q = (T/T_m)^{1-m/m} \; (n/n_m)^{1/2m}$$

and for m = 0.77

$$\frac{T/T_m}{2 + C_3} = \frac{(T/T_m)^{0.3} \; (n/n_m)^{0.65}}{1 + C_3 (T/T_m)^{0.3} \; (n/n_m)^{0.65} + (T/T_m)^{0.6} \; (n/n_m)^{1.3}} \qquad \text{(A1-8)}$$

A1-5 Generalised fundamental flux per pole

$$(\phi/\phi_m)_{ac} = \left[\frac{(2 + C_3) \; Q}{1 + C_3 \; Q + Q^2}\right]^{0.35} \Big/ \; (n/n_m)^{0.325} \qquad \text{(A1-9)}$$

where $(\phi_m)_{ac}$ is the fundamental flux at peak-torque

A1-6 Generalised armature reaction

$$F_R/F_{R_m} = \left[\frac{(2 + C_3) \; Q}{1 + C_3 \; Q + Q^2}\right]^{0.65} \left[n/n_m\right]^{0.325} \qquad \text{(A1-10)}$$

where F_{R_m} is the armature reaction at peak-torque.

A1-7 Generalised drum loss

$$W/W_m = \frac{(2 + C_3)\ Q(n/n_m)}{1 + C_3\ Q + Q^2} \qquad \text{(A1-11)}$$

where W_m is the drum loss at peak-torque.

A.2 Axial airgap flux density distributions

A.2.1 Test results

The search coils described in Section 2.6.1 were used to measure axial flux-density distributions on load. Typical distributions are shown in Figure A.2-1 from which it will be seen that the axial distribution is not constant as was assumed for analytical simplicity (see Section 3.5).

A.2.2 Reasons for variation in axial distributions

To simplify analysis of solid iron problems, it is usual to assume that the eddy currents in the active region are solely axial. An examination of the dynamic flux-density distribution across the pole-face (Figure A.2-1) reveals that this assumption is not valid, even when the iron drum is provided with copper endrings. The depression in the axial flux-density distribution curve would appear to imply that there are closed eddy-current paths within the active region. Figure A2-1 shows that the maximum depression is displaced towards the open end of the drum and moves closer to it with increasing frequency. The reason for this is probably the inductive imbalance between the two end regions (see Figure A2-2).

FLUX DENSITY DISTRIBUTION ALONG POLE FACE (AXIAL) UNDER LOAD FOR VARIOUS SPEEDS AT CONSTANT EXCITATION (See Figure 2.5(b)

FIELD CURRENT 0.3A

ENDRING DRUM

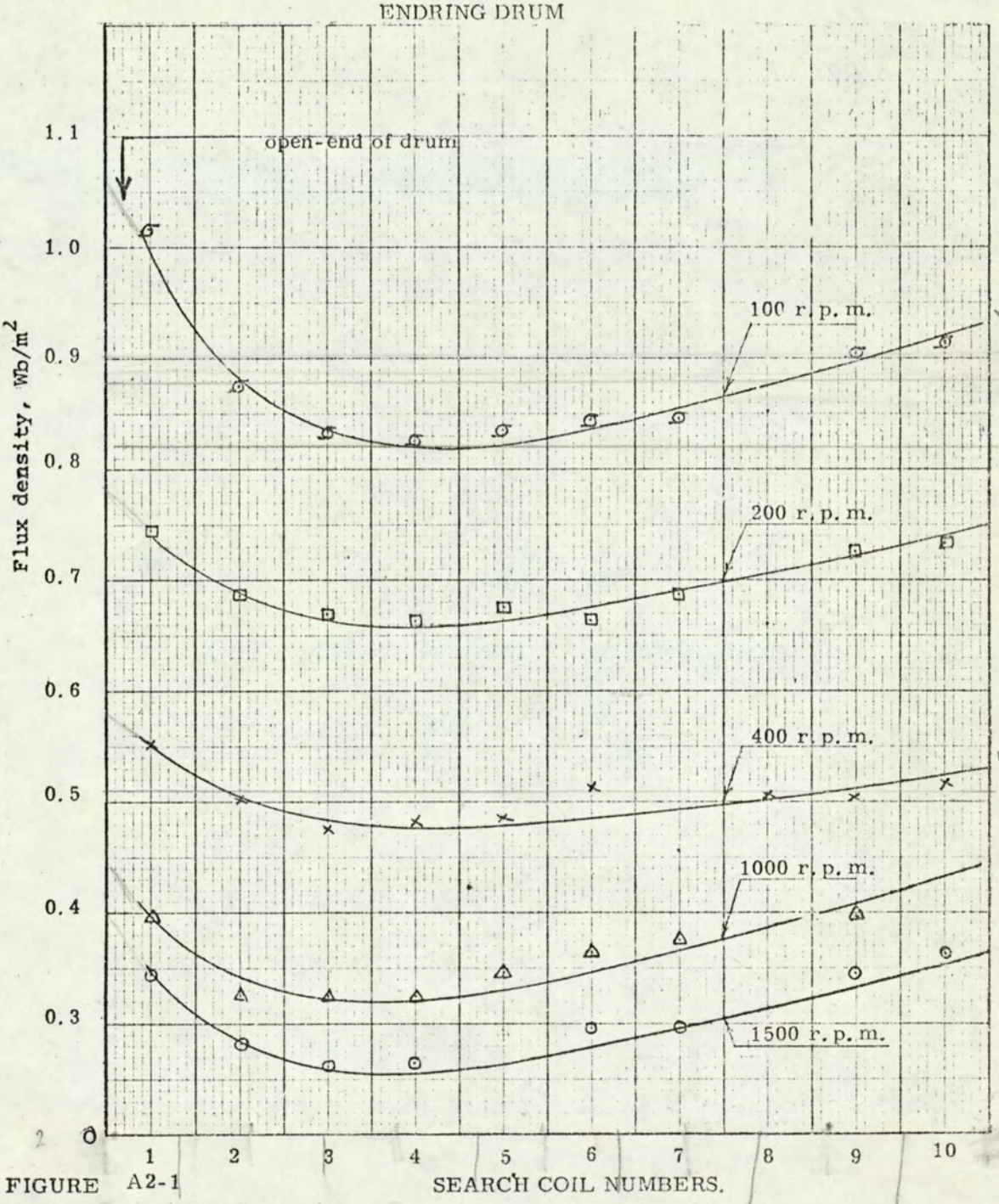

FIGURE A2-1

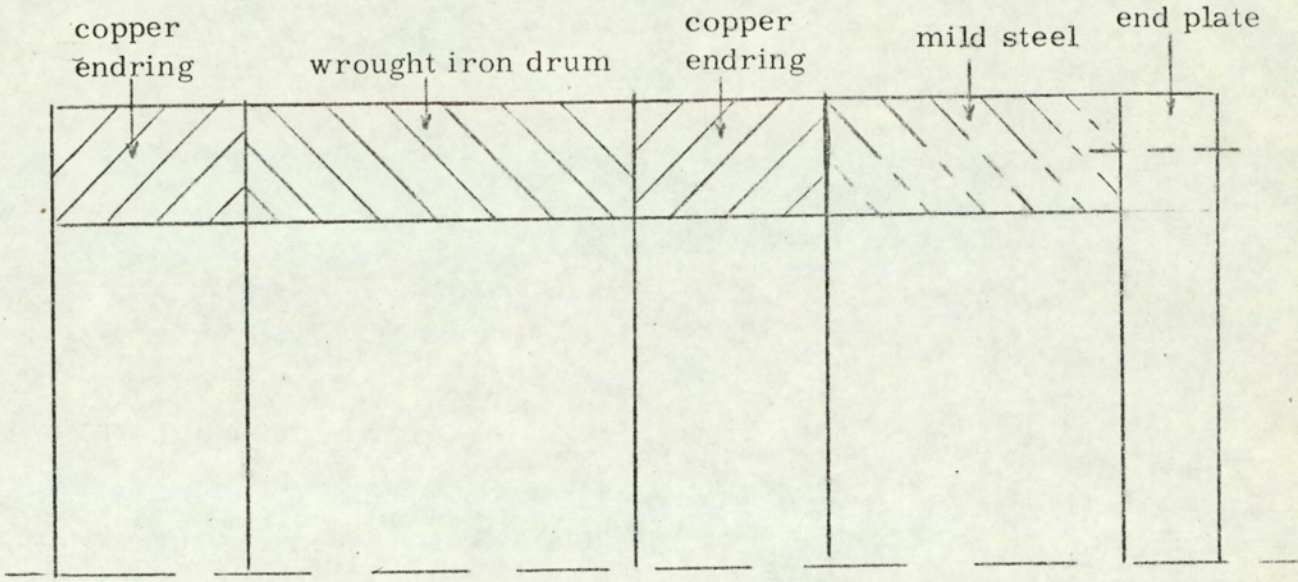

Half section of endring drum

Figure A2. 2

A.3 Field member leakage flux

The leakage flux paths in a partially interdigitated field member are shown in Figure A3-1. The pole edge component of the leakage flux will increase with the degree of interdigitation. Search coils shown in Figure 2.7(a) and (b), page 30, were used to measure the flux through all the poles (six) of the same polarity and the corresponding core fluxes; the total leakage flux being the difference between the core and pole fluxes.

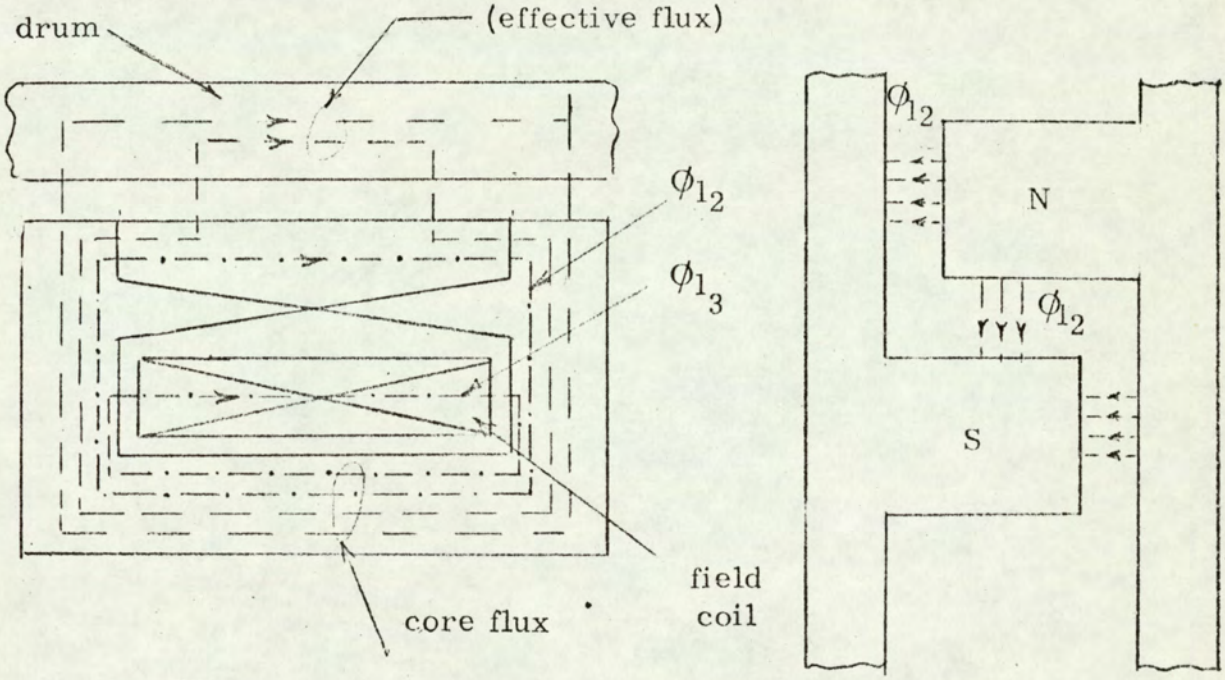

Figure A3-1

A.3-1 Test results

Test results of the total leakage flux are given in Table A3-1. It will be seen that at standstill the leakage flux is about

30% of the total core flux. The percentage leakage flux increases on load since the armature reaction reduces the effective flux, with a corresponding reduction in any saturation which may be present in the core. The effect of this reduced saturation in the core is equivalent to a reduction in the reluctances of the leakage paths of the fluxes ϕ_{ℓ_2} and ϕ_{ℓ_3} (see Figure A3-1).

TABLE A3-1

Field member leakage flux (end ring-drum)

Standstill

Field current A	Total flux* m Wb	Pole face flux* m Wb	Leakage flux* m Wb	Leakage flux, per cent of total flux
0.1	2.8	2.0	0.8	28.5
0.2	5.1	3.9	1.2	23.5
0.3	6.6	4.75	1.85	28
0.4	7.5	5.15	2.35	32
10 Hz (100 r.p.m.)				
0.1	2.3	1.7	0.6	26
0.2	4.15	2.8	1.35	32.5
0.3	5.7	3.55	2.15	38
0.4	6.8	4.15	2.65	39
20 Hz (200 r.p.m.)				
0.1	2.0	1.4	0.6	30
0.2	3.7	2.3	1.4	38
0.3	5.0	2.9	2.1	42
0.4	6.0	3.4	2.6	43.3
40 Hz (400 r.p.m.)				
0.1	1.65	1.1	0.55	33
0.2	3.2	1.8	1.4	44
0.3	4.45	2.25	2.24	49.5
0.4	5.3	2.6	2.7	51
100 Hz (1000 r.p.m.)				
0.1	1.4	0.8	0.6	43
0.2	2.6	1.3	1.3	50
0.3	3.65	1.6	2.05	56.5
0.4	4.5	1.75	2.75	61
150 Hz (1500 r.p.m.)				
0.1	1.2	0.65	0.55	46
0.2	2.3	1.0	1.3	56
0.3	3.3	1.2	2.1	64

* For half the poles (six)